國立交通大學

機械工程學系

博士論文

應用薄膜-集塊理論分析質子交換膜燃料電池之暫態行為

Analysis of the Transient Behavior for PEM Fuel Cell Using Thin Film-Agglomerate Model

研究生　：張時明

指導教授　：陳俊勳教授

曲新生教授

中華民國九十六年六月二十九日


E
S
A
1896

應用薄膜-集塊理論分析質子交換膜燃料電池之暫態行為

Analysis of the Transient Behavior for PEM Fuel Cell Using Thin Film-Agglomerate Model

研究生： 張時明　　Student: Shih-Ming Chang

指導教授：陳俊勳 曲新生　　Advisor: Chiun-Hsun Chen

Hsin-Sen Chu

國 立 交 通 大 學

機械工程學系

博 士 論 文

A dissertation

Submitted to Department of Mechanical Engineering

College of Engineering

National Chiao Tung University

in Partial Fulfillment of the Requirements

for the Degree of

DOCTOR OF PHILOSOPHY

in

Mechanical Engineering

June 2007

Hsinchu, Taiwan, Republic of China

中華民國九十六年六月


E
S
A
1896

國立交通大學

論文口試委員會審定書

本校 機械工程 學系博士班 張時明 君

所提論文(中文) 應用薄膜-集塊理論分析質子交換膜燃料電池之暫態行爲

(英文) Analysis of the Transient Behavior for PEM fuel cell using Thin film-Agglomerate Model

合於博士資格水準、業經本委員會評審認可。

口試委員：陳朝光　洪哲文

顧維謀　楊文美

曲新生　陳俊勳

指導教授：陳俊勳　曲新生

系主任：　教授

中華民國 九十五 年 六 月 二十九 日


E
S
A
1896

應用薄膜–集塊理論分析質子交換膜燃料電池之暫態行為

研究生：張時明　　指導教授：陳俊勳 曲新生

摘 要

近年來，燃料電池已經廣泛地應用在可攜式電子產品，如行動電話、筆記型電腦、及數位相機等等。目前研究燃料電池的主要方向大都在於如何降低成本、提高穩定性及續電力。質子交換膜燃料電池具有啓動快速、工作溫度低以及單位功率所需成本低的優點，這是它比其他類型的燃料電池有利的地方。而可攜式電子產品對高動態負載的要求比較高，但是目前的研究大多以穩態爲主而非暫態。爲了設計出更高性能的質子交換膜燃料電池，所以發展暫態模式的研究乃勢所必然。

首先，本文是以兩相流、半電池的模式進行質子交換膜燃料電池的暫態分析。在觸媒層的電化學反應則以圓柱形薄膜-集塊模式(thin film-agglomerate model)模擬，用以探討質子交換膜燃料電池中氣態水及液態水、氧氣及質子的分佈及變化情形。其中質子的傳輸速度較其他快很多，到達穩態所需時間約在 0.1 秒左右，而液態水則需要數十秒的時間。質子電位的變化在初期先急劇下降，而在達到極值後，隨時間增加而漸漸上升達到定值。本文也同時探討不同的操作條件下對燃料電池性能的影響，如操作溫度及陰極入口氣體的相對濕度。在 60℃~80℃操作溫度下，操作溫度與電池性能呈正比。

此外，對於各項設計參數對電池性能的影響，如孔隙率、觸媒層厚度及集塊半徑(agglomerate radius)本文也有進一步的研究。電流密度隨時間的變化情形如下：在 0.01 秒內，電流密度的變化非常劇烈。在 0.01 秒到 0.1 秒間，則保持定值。在 1 秒後，它的變化情形則與操作電壓、孔隙率、觸媒層厚度及集塊半徑有關。當氣體擴散層的孔隙率介於 0.2 和 0.5 間時，電流密度與孔隙率呈正比。在 1 秒後，當孔隙率大於 0.3 以後，電流密度不會受到液態水的影響而下降。而

在觸媒層孔隙率方面，當孔隙率在 0.06 到 0.1 間時電流密度有最大值。觸媒層厚度則以 10 μm 到 13 μm 間，電流密度最大。而集塊半徑則建議應小於 100nm，才能獲得較高的電流密度。

最後本文在觸媒層的電化學反應以更接近實際的球形薄膜-集塊理論進行模擬，探討質子交換膜燃料電池中氣態水及液態水、氧氣及質子的分佈及變化情形。同時透過介面邊界條件結合液態水分量與 Nafion 相中的液態水，使得的液態水效應能夠更完整地納入研究。根據數值結果顯示，電池的最大質子過電位降隨操作電壓減少而增加，當電池克服其最大活化過電位後，電池只需較小的質子過電位降即可保持原有的電化學反應。當液態水分量及薄膜中的水含量同時偏高時，電池即容易發生水氾濫(flooding)。對於各項參數對電池性能的影響，如氣體擴散層與觸媒層中滲透係數(permeability)，觸媒含量以及氣體擴散層的厚度也一併探討。

Analysis of the Transient Behavior for PEM fuel cell using Thin Film-Agglomerate Model

Student: Shih-Ming Chang Advisor: Chiun-Hsun Chen
Hsin-Sen Chu

Abstract

Nowadays fuel cells have been enthusiastically developed in order to be used in portable devices, such as mobile phones, notebook computers, power tools and digital cameras etc. Cost, durability and stability are the main concerns of the R&D programs for the fuel cell systems. The advantages of PEM fuel cell include lower cost per kW, and fast start-up, and lower operating temperature. In actual applications, the cell behaviors are highly dynamic. However, most of the recent researches focus on steady state models instead of transient ones. In order to mimic the real performance characteristics of PEM fuel cell, it is crucial to develop the transient model.

The first part of this dissertation analyzes the transient behavior for a PEM fuel cell via two-phase and half cell model with a thin film-agglomerate approach to model the catalyst layer. The model includes the transports of gaseous species, liquid water, proton, and electrochemical kinetics. The numerical results reveal that the transport of proton is much faster than the others. The ionic potential reaches the steady state in the order of 10^{-1}sec but that of the liquid water transport takes place is in the order of 10 sec. The ionic potential does not decrease monotonically with time. In the very beginning, the ionic potential rise rapidly, and then reaches the critical value, and then increase till its steady state. We investigate how operating parameters affects the cell performance of a PEM fuel cell, such as the operating temperature and the inlet relative humidity of the cathode streams. For the operating temperature, the higher the operating temperature is, the higher the cell performance will be.

Subsequently, we investigate the parameters which can affect the cell performance such as GDL porosity, CL porosity, catalyst layer thickness and agglomerate radius in detail. The transient behaviors show that within 10^{-2}sec, the current density rises rapidly, and there is a plateau between 10^{-2}sec and 10^{-1}sec. After 1sec, the variations of current density depend on cell voltage, gas diffusion layer porosity, catalyst layer porosity, catalyst layer thickness and agglomerate radius. For gas diffusion layer porosity, between ε_{GDL}=0.2 and ε_{GDL}=0.5, the higher the GDL porosity is, the higher the cell current density will be. After 1sec, if the GDL porosity is below 0.3, the current

density will go down. For catalyst layer porosity, optimum current density appears between ε_{CL}=0.06 and ε_{CL}=0.1. For the catalyst layer thickness, the optimum values of catalyst layer thickness appears between δ_{CL}=10μm and 13μm. For the agglomerate radius, it suggests that the agglomerate radius should smaller than 100nm for a higher utilization of catalyst.

Finally, we investigate the transient behavior of a PEM fuel cell by using a one-dimensional, two-phase mathematical model that treats the catalyst layer as a spherical thin file-agglomerate. This method is different from other works that regard it as interface or thin film. Effects of various transport parameters as well as other factors such as catalyst loading, gas diffusion layer thickness and liquid water permeability on the transient evolution of major model properties and cell performance are investigated thoroughly. Numerical results show that the evolution of ionic potential drop and oxygen consumption experience several steps before they reach steady state. The same situation can also be seen for the evolution of water saturation and current density. A close inspection of these phenomena shows a intimate between these transport variables and cell performance. Parametric studies of other design factors' effects reveal there exists optimum values which lead to a greater current output during its evolution period.

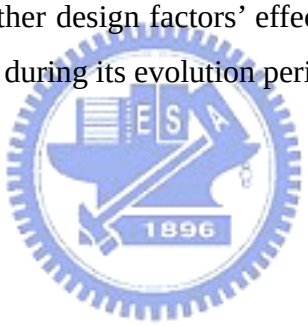

Table of contents

List of tables

List of figures

Nomenclature

a surface area per unit volume,

b Tafel slop,

C_j concentration of species j, $mol \cdot cm^{-3}$

D_j diffusion coefficient of species j, $cm^2 \cdot s^{-1}$

F Faraday constant

H Henry constant, $atm \cdot cm^3 \cdot mol^{-1}$

i current density, $A \cdot cm^{-2}$

k_T oxygen reaction rate constant, s^{-1}

k_c condensation rate,

k_v evaporation rate,

K permeability, cm^2

M molecular weight,

N molar flux of species j, $mol \cdot cm^{-2} \cdot s^{-1}$

P pressure, atm

q switch function

r radius, cm

s liquid water saturation level in porous medium

T temperature, K

Vs cell potential, V

y mole fraction

Greek

α water activity

δ thickness, cm

ε	porosity or volumetric fraction
ϕ	ionic potential, V
φ	Thiele modulus
κ	conductivity, $\Omega^{-1} \cdot cm^{-1}$
λ	water content
μ	viscosity, $g \cdot cm^{-1} \cdot s^{-1}$
ρ	density, $g \cdot cm^{-3}$
τ	tortuosity
ξ	effectiveness factor

Subscripts and Superscripts

agg	agglomerate
CL	catalyst layer
eff	effective
g	gas phase
GDL	gas diffusion layer
MEM	membrane
N	Nafion phase
O_2	oxygen
p	proton
Pt	platinum
sat	saturation
v	vapor water
w	liquid water

.

1. Introduction

1.1. Foreword

Sine 2003, the crude oil price has increased 20% and almost reached $80 per barrel in recent years. (Figure 1-1) As the demand for cost effective and environmentally friendly alternatives of traditional power sources continues to grow, it is becoming evident that future energy generation may be somewhat different from that of the present ones. Many of today's industries, including automotive manufacturers, are investing considerable resources in finding and implementing new technologies to replace traditional power production methods in order to stay competitive in future markets. One of these newly emerging technologies is the fuel cell. Fuel cells, which were invented 167 years ago by William Grove, have only recently become economically competitive with traditional power systems, such as the internal combustion engine.

The fuel cell is an electrochemical device that converts the chemical energy of its reactants directly into electricity and heat, without combustion. Figure 1-2 illustrates the components common to a fuel cell. First, there is a region where reactants can enter and exit the fuel cell. The electrochemical reactions take place at the electrodes, which in most cases are made of porous material to maximize the reaction surface area. In many types of fuel cells, the electrodes contain a catalyst, usually platinum, to facilitate the chemical reactions. The electrodes are connected by an external circuit, through a load. Electrons can follow this circuit from the anode to the cathode of the fuel cell. The electrolyte can be solid or liquid and serves to separate the reactants at the two electrodes and to conduct ions from one electrode to the other. Fuel cells have a substantial range of potential applications, on a power scale from less than a watt to megawatts. The extraordinary environmental quality and high efficiency of fuel cells make them a potential alternative energy source for both stationary and transportation applications. In stationary energy production, fuel cell power plants may have a key role in the transition of the energy economy toward a more distributed, network-type structure. In transportation, fuel cells hold the potential to end the century-long reign of internal combustion engines. Fuel cells have the opportunity to end the carbon-dominated energy system of the 20^{th} century and make the cost of the broadly available hydrogen molecule. While fuel cell technology matures and further research advances are made, the challenge for the fuel cell industry will be to commercialize fuel cell systems by improving their performance and cost. In this chapter, an overview of fuel cell is given, the proton exchange membrane fuel cell (PEMFC) is introduced, a review of existing fuel cell models is discussed, and the objectives of this work are

presented.

1.2. Different types of fuel cells

Fuel cells are usually classified by the nature of the electrolyte they use. Table 1.1 summarizes the major technical differences between them. These distinctions allow one to choose the type of fuel cell that best matches a given application.

As shown in Table 1.1, PEM fuel cells deliver significantly higher power density than the other types of fuel cells, with the exception of the alkaline fuel cell (AFC) and solid oxide fuel cell (SOFC), which have comparable performance. Their electrical efficiency of 40 to 55% is also relatively high in comparison to the efficiency of a spark-ignition internal combustion (IC) engine of comparable size. In addition, the low operating temperature of the PEMFC allows for quick start-up and fast response to changes in electric load. These characteristics, along with their relatively long expected lifetime, make the PEMFC a very suitable power system for vehicular application as well as small stationary power plants. The technical issues involved in a PEMFC will be developed in the next section.

1.3. Proton exchange membrane fuel cell

In comparison to the other types of fuel cells, PEM fuel cells have the shortest start-up time and the highest power density. These properties make PEM fuel cells well suited for portable, automotive and most stationary applications. Thus, the PEM fuel cells have been enthusiastically developed in order to be used in portable devices, such as mobile phones, notebook computers, power tools digital cameras and etc. The proton exchange membrane can operate on reformed hydrocarbon fuels, with pretreatment, and on air. The use of a solid polymer electrolyte eliminates the corrosion and safety concerns associated with liquid electrolyte fuel cells. The anode and cathode are prepared by applying a small amount of platinum black to one surface of a thin sheet of porous, graphitized paper which has previously been wet-proofed with Teflon. Platinum loading have decreased from $5\,mg/cm^2$ to $0.005\,mg/cm^2$.[1] Its low operating temperature provides instant start-up. About 50% of maximum power is available immediately at room temperature. Full operating power is available within about 3 minutes under normal conditions. Recent advances in performance and design offer the possibility of lower cost than any other fuel cell system.

A PEMFC uses a polymer electrolyte membrane usually made of Nafion® (from DuPont), which chemical structure consists of a fluorocarbon polymer with sulfonic acid groups attached. Through this structure, the protons and water molecules are free to migrate. However, the Nafion®

material remains impermeable to reactants (hydrogen at the anode and oxygen at the cathode) and is a good electronic insulator. The carbon fiber material is also referred to as the gas diffusion layer. These components produce a membrane-electrode assembly (MEA). This structure is about hundreds microns thick and the electrodes is about several hundreds microns thick each while the catalyst layers is about tens of micrometers thick each. The components of a PEM fuel cell are shown in Figure 1-3.

The MEA is connected on each side to electronically conductive collector plates, which supply the fuel and the oxidant to the electrodes via gas channels and conduct the current to the external circuit. The reactants are transported by diffusion through the porous electrodes to the reaction site. At the anode, the oxidation of hydrogen fuel releases hydrogen protons that are transported through the membrane and electrons that produce the electrical current. At the cathode, oxygen reacts with the protons and electrons to produce liquid water. The electrochemical reactions are

Anode: $H_2 \leftrightarrow 2H^+ + 2e^-$ (1-1)

Cathode: $2H^+ + \frac{1}{2}O_2 + 2e^- \leftrightarrow H_2O$ (1-2)

The overall reactions is

$H_2 + \frac{1}{2}O_2 \leftrightarrow H_2O$ (1-3)

The operation principle of a PEMFC is described in Figure 1-2.

1.4. Literature survey

The number of published fuel-cell-related models has increased dramatically in the past few years. Not only are there more model being publishing, but they are also increasing in complexity and scope. In this section, an overview of the various fuel cell models is presented.

1.4.1. Zero-dimensional models

0-D models were used to analyze the experimental data. These models normally fit the experimental data with a single equation, and although they demonstrate good fits and are quick and easy to implement, they are less reliable in predicting and explaining behavior. The 0-D modeling equations also can be derived by combination of the governing equations for each regime. The drawbacks of these models are that they do not yield true mechanistic behavior and fundamental understanding and that they are not good for predicting performance or optimization. But they are

valuable for determining kinetic parameters as well as comparing the various losses in the system to one another.

0-D models are very helpful in determining kinetic parameters and general ohmic resistance from experimental data.[2-5] The model of Amphlett et al.[2] accounted for all the temperature dependences through empirical fitting parameters. 0-D models also allow for deviations from the theoretical expression to be investigated. They fitted some experimental data to yield a double Tafel slope at higher current densities. This change in the Tafel slope is caused by mass transport limitations. The equation can not fit the whole polarization curve with just one set of parameter values. Kim et al.[6] incorporated the gas-phase mass transport limitations to their model. The equation yields good fits with the data. Kulikovsky[7] incorporated the limiting current density, thus it is more empirical. Pisani et al. [8], Lufrano et al.[9] and Squadrito et al[10] included the mass-transport limitation to be a more complicated function of current with more fitting parameters.

Of course, all the parameters of models are adjusted for the conditions. As mentioned above, such polarization-equation fits are useful for getting parameter values and perhaps some gross understanding, but they cannot really be used for optimization, prediction, or in-depth examination of the underlying phenomena. It is difficult for them to treat interacting phenomena in a clear way, such as flooding with liquid water.

1.4.2. Fuel cell sandwich modeling

The fuel cell sandwich presents the 1-D across section of the fuel cell, and it includes gas distributors, porous electrodes and membrane. Flow is taken to be normal to the various layers. Additional layers are incorporated into the sandwich, such as separating the porous electrode into microporous layers, gas diffusion layers and catalyst layers. The mass transport and energy transport are through all the various sandwich layers. These processes, include electrochemical kinetics, are key in describing how fuel cell working. Various models for the fuel cell sandwich of the layers are going to be discussed in next section.

1.4.2.1. Gas diffusion layer modeling

The gas diffusion layers are the porous backings between the catalyst layer and the gas channels. The function of them is to

1. act as a gas diffuser;
2. provide mechanical support;

3. provide a pathway for electrons, gases and liquid water.

They are typically carbon-based, and may be in cloth form, a non-woven pressed carbon fiber configuration, or simply a felt-like material. The transport equations are discussed as follow.

For the gas-phase transport, almost every model treats it in the fuel cell sandwich are identically. The Stefan-Maxwell equations are used for the gas transport, and the Bruggeman correlation is adopted to count the effects of porosity and tortuosity.[11-13] Nam and Kaviany[13] discuss the appropriate function to use for the tortuosity, in which changing value due to liquid saturation are also accounted for.

When the pore size decreases to the point where the majority of collisions are between the gas and the pore wall, the Knudsen diffusion becomes the predominant transport mechanism. Some models have begun to take this into account.[14-16] When the pore radius is less then 0.5μm, the Knudsen diffusion is dominant. In the meantime, the diffusion coefficient is a function of the pore radius.[17]

Most models treat the gas-phase flow as diffusion only, but some models take convection term into account.[18-26]. They incorporate the Darcy's law for the gas phase into the momentum equation. Some models of them include the effect of gas-phase pressure-driven flow, because they are often multidimensional. The results of the most models show that the pressure difference through the sandwich is minimal, and the assumption of uniform gas pressure is probably fine for most conditions. Since, the flow parallel to the sandwich and move through the diffusion media primarily by diffusion, because that no-slip condition is adopted. If it uses an interdigitated flow field, the gas-phase pressure-driven flow should be accounted for.

For the liquid water transport, the simplest model is to treat it as a solid species that occupies a certain volume fraction. It reduces the gas porosity, thus the diffusion coefficients of gas species have to correct. The models usually use the volume fraction of water as a fitting parameter.[27-31]. Gurau et al.[30] and Chu et al.[31] used a liquid volume fraction that is a function of position to mimic flooding effects. Gurau et al.[30] developed an analytical solution for a half-cell model. The discrete porosity is adopted for the GDL. They showed how the limiting current density and polarization effects depended on the different liquid volume fraction. Then Chu et al.[31] investigated the effect of the non-uniform porosity of GDL on the performance with various parameters. Such as potential, oxygen mass fraction, and current density.

The more complicated treatment is to develop a two-phase flow in the diffusion media. Several groups are working on it. Nguyen and his co-worker are some of the first researcher to investigate

two-phase flow. They clearly showed how important saturation effects are at the cathode. The two-phase models use empirical expressions for the saturation functions taken from matching experimental data. [1, 21, 32-34] As for the investigation of two-phase flow, Wang et al.[35], at Pennsylvania State University, pioneered the research on this issue through analytic method and computational-fluid-dynamics (CFD) models. A threshold current density was proposed to distinguish the scenarios between single- and two-phase regimes of water distribution and transport. In the subsequent works of their group, sophisticated models [36-42] were developed to simulate the flooding and liquid water distribution in PEM fuel cells. The mature multiphase mixture (M^2) formulation [43, 44] with single set of conservation equations was employed to mimic the two-phase transport process. The modeling domain for this model was basically the cathode side of the fuel cell, where a net water flux through the membrane was assumed. The results showed that it is important to consider the gas-phase pressure field in the GDL as a new mechanism of reactant transport. Another analytic model performed by Pasaogullari et al.[39], focusing on the liquid water transport in hydrophobic electrode, indicated that capillary transport dominates the water remove from flooded GDL. Jang et al. [45] established a two-dimensional, isothermal and multi-phase numerical model to investigate the influence of the GDL parameters on the transport phenomenon and cell performance. The porosity and thickness of the GDL were employed in the analysis as the parameters, and the effects of liquid water and flow direction of the fuel and air on the performance were also considered. Recent reviews by Wang[46] and Weber and Newman[47] provide comprehensive overview of various two-phase PEFC models and address the water management issue with particular attention to GDL in significant details.

Hwang [48] developed a complete two-phase model that cover all two-phase components in a porous cathode of a PEMFC, i.e., velocity (liquid water/gaseous mixture), temperature (reactant fluids/solid matrices), and current (ionic conductor/electronic conductor). The categories of two-phase transports are strongly coupled in an operating fuel cell. The model successfully predicted the phase equilibrium front and the thermal equilibrium front in the cathode of a PEMFC. However, the macroscopic two-phase models are plagued with the scarcity of realistic two-phase correlations, in terms of capillary pressure and relative permeability as functions of water saturation, tailored specifically for actual gas diffusion medium characterized by structures. Due to the lack of reliable two phase correlations, Schulz et al. [49] developed a full morphology (FM) model for studying the two-phase characteristics of the gas diffusion medium. The FM model directly solves for the capillary pressure-saturation relations on the detailed morphology of the reconstructed GDL from drainage simulations.

1.4.2.2. Membrane modeling

Electrolyte is one of the most important parts of a proton exchange membrane fuel cell. It is a proton-conducting membrane, and usually is made of Nafion®. Nafion® is a polymer that falls within the perfluorosulfonic acid family. It is characterized by a backbone structure that is Teflon®-like, i.e., polytetrafluoroethylene, and which has bonded to it a perfluorinated side chain that has a terminal sulfonic acid group (SO_3^-). The function of the ion exchange membrane is to provide a conductive path while at the same time separating the reactant gases. The material is an electrical insulator. As a result, ion conduction takes place via ionic groups within the polymer structure. Ion transport is highly dependent on the bound and free water associated with those sites.

There have been many microscopic models and physical models in addition to the macroscopic ones. The microscopic models examined single ions and pore-level effects. The macroscopic models are often more empirical and focus on describing the transport in a macrohomogeneous medium. For the macroscopic models, there two main categories, one is single phase and the other is two phases. Membrane, protons, and water are the main components in the models. They neglected the hydrogen crossover or oxygen crossover in the membrane. The microscopic models provide the fundamental understanding of processes such as diffusion and conduction in the membrane on single-pore level. They allow for the evaluation of how small perturbations like heterogeneity of pores and electric fields affect transport, as well as the incorporation of small-scale effects.

Weber and Newman [50-53] developed a physical model of transport in Nafion, which could be used as a foundation for a macrohomogeneous model. They focus on how the membrane structure changes as a function of water content, where λ is the moles of water per mole of sulfonic acid sites and is measured by examining the weight gain of an equilibrated membrane. In the physical model, there are two separate structures for the membrane depending on whether the water at boundary is vapor or liquid. These are termed the vapor- or liquid-equilibrated membrane respectively. When the channels are collapsed, it is a vapor-equilibrated membrane. When they are expanded and filled with water, it is a liquid-equilibrated membrane.

For a single phase membrane, the diffusive models are adopted. They correspond with more-or-less to the vapor-equilibrated membrane. Because the collapse channels fluctuate and there are not any true pores, it is easy to treat the system as a single, homogeneous phase in which water and protons dissolve and move by diffusion. Since the membrane is stationary, only the water and protons move in the membrane system. The simplest models for a membrane either neglect the

water movement or treat it as a known constant. For the proton transport, the Ohm's law is the simplest treatment. This can easily be integrated to yield a resistance for use in a polarization equation.[1, 2, 13, 21, 24, 31, 33, 35, 54-56]

For the transport parameters in the membrane are the functions of temperature and the water content, λ. [52]. In the models, empirical fits are used [19, 22, 27, 57-60] or the properties are assumed constant.[4, 15, 25, 61] Weber and Newman [47, 52] review many of the data and discuss the functional forms for the properties from a physical view. Schroeder's paradox is an observed phenomenon that needs to be considered in any model when the membrane is not either fully hydrated or dehydrated. There are various approaches to account for Schroeder's paradox. The easiest approach is to ignore it, which a majority of the models do. Next, it can be treated as a discontinuity or by assuming a functional form of the water content and water activity continue to increase.[15, 19, 20, 22, 57, 60, 62, 63] In the model of Springer et al.[27], was used as the driving force for water flown in the membrane, and an activity coefficient was used to account for the isothermal behavior. The approach of Wang and Savinell[58]'s is identical to Springer et al.'s.

For the two-phase membrane, the model corresponds to the liquid-equilibrated membrane. The membrane is treated as having pores that are filled with liquid water. This sustains a pressure gradient in the water because of a stress relation between the membrane and fluid at every point in the membrane. Bernardi and Verbrugge [64, 65] developed a membrane model for it. They utilized a dilute solution approach that used the Nernst-Plank equation to describe the proton transport. There are two models of water transport are operative: the electro-osmotic drag effect and diffused by the concentration gradient. The water flux due to the electro-osmotic drag is directly proportional to the protonic flux. The diffusion flux of water in the membrane is usually described by a water diffusion coefficient and the gradient in molar concentration of water.

1.4.2.3. Catalyst layer modeling

The catalyst layer is platinum-based for both the anode and cathode. To promote hydrogen oxidation reaction and the anode uses either pure platinum metal catalyst or a supported platinum catalyst, typically on carbon or graphite for pure hydrogen feed steams. Oxygen reduction reaction at the cathode may use the platinum metal or the supported catalyst. For the HOR, the reaction is fast and can be described by a Bulter-Volmer kinetic expression. For the ORR, a Tafel equation is normal used.

The catalyst layer is very complex, because the electrochemical reactions take place there, and all the different types of phases exist. Thus, the membrane models and gas diffusion layer models must be used in the catalyst layer along with additional expression related to the electrochemical kinetics on the supported electro-catalyst particles. There are many approaches for studying the catalyst layer. An examination of the catalyst layer models reveals the fact that there are more cathode models than anode ones. Because the cathode has the slower reaction, it is where water is generated, and mass transfer effects are more significant. The anode can almost always be modeled as a simplified cathode model. The simplest approach is interface model, where a single equation is used. It is infinitely thin, and their structure can be neglected. This approach is used in complete fuel cell models where the emphasis of the model is not on the effects of catalyst layer.[13, 15, 16, 27, 53, 66, 67] If takes it as an interface, the results will be higher. The next set of models is the homogeneous models [64, 65, 68-70]. In the homogeneous model, it is assumed that the electrode active layer consists of a uniform, gas pore-free blend of proton conducting polymer and supported catalyst. The suitability of the homogeneous model for describing state-of-the-art PEM fuel cell cathode has been criticized.[28, 71, 72] Besides these models, the works of Wang et al. [73, 74] treated the catalyst layer as an individual zone with various conservation equations employed in the modeling of transient study and various time constants for the transient transport phenomena were proposed. It predicts too poor oxygen permeability properties as compared to experimental results.

Experimental study and microscopic analysis [25, 71, 75] showed that the catalyst layer is porous and the reactants can transport through the catalyst layer in the gas phase. In order to account for this phenomenon, the so-called thin-film model and agglomerate model have been proposed. In the thin-film model [55, 76], the catalyst particles are covered by a polymer electrolyte film, and the gas pores only exist within the electrode. The thickness of the film is uniform and is very small in comparison to the pore size. The model of Bultel et al.[76]'s was developed for taking into account simultaneously the couple effects of diffusion and ohmic drops. They suggested that the local effects are mainly masked for oxygen reduction in acidic medium, and these effects are no more negligible for hydrogen oxidation.

In the agglomerate model [25, 68, 71, 72, 75, 77-79], the catalyst particles, electrolyte and gas pores form a homogeneous mixture. For the analysis, the effectiveness factor is used. For spherical agglomerate, an analytic expression is

$$\xi = \frac{1}{\varphi}\frac{3\varphi\coth(3\varphi)-1}{3\varphi} \tag{1-4}$$

φ is the Thiele modulus[80]

$$\varphi = r_{Agg}\sqrt{\frac{k_T}{D_{O_2,eff}}} \tag{1-5}$$

When the Thiele modulus is large, diffusion usually limits the overall rate of reaction. While it is small, the surface reaction is usually rate-limiting. The results of the simple agglomerate models are helpful in trying to understand and optimize catalyst layer parameters such as catalyst loading and agglomerate size. The agglomerate model has many parameters that should be used to fit experimental data. Such as the agglomerate size and surface oxygen concentration. Several researchers had compared them to each other and experimental data. Broka and Ekdunge[71] suggest that the agglomerate model is more accurate. Gloaguen et al.[77] also showed the agglomerate model is more suitable compared to the flooded thin-layer model in terms of describing the catalyst layer.

The National Research Council of Canada research group [81-89] had a series of investigation on the structures of catalyst layers with different types of agglomerate and optimizations of the cathode catalyst layer. However, their model only considers a single phase in catalyst layer or cathode side, while in reality multiphase of catalyst layers should be considered. For the flooding of the catalyst layer, there are various models have addressed. There are two main ways which depend on how the catalyst layer is modeled. If an agglomerate model is used and liquid water exists. A liquid film covering the membrane of the agglomerates can be assumed. Thus, the flooding of the catalyst layer is easily incorporated into the external mass transfer limitation.[29, 69] Because the low diffusivity and solubility of oxygen in water, only a very thin liquid film is needed to inhibit reaction. The thickness of the film used as a fitting parameter. The other approach is to use the two-phase modeling which described in the gas diffusion layer modeling. This involves calculating the liquid water saturation in the catalyst layer. The liquid water occupied the gas pore, and reduces the gas porosity. There are a few models that use this approach.[21, 33-35, 90, 91] Lin et al.[91] developed a one-dimensional thin film-agglomerate model for the catalyst layer in the steady state. They showed that the liquid water accumulation within the gas diffusion layer and catalyst layer had a significant impact on the cell performance. Lin and Nguyen [92] extended their one-dimensional model to a two-dimensional to account for the effect of the relative dimensions of the shoulders and channels on the cell performance. The effects of the in-plane liquid water permeability and electronic conductivity of the gas diffusion layer on cell performance were also examined. It was found that more channels, smaller shoulder widths on the gas distributor, and

higher in-plane water permeability of the gas diffusion layer can enhance the transport of liquid water and oxygen, leading to better cell performance.

1.5. Motivation and objectives

Due to the facts, a PEM fuel cell is the most promising candidates which are suitable for portable power source applications. Its low cost per kW is very important for mobile applications. PEM fuel cells for these applications must be working constantly under highly dynamic loading. The promotion of the fuel cell performance is ipod-like nowadays. However, most of the recent researches are based on the steady state scenario. In actual situation, it is put in use to portable devices with highly dynamic loading. Therefore, to enhance the understanding on the underlying transport and performance characteristics of the PEM fuel cell, a transient model investigation is necessary and important. Furthermore, a comprehensive knowledge is able to be obtained through conducting a parametric study of various vital design parameters of the PEM fuel cell and optimal parameters for the best performance can be obtained accordingly.

The objective of this dissertation is to develop a transient model describing the transport process of gaseous species, liquid water and protons with a thin film-agglomerate approach to model the catalyst layer structure. An overview of the transient, two-phase, one-dimensional model of a PEM fuel cell cathode is described in Chapter 2. And the effect of operating parameters that affect the water generation and removal process, such as the inlet relative humidity of the cathode streams and operating temperature is studied. In this dissertation, it investigates the transient state and emphasis on the start-up. In Chapter 3, it presents the interactions between each parameter and the cell performance in transient state. The porosity effect, catalyst layer thickness effect and agglomerate radius effect are discussed. In Chapter 4, the catalyst pellets in the catalyst layer are treated as spheres. And a spherical thin film-agglomerate model is developed.

Table 1-1. Characteristics of different types of fuel cells.

Fuel cell type	PEMFC	DMFC	AFC	PAFC	MCFC	SOFC
Mobile Ion	H^+	H^+	OH^-	H^+	CO_3^{2-}	O^{2-}
Operating temperature (^oC)	50-100	50-200	50-200	~220	~650	600-1000
Power density (kW/m^2)	3.8-2.6	>1.5	0.7-8.1	0.8-1.9	0.1-1.5	1.5-2.6
Electrical 1st law efficiency (%)	40-55 (stack)	40 (stack)	45-60 (stack)	40-50 (stack) 41 (system)	50-60 (system)	50-65 (stack) 45-50 (system)
Start-up time	Sec-min	Sec-min	Min	Hours	Hours	Hours

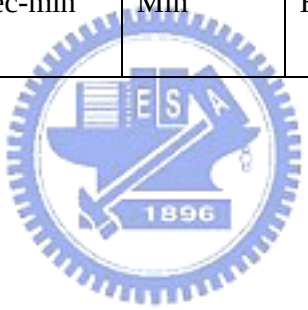

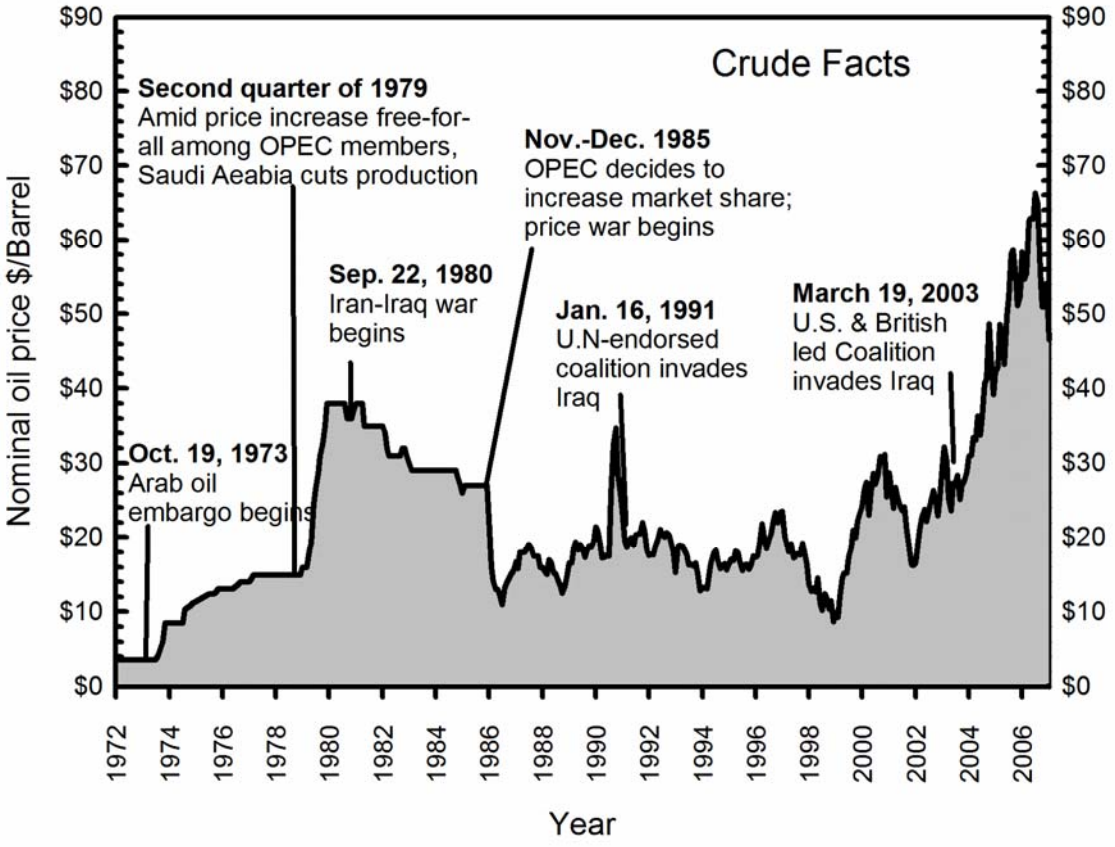

Fig 1-1. Crude oil price Jan. 1972 ~ May 2007

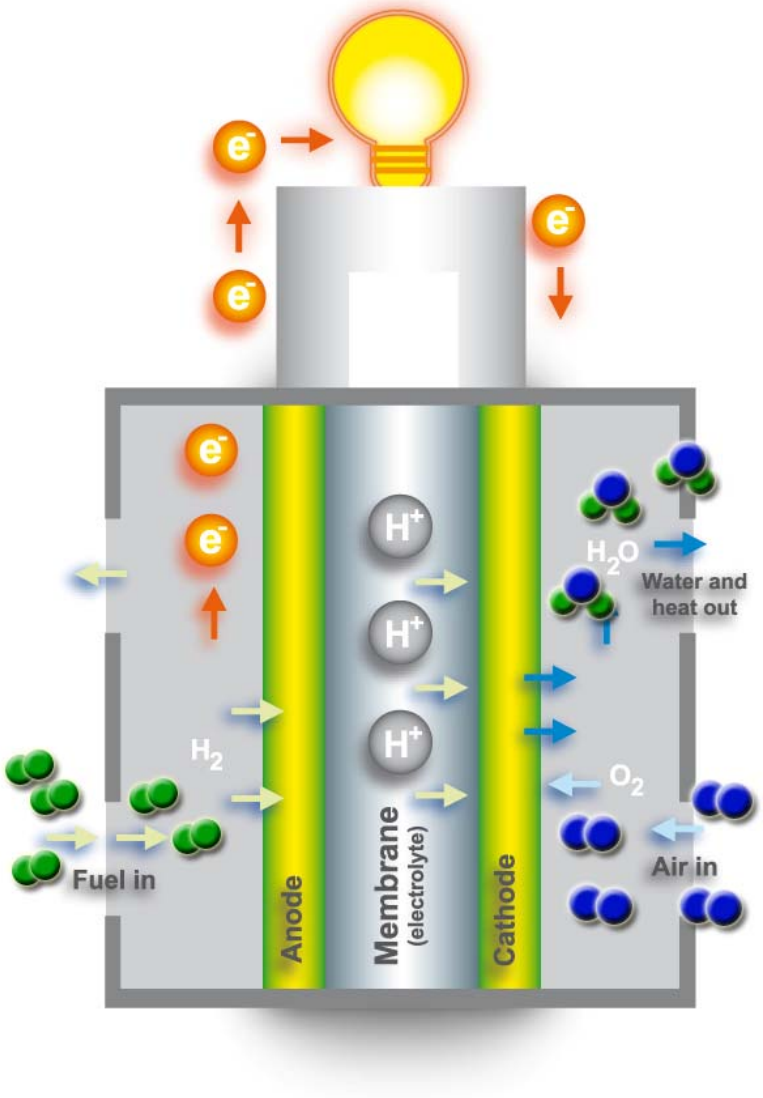

Fig 1-2. An illustration of a fuel cell.

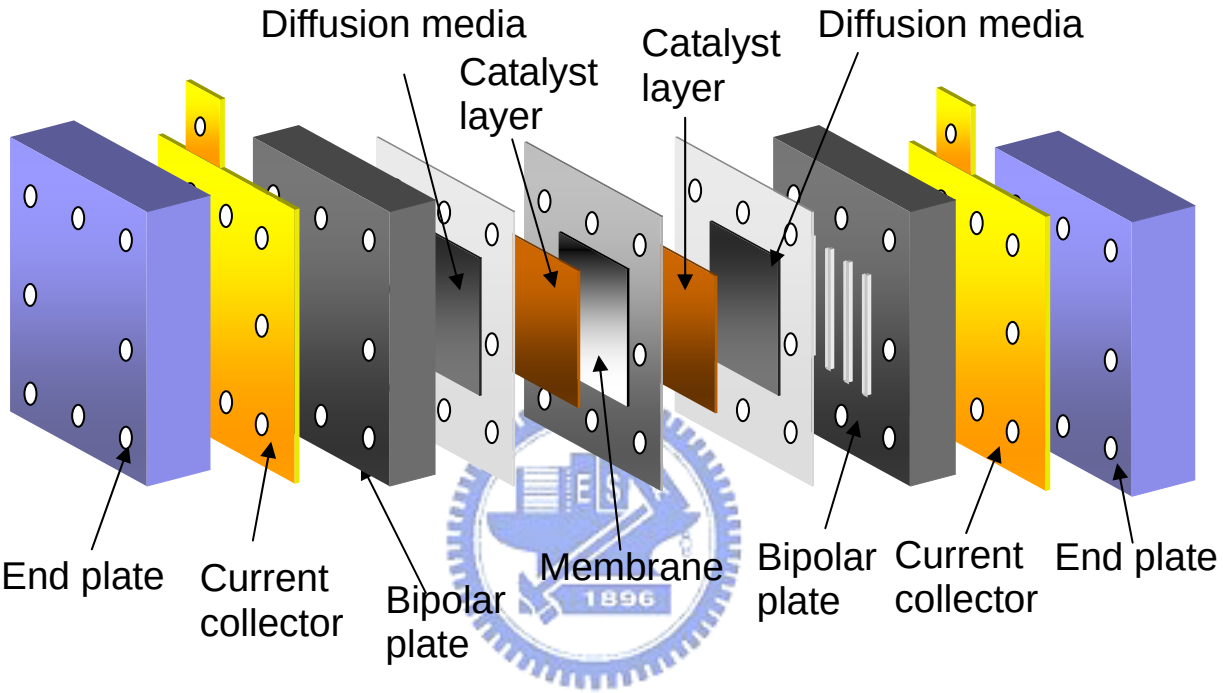

Fig 1-3. Component diagram of a PEM fuel cell

2. Transient analysis of PEM fuel cells based on a cylindrical thin film-agglomerate approach

This chapter is devoted to investigate the transient, two-phase, multi-component transport as well as electrochemistry behavior of the PEMFC. The transient model is extended from the steady state model developed by Lin et al.[91] (Figure 2-1). It includes the transport of gaseous species, liquid water, proton, and electrochemical kinetics in the cathode of a PEMFC. The catalyst pellet is consisted of carbon-supported platinum catalyst and Nafion ionomer and is covered with a thin Nafion film. In this chapter, they are treated as cylindrical objects. The Nafion-filled spaces among the catalyst pellets form the channels which have the functions of transporting reactant and product. The oxygen flows from gas channel to the catalyst layer via the gas diffusion layer. It is assumed to diffuse constantly along the catalyst layer. In the meantime, the oxygen dissolves into the Nafion film and reaches the pellet surface. Then, the liquid water is generated through the oxygen reduction reaction.

2.1. Assumptions

The following assumptions are made to simplified the modeling.

1. The gas phase obeys the ideal gas law.
2. In the GDL and CL, the electronic resistance is negligible.
3. Bruggeman correlation is used to count for the effects of porosity and tortuosity.
4. The radius of the catalyst pellet and the thickness of the Nafion film are uniform in the catalyst layer.
5. The catalyst pellets are treated as homogeneous and oxygen diffuses into pellets via Nafion film.
6. The Thiele modulus approach is applied.
7. The oxygen reduction reaction generates liquid phase water.

The ionic potential between the anode catalyst layer and the membrane is approximately zero because of the fast reaction rate of hydrogen oxidation.

There are five variables employed in this chapter as blow:

(1). The concentration of oxygen in the gas phase, [$C_{O_2}^g$].

(2). The concentration of vapor water in the gas phase, [C_v^g].

(3). The liquid water saturation level, [s]. (the ratio between the liquid water volume and the total void volume in the porous medium)

(4). The concentration of liquid water in Nafion phase, [C_w^N].

(5). The ionic potential, [ϕ] (potential in Nafion phase).

2.2. Governing equations

2.2.1. Governing equations in the gas diffusion layer

The mass conservation equation for the oxygen is

$$\frac{\partial}{\partial \mathrm{t}}\left(\left(1-s\right)\varepsilon_0^{GDL}C_{O_2}^g\right)=\mathrm{D}_{\mathrm{O}_2}\varepsilon_0^{\mathrm{GDL}^\tau}\left[\left[\left(1-s\right)\right]^\tau\nabla^2C_{O_2}^g+\nabla\cdot\left[\left(1-s\right)\right]^\tau\nabla\cdot C_{O_2}^g\right] \tag{2-1}$$

LHS is the oxygen concentration's increasing rate with time. ε_0^{GDL} is the porosity of gas diffusion layer. The liquid water in GDL reduces the gas porosity, so that the term $\left(1-s\right)$ is employed to consider this phenomenon. RHS is a diffusion term, describing the oxygen molar flux, and τ is tortuosity of the porous medium.

The mass conservation equation for the vapor water in the gas phase is

$$\frac{\partial}{\partial \mathrm{t}}\left(\left(1-s\right)\varepsilon_0^{GDL}C_v^g\right)=\mathrm{D}_{\mathrm{v}}\varepsilon_0^{\mathrm{GDL}^\tau}\left[\left[\left(1-s\right)\right]^\tau\nabla^2C_v^g+\nabla\cdot\left[\left(1-s\right)\right]^\tau\nabla\cdot C_v^g\right]-\mathrm{R}_{\mathrm{w}} \tag{2-2}$$

LHS is the concentration of vapor water. The 1st term of the RHS is the diffusion term. 2nd term is a source term. R_w is the interfacial transfer rate of water between liquid and vapor water.

$$R_w=k_c\frac{\varepsilon_0^{GDL}\left(1-s\right)y_v}{RT}\left(y_vP-P_v^{sat}\right)q+k_v\frac{\varepsilon_0^{GDL}s\rho_w}{M_w}\left(y_vP-P_v^{sat}\right)\left(1-q\right) \tag{2-3}$$

where k_c and k_v are the condensation rate and evaporation rate constants respectively; y_v is the molar fraction of vapor water in the gas phase; P and P_v^{sat} are the operating pressure and water vapor saturation pressure respectively. M_w and ρ_w are the molecular weight and density of liquid

water respectively. q is a switch function and is defined as,

$$q = \frac{1 + \left| y_v P - P_v^{sat} \right| \Big/ \left(y_v P - P_v^{sat} \right)}{2} \tag{2-4}$$

The liquid water transport in the GDL and CL is driven by capillary force. Darcy law is used to describe the flow of the liquid water in the porous media.

$$N_w = -\frac{\rho_w K_w(s)}{M_w \mu_w} \nabla P_l \tag{2-5}$$

P_l is the pressure of liquid water, and K_w is permeability of liquid water. Since

$$P_l = P_g - P_c \tag{2-6}$$

P_g is the gas phase pressure and is a constant over the domain. Eq. (2-5)becomes

$$N_w = -\frac{\rho_w K_w(s)}{M_w \mu_w} \nabla(-P_c) \tag{2-7}$$

The relation between the liquid water permeability and saturation level is linear [1].

$$K_s(s) = K_{w,0} s \tag{2-8}$$

$K_{w,0}$ is the permeability of liquid water at 100% saturation level. Thus,

$$N_w = -\frac{\rho_w K_{w,0}}{M_w \mu_w} \left(-\frac{dP_c}{ds} \right) s \nabla s \tag{2-9}$$

$\left(-\frac{dP_c}{ds} \right)$ is treated as a constant in order to reduce the total number of adjustable fitting parameters, and different values are used for different porous media, such as the GDL and CL. Therefore, the transport equation of liquid water saturation level is

$$\frac{\varepsilon_0^{GDL} \rho_w}{M_w} \frac{\partial s}{\partial t} = \frac{\rho_w K_{w,0}}{M_w \mu_w} \left(-\frac{dp_c}{ds} \right) \left(s \nabla^2 s + (\nabla \cdot s)^2 \right) + R_w \tag{2-10}$$

The mass conservation equation of the concentration of liquid water in the Nafion phase is

$$\varepsilon_m^{GDL}\frac{\partial C_W^N}{\partial t}=D_w^N\nabla^2 C_w^N \tag{2-11}$$

RHS is a diffusion term. D_w^N is the diffusivity of liquid water in the Nafion phase and is function of the water content as listed in Table 2-1.

2.2.2. Governing equations in the catalyst layer

The mass conservation equation of oxygen in the gas phase is

$$\frac{\partial}{\partial t}\left(\left(1-s\right)\varepsilon_0^{CL}C_{O_2}^g\right)=D_{O_2}\varepsilon_0^{CL^\tau}\left[\left[\left(1-s\right)\right]^\tau\nabla^2 C_{O_2}^g+\nabla\cdot\left[\left(1-s\right)\right]^\tau\nabla\cdot C_{O_2}^g\right]-R_{O_2} \tag{2-12}$$

It is similar to the equation in the GDL, but the last term in RHS. The electrochemical reacts in the catalyst layer. R_{O_2} is a source term, but then oxygen is consumed in the CL. The scheme of the catalyst pellet domain contains the gas phase, water film and Nafion phase as shown in the Figure 2-2.

Oxygen dissolves into the water film first at interface 1 and then diffuses through the water film, across the interface 2. And then through the Nafion film to reach the interface 3. At the interface 1 and 2, the oxygen concentration in different phases obeys Henry's law. The expression for oxygen between air and phase i is

$$P_{O_2}^g=H_{O_2}^{i,g}C_{O_2}^i \tag{2-13}$$

$H_{O_2}^{i,g}$ is the Henry's constant for oxygen between air and phase i. Therefore at interface 1, the concentration of oxygen is

$$C_{O_2,1}^w=\frac{RT}{H_{O_2}^{w,g}}C_{O_2}^g \tag{2-14}$$

At interface 2, oxygen is equilibrium with both liquid water and Nafion.

$$C_{O_2,2}^w=\frac{H_{O_2}^{N,g}}{H_{O_2}^{w,g}}C_{O_2,2}^N \tag{2-15}$$

The flux of oxygen through the water film and Nafion film are

$$N_{O_2}^{W} = -D_{O_2}^{W}\frac{C_{O_2,1}^{w} - C_{O_2,2}^{w}}{\delta_w}$$
$$N_{O_2}^{N} = -D_{O_2}^{N}\frac{C_{O_2,2}^{N} - C_{O_2,3}^{N}}{\delta_N} \tag{2-16}$$

And from the continuity equation

$$N_{O_2}^{W}\, a_r\big|_2 = N_{O_2}^{N}\, a_r\big|_3 = -R_{O_2}^{p} \tag{2-17}$$

$$a_r\big|_1 \approx a_r\big|_2 \approx a_r\big|_3 = a_r \tag{2-18}$$

a_r is the outer surface area of agglomerates per catalyst layer unit volume.

$$a_r = \frac{2}{r_{Agg} + \delta_N}\left(1 - \varepsilon_0^{CL}\right) \tag{2-19}$$

By using the effectiveness factor and Thiele modulus approach, the oxygen reaction rate within the catalyst pellet can be expressed in terms of the oxygen concentration on the surface of the catalyst pellet. That is, at interface 3

$$R_{O_2}^{P} = \xi k_p \left(1 - \varepsilon_0^{CL}\right) C_{O_2,3}^{N} \tag{2-20}$$

It assumes that $k_T = k_p\left(1-\varepsilon_0^{CL}\right)$, then $R_{O_2}^{p} = \xi k_T C_{O_2,3}^{N}$. The concentration of oxygen at the surface of catalyst pellet is

$$C_{O_2,3}^{N} = \frac{a_r \dfrac{D_{O_2}^{N}}{\delta_N}\dfrac{D_{O_2}^{w}}{\delta_w}\dfrac{RT}{H_{O_2}^{w,g}} C_{O_2,2}^{g}}{\xi k_T \dfrac{D_{O_2}^{w}}{\delta_w}\dfrac{H_{O_2}^{N,g}}{H_{O_2}^{w,g}} + \xi k_T \dfrac{D_{O_2}^{N}}{\delta_N} + a_r \dfrac{D_{O_2}^{w}}{\delta_w}\dfrac{D_{O_2}^{N}}{\delta_N}\dfrac{H_{O_2}^{N,g}}{H_{O_2}^{w,g}}} \tag{2-21}$$

Substituting into $R_{O_2}^{p} = \xi k_T C_{O_2,3}^{N}$, rearranging and dropping off the superscript p,

$$R_{O_2} = \frac{\dfrac{RT}{H_{O_2}^{N}}}{\dfrac{\delta_N}{a_r D_{O_2}^{N}} + \dfrac{\delta_w}{a_r D_{O_2}^{w}} + \dfrac{1}{\xi k_T}} C_{O_2}^{g} \tag{2-22}$$

$H_{O_2}^{N}$ and $H_{O_2}^{W}$ are the Henry's constants. $H_{O_2}^{N}$ is the oxygen between air and the Nafion phase and $H_{O_2}^{W}$ is the oxygen between air and liquid water. δ_N is the thickness of the Nafion film. $D_{O_2}^{N}$ is

the diffusivity of oxygen in the Nafion, and $D_{O_2}^{w}$ is the diffusivity of oxygen in the liquid water. r_{Agg} is the radius of a catalyst pellet. Liquid water forms a film around the top of Nafion film. If it is not evaporated, its thickness can be estimated by

$$\delta_w = \frac{\varepsilon_0^{CL} s}{a_r} \tag{2-23}$$

The reaction rate constant

$$k_T = \left(1-\varepsilon_0^{CL}\right)\frac{1}{4FC_{O_2,eff}} a_{Pt}^{agg} i_0 \exp\left[-\frac{2.303\left(V_s-\phi-U_{ref}\right)}{b}\right] \tag{2-24}$$

The active catalyst surface area per unit volume of agglomerates

$$a_{Pt}^{agg} = \frac{a_{Pt} m_{Pt}}{\delta_{CL}\left(1-\varepsilon_0^{CL}\right)} \tag{2-25}$$

a_{Pt} is the surface area per mass. m_{Pt} is the catalyst loading of the electrode. δ_{CL} is the thickness of catalyst layer and b is the Tafel slope.

The effectiveness factor

$$\xi = \frac{1}{\varphi}\frac{3\varphi\coth\left(3\varphi\right)-1}{3\varphi} \tag{2-26}$$

The Thiele modulus

$$\varphi = \frac{r_{Agg}}{2}\sqrt{\frac{k_T \Big/ \left(1-\varepsilon_0^{CL}\right)}{D_{O_2,eff}^{N}}} \tag{2-27}$$

$D_{O_2,eff}^{N}$ is the effective diffusivity of oxygen in the Nafion phase within the catalyst pellets.

$$D_{O_2,.eff}^{N} = D_{O_2}^{N}\left[\left(1-\varepsilon_0^{CL}\right)\varepsilon_N^{P}\right]^{\tau} \tag{2-28}$$

ε_N^P is the volumetric fraction of Nafion within the catalyst pellets.

The mass conservation equation of vapor water in the gas phase is

$$\frac{\partial}{\partial \mathrm{t}}\left(\left(1-s\right)\varepsilon_0^{CL}C_v^g\right)=\mathrm{D_v}\varepsilon_0^{\mathrm{CL}^r}\left[\left[\left(1-s\right)\right]^\tau\nabla^2C_v^g+\nabla\cdot\left[\left(1-s\right)\right]^\tau\nabla\cdot C_v^g\right]-\mathrm{R_w} \tag{2-29}$$

The transport equation of liquid water saturation level is

$$\frac{\varepsilon_0^{CL}\rho_w}{M_w}\frac{\partial s}{\partial t}=\frac{\rho_w K_{w,0}}{M_w\mu_w}\left(-\frac{dp_c}{ds}\right)\left(s\nabla^2 s+\left(\nabla\cdot s\right)^2\right)+R_w+\left(4n_d^{CL}+2\right)R_{O_2} \tag{2-30}$$

It is similar to the equation in the GDL, but the last term is generated by electrochemical reaction and electro-osmotic effect. n_d^{CL} is the net electro-osmotic drag coefficient and is a functions of the water content as listed in Table 2-1.

The mass conservation equation for the concentration of liquid water in Nafion phase is the same as the equation in GDL.

The flux expression of charges in the catalyst layer is

$$i_p=-\kappa_{N,eff}\nabla\phi \tag{2-31}$$

The conservation equation of ionic current is

$$\kappa_{N,eff}\nabla^2\phi-4FR_{O_2}=0 \tag{2-32}$$

It is based on the stoichiometry of the oxygen reduction reaction. The consumption rate of protons is proportional to the reaction rate of oxygen $\kappa_{N,eff}$ is the effective electric conductivity of the Nafion phase.

$$\kappa_{N,eff}=\kappa_N\left[\left(1-\varepsilon_0^{CL}\right)\varepsilon_N^P\right]^\tau \tag{2-33}$$

2.2.3. Governing equations in the membrane

In the membrane, the liquid water transport is driven by the water concentration gradient and electro-osmotic drag. The concentration of the liquid water in the Nafion phase is

$$\varepsilon_m\frac{\partial C_W^N}{\partial t}=D_w^N\nabla^2C_w^N+\frac{n_d\kappa_N}{F}\nabla^2\phi \tag{2-34}$$

κ_N is the bulk electric conductivity in the Nafion phase and is function of the water content as listed in table 2-1.

In the anode, protons are produced and transported through the membrane to the catalyst layer. The flux expression of charges in the membrane is

$$i_p = -\kappa_N \nabla \phi \tag{2-35}$$

The electrochemical reaction does not react in the membrane. The equation of ionic current is

$$\nabla^2 \phi = 0 \tag{2-36}$$

2.3. Initial and boundary conditions

The simplification of all the differential equations and closure relations (governing and constitutive equations) previously presented allows one to write a system of five differential equations in the cathode of a PEMFC. Thus, one has to solve for 5 constitutive variables:

(1). The concentration of oxygen in the gas phase, [$C_{O_2}^g$].

(2). The concentration of vapor water in the gas phase, [C_v^g].

(3). The liquid water saturation level, [s]. (the ratio between the liquid water volume and the total void volume in the porous medium)

(4). The concentration of liquid water in Nafion phase, [C_w^N].

(5). The ionic potential, [ϕ].

To denote the location of a particular interface, the following notation will be used for subscripts in the expression of boundary conditions:

(1). The first letter symbolizes the domain:

GDL : gas diffusion layer,
CL : catalyst layer,
MEM : membrane.

(2). The second indicates the side of the interface:

\+ : higher values of x-coordinates, perpendicular to the surface,
\- : lower values of x-coordinates, perpendicular to the surface.

Oxygen concentration in the gas phase [$C_{O_2}^g\left(t,x\right)$]

The mass conservation equation for oxygen requires one initial condition and 4 boundary conditions

The initial condition is assumed to be zero. Thus,

$$C_{O_2}^{g}\left(0,x\right)=0 \tag{2-37}$$

At the gas channel boundary, we assume that inlet gas is air. Thus,

$$C_{O_2}^{g}\left(t,0\right)=C_{O_2}^{air} \tag{2-38}$$

At the interface between the GDL and CL, both the oxygen concentration and the oxygen flux are continuous so that,

$$C_{O_2}^{g}\Big|_{t,x=GDL^-}=C_{O_2}^{g}\Big|_{t,x=GDL^+} \tag{2-39}$$

$$N_{O_2}^{g}\Big|_{t,x=GDL^-}=N_{O_2}^{g}\Big|_{t,x=GDL^+} \tag{2-40}$$

At the interface between the CL and the membrane, it is assumed that no oxygen leaves, i.e.

$$N_{O_2}^{g}\Big|_{t,x=CL^-}=0 \tag{2-41}$$

Vapor water concentration in the gas phase [$C_v^g\left(t,x\right)$].

The mass conservation equation for the concentration of vapor water requires one initial condition and 4 boundary conditions. The initial condition is assumed to be zero. Thus,

$$C_{v}^{g}\left(0,x\right)=0 \tag{2-42}$$

At the gas channel boundary, we assume that inlet gas is air. Thus,

$$C_{v}^{g}\left(t,0\right)=C_{v}^{air} \tag{2-43}$$

At the interface between the GDL and CL, both the oxygen concentration and oxygen flux are continuous so that,

$$C_{v}^{g}\Big|_{t,x=GDL^-}=C_{v}^{g}\Big|_{t,x=GDL^+} \tag{2-44}$$

$$N_{v}^{g}\Big|_{t,x=GDL^-}=N_{v}^{g}\Big|_{t,x=GDL^+} \tag{2-45}$$

At the interface between the CL and the membrane, it is assumed that vapor water cannot permeate into the membrane, i.e.

$$N_{v}^{g}\Big|_{t,x=CL^-}=0 \tag{2-46}$$

Saturation level of liquid water in porous media [$s(t,x)$]

The transport equation for the liquid water saturation level requires one initial condition and 4 boundary conditions. As to the initial condition, the saturation level profile is assumed to be zero, thus

$$s(0,x)=0 \tag{2-47}$$

At the gas channel boundary, it is assumed that there is no liquid water, i.e.

$$s(t,0)=0 \tag{2-48}$$

At the interface between the GDL and CL, it is assumed that the saturation level and liquid water flux is continuous. Thus,

$$s\big|_{t,x=GDL^-} = s\big|_{t,x=GDL^+} \tag{2-49}$$

$$N_w\big|_{t,x=GDL^-} = N_w\big|_{t,x=GDL^+} \tag{2-50}$$

At the interface between the CL and the membrane, the flux of liquid water saturation level is assumed to be zero.

$$N_w\big|_{t,x=CL^-} = 0 \tag{2-51}$$

Concentration of liquid water in Nafion phase [$C_w^N(t,x)$]

The mass conservation equation for the concentration of liquid water in Nafion phase requires one initial condition and 6 boundary conditions. As the initial state, the Nafion phase had fully hydrated. Thus the concentration of liquid water in Nafion phase is assumed to be in equilibrium with the vapor water activity in the gas phase, i.e.

$$C_w^N(0,x) = C_{w(anode)}^{N,eq} \tag{2-52}$$

$$C_{w(anode)}^{N,eq} = C_f\left(0.043+17.81\alpha-39.85\alpha^2+36.0\alpha^3\right) \tag{2-53}$$

There is not any Nafion phase in the gas channel, thus

$$C_w^N(t,0)=0 \tag{2-54}$$

At the interface between the GDL and CL, both the concentration and flux are continuous, i.e.

$$C_w^N\Big|_{t,x=GDL^-} = C_w^N\Big|_{t,x=GDL^+} \tag{2-55}$$

$$N_w^N\Big|_{t,x=GDL^-} = N_w^N\Big|_{t,x=GDL^+} \tag{2-56}$$

At the interface between the CL and the membrane, both the concentration and flux are continuous.

$$C_w^N\Big|_{t,x=CL^-} = C_w^N\Big|_{t,x=CL+} \tag{2-57}$$

$$N_w^N\Big|_{t,x=CL^-} = N_w^N\Big|_{t,x=CL+} \tag{2-58}$$

At x=L, the concentration of liquid water in membrane is assumed to be in equilibrium with the vapor water activity in the gas phase.

$$C_w^N\Big|_{t,x=L} = C_{w(anode)}^{N,eq} \tag{2-59}$$

Ionic potential [$\phi(t,x)$]

The potential equation requires 4 boundary conditions. At the GDL boundary, the ionic current is zero.

$$i_p\Big|_{x=GDL^+} = 0 \tag{2-60}$$

At the interface between the CL and the membrane, the ionic potential and ionic current are continuous. Thus,

$$\phi\Big|_{x=CL^-} = \phi\Big|_{x=CL^+} \tag{2-61}$$

$$i_p\Big|_{x=CL^-} = i_p\Big|_{x=CL^+} \tag{2-62}$$

At x=L, the ionic potential is zero.

$$\phi\Big|_{x=L} = 0$$

2.4. Methods of solution

The governing equations solved in the domain are in the form of transient second order, parabolic differential equations with variable coefficients. Because of the complexity of these equations, they cannot be solved analytically. However, they can be solved numerically using a finite difference method used approximates each derivative and coefficient in each of the partial differential equations. The following is a description of the finite difference scheme used to solve the system of coupled equations presented in section 2.2.

2.4.1. Difference operators

In finite difference schemes, the derivatives that occur within the equation being solved are approximated using finite difference operators. In order to derive these operators, one must first partition the x (spatial direction) and the t (time dimension) plane into uniform cells Δx by Δt with cell spacing $\Delta x = 1/J$ and $\Delta t = 1/N$. An example is shown in Figure 2-3.

After grid spacing has been established in the general terms depicted in Figure 2-3, derivatives are approximated using the system of line intersections (nodes) shown. Taylor's formula or series expansion is used to express the value of some dependent variable u at node $n, j+1$ $\left(u_{j+1}^{n}\right)$ in terms of its adjacent node n, j $\left(u_{j}^{n}\right)$ and its spatial derivatives, where $t_n = n\Delta t$ and $x_j = j\Delta x$. Thus,

$$u_{j+1}^{n} = u_j^n + \left(\frac{\partial u}{\partial x}\right)_j^n \Delta x + \frac{1}{2!}\left(\frac{\partial^2 x}{\partial x^2}\right)_j^n \Delta x^2 + \ldots + \frac{1}{k!}\left(\frac{\partial^k u}{\partial x^k}\right)_j^n \Delta x^k + \frac{1}{(k+1)!}\left(\frac{\partial^{k+1} u}{\partial x^{k+1}}\right)_{j+\delta}^n \Delta x^{k+1} \tag{2-63}$$

The last term or remainder involves the evaluation of $\left(\partial^{k+1}u/\partial x^{k+1}\right)$ at $x = (j+\delta)\Delta x$ and $t = n\Delta t$. If only terms up to $(\partial^2 u/\partial x^2)$ are retained and one solves for $(\partial u/\partial x)$, the results is

$$\left(\frac{\partial u}{\partial x}\right) = \frac{u_{j+1}^n - u_j^n}{\Delta x} - \frac{1}{2}\left(\frac{\partial^2 u}{\partial x^2}\right)_{j+\delta}^n \Delta x, \qquad \text{for } 0<\delta<1 \tag{2-64}$$

The first term on the right hand side of Eq. (2-64) is called the first forward finite difference approximation. The second term is referred to as the local discretization (or local truncation) error.

Backward difference operators are determined in much the same way, expanding u_{j-1}^n about

x_j, t_n using a Taylor series, i.e.

$$u_{j-1}^n = u_j^n - \left(\frac{\partial u}{\partial x}\right)_j^n \Delta x + \frac{1}{2!}\left(\frac{\partial^2 x}{\partial x^2}\right)_j^n \Delta x^2 + \ldots + \frac{(-1)^k}{k!}\left(\frac{\partial^k u}{\partial x^k}\right)_j^n \Delta x^k + \frac{(-1)^{k+1}}{(k+1)!}\left(\frac{\partial^{k+1} u}{\partial x^{k+1}}\right)_{j+\delta}^n \Delta x^{k+1} \tag{2-65}$$

Following the same procedure used to arrive at the first forward difference operator, the results is

$$\left(\frac{\partial u}{\partial x}\right) = \frac{u_j^n - u_{j-1}^n}{\Delta x} + \frac{1}{2}\left(\frac{\partial^2 u}{\partial x^2}\right)_{j-\delta}^n \Delta x, \qquad \text{for } 0<\delta<1 \tag{2-66}$$

where the first term on the right hand side of Eq. (2-66) is now called the first backward finite difference approximation and the second term is still referred to as the local truncation error. An alternative to the directional forward and backward operators is the centered difference operator. For the first centered difference operator, all the terms in Eqs. (2-63) and (2-65) up to the $\left(\partial^3 u/\partial x^3\right)_j^n$ are subtracted from one another resulting in

$$\left(\frac{\partial u}{\partial x}\right) = \frac{u_{j+1}^n - u_{j-1}^n}{2\Delta x} - \frac{1}{6}\left(\frac{\partial^3 u}{\partial x^3}\right)_{j+\delta}^n \Delta x^2, \qquad \text{for } -1<\delta<1 \tag{2-67}$$

where the first term on the right hand side of Eq. (2-67) is referred to as the first centered finite difference approximation and the second term is referred to as the local truncation error.

Eqs. (2-64), (2-66) and (2-67) give three first difference operators to choose from. The local truncation error of the first centered difference operator is $O\left(\Delta x^2\right)$ compared to $O\left(\Delta x\right)$ for the forward and backward difference operators. For this reason the centered difference operator is the choice of the finite difference scheme used to numerically solve equations such as those developed for this dissertation.

Just as easily, higher order spatial derivatives can be found. By adding all the terms up to $\left(\partial^4 u/\partial x^4\right)_j^n$ in Eqs.(2-63) and (2-65), the second centered finite difference approximation can be determined. It is expressed as

$$\left(\frac{\partial^2 u}{\partial x^2}\right) = \frac{u_{j-1}^n - 2u_j^n + u_{j+1}^n}{\Delta x} - \frac{1}{12}\left(\frac{\partial^4 u}{\partial x^4}\right)_{j+\delta}^n \Delta x^2, \qquad \text{for } -1<\delta<1 \tag{2-68}$$

As with the first centered difference operator, its truncation error is of the order $O\left(\Delta x^2\right)$.

Using a Taylor expansion, it is also possible to approximate time derivative. In Eqs.(2-63) and (2-64) first order spatial derivatives were approximated. Just as easily, the first forward difference operator approximating $\left(\partial u/\partial t\right)$ could have been found if the Taylor expansion had been used to find u_j^{n+1} in terms of u_j^n time derivatives instead of spatial derivatives. The resulting first forward difference approximation for $\left(\partial u/\partial t\right)$ is

$$\left(\frac{\partial u}{\partial t}\right) = \frac{u_j^{n+1} - u_j^n}{\Delta t} - \frac{1}{2}\left(\frac{\partial^2 u}{\partial t^2}\right)_j^{n+\delta} \Delta t, \qquad \text{for } 0<\delta<1 \tag{2-69}$$

Using these finite difference operators, all the first and second order derivatives within the species equations are approximated.

2.4.2. Implicit scheme versus explicit scheme

The determining factor for whether a finite difference scheme is implicit or explicit is the time step at which spatial derivatives are approximated. In fully implicit schemes, spatial derivatives are approximated at the time step being solved for $\left(t=(n+1)\Delta t\right)$. In fully explicit schemes, spatial derivatives are approximated at the pervious time step $\left(t=n\Delta t\right)$. To illustrate the difference between fully implicit and explicit schemes, Eq.(2-70)

$$\frac{\partial u}{\partial t} = \alpha \frac{\partial^2 u}{\partial x^2} \tag{2-70}$$

will be approximated with both an implicit and explicit scheme. It is important to note that in this equation, α is constant and can be factored out of each u term.

An explicit backward temporal and second centered spatial scheme is shown in Eq. (2-71), i.e.

$$\frac{u_j^{n+1}-u_j^n}{\Delta t}=\alpha\frac{u_{j-1}^n-2u_j^n+u_{j+1}^n}{\Delta x^2}\rightarrow$$
$$u_j^{n+1}=u_j^n+\alpha\frac{\Delta t}{\Delta x^2}\left(u_{j-1}^n-2u_j^n+u_{j+1}^n\right) \tag{2-71}$$

This scheme is termed explicit because the expression for u_j^{n+1} is explicit, containing only known values from the previous time step n. For an explicit scheme all spatial derivatives are approximated at time equals $n\Delta t$.

An implicit backward temporal and second centered spatial scheme is shown in Eq. (2-72), i.e.

$$\frac{u_j^{n+1}-u_j^n}{\Delta t}=\alpha\frac{u_{j-1}^{n+1}-2u_j^{n+1}+u_{j+1}^{n+1}}{\Delta x^2}\rightarrow$$
$$-\frac{\alpha\Delta t}{\Delta x^2}u_{j-1}^{n+1}+\left(1+2\frac{\alpha\Delta t}{\Delta x^2}\right)u_j^{n+1}-\frac{\alpha\Delta t}{\Delta x^2}u_{j+1}^{n+1}=u_j^n \tag{2-72}$$

This scheme is termed implicit because u_j^{n+1} must be solved for simultaneously with all other u^{n+1} values using a matrix formulation. For an implicit scheme, all spatial derivatives are approximated at time equals $(n+1)\Delta t$. Figure 2-4 demonstrates the formulation and solution technique used to solve for $u_{0\rightarrow J}^{n+1}$. The result of this scheme is a tridiagonal $(j-1$ by $j-1)$ matrix labeled $\overline{\overline{A}}$, a solution vector $\vec{B}$ and load vector $\vec{C}$. It is important to note, the solution method illustrated in Figure 2-4 is for Dirichlet boundary conditions. The terms multiplied by s and then added to u_1^n and u_{J-1}^n, respectively, in load vector $\vec{C}$ represent the contributions of boundary conditions for the time step $(n+1)$ being solved for.

Implicit and explicit schemes represent the two extremes used for one-level finite difference schemes. One-level schemes use only nodal solutions from time step t_n to obtain a solution at time step t_{n+1}. Multi-level schemes were not considered in this dissertation. They are more difficult to start but can offer increased accuracy. To represent all the possible one-level schemes, a variable θ is introduced. θ is referred to as a weighting derivatives are located. Using the theta method, spatial derivatives are approximated at $t=(n+\theta)\Delta t$. Eq.(2-73) demonstrates how this weighted method can be used to approximate Eq.(2-63) :

$$\frac{u_j^{n+1}-u_j^n}{\Delta t}=\theta\alpha\frac{u_{j-1}^{n+1}-2u_j^{n+1}+u_{j+1}^{n+1}}{\Delta x^2}+(1-\theta)\alpha\frac{u_{j-1}^{n}-2u_j^{n}+u_{j+1}^{n}}{\Delta x^2} \quad \text{for} \quad 0\le\theta\le 1 \tag{2-73}$$

if $\theta=0$, Eq.(2-73) is an explicit scheme

if $\theta=1$, Eq.(2-73) is a fully implicitly scheme

if $\theta=1/2$, Eq.(2-73) is an implicit scheme called the Crank-Nicolson method.

The scheme depicted in Eq.(2-73) can be rewritten in the following more common form, grouping nodes at similar time steps and using $s=\alpha\Delta t/\Delta x^2$:

$$\begin{aligned}&-\theta s u_{j-1}^{n+1}+(1+2\theta s)u_{j-1}^{n+1}-\theta s u_{j+1}^{n+1}=\\&(1-\theta)s u_{j-1}^{n}+(1-2(1-\theta)s)u_j^n+(1-\theta)s u_{j+1}^{n}\end{aligned} \tag{2-74}$$

The finite difference scheme used to solve for concentration and voltage in the domain is a weighted or theta scheme. This allows it to be changed from fully implicit to fully explicit or any fraction of either depending on the value of theta. When generating results for this dissertation theta was set to unity resulting in a fully implicit scheme.

The numerical solution techniques used in this dissertation are from the finite-difference method. A central-difference representation of the space derivative and an implicit forward-difference representation of the time derivative are adopted. For the boundary condition, 2nd order backward difference and 2nd order forward difference are applied for right boundary condition and left boundary condition respectively.

The solution procedure is showed in the Figure 2-3. The convergence criteria for iteration and steady state are

$$\left|\frac{V_i^{new}-V_i^{old}}{V_i^{old}}\right|\le 1\times10^{-4} \tag{2-75}$$

V_i is a arbitrary variable.

The parameters used in this dissertation are listed in Table 2-2. Figure 2-4 shows the spatial grid analyzing, and the 949 spatial points is used for this dissertation. Figure 2-5 shows the time step analyzing, and the time step of 0.001 seconds is used for this dissertation.

2.5. Results and discussion

Figure 2-6 shows the polarization curves in the steady state, and the solid line, dot line and dash line are present result, Lin et al.'s model and Natarajan and Nguyen's model respectively. The catalyst layer is treated as an interface as in Natarajan and Nguyen's model. It can be clearly seen form Figure 2-6 that these three curves overlap when the current density is below 0.5 $A \cdot cm^{-2}$, then the curve in last case separates from others afterward. This observation can be explained as follows. When the cell is operated at low current density, the oxygen transport rate is much faster than the kinetic rate of oxygen reduction, and therefore oxygen can access all the active areas equally. Liquid water is going to be accumulated, but it will not affect the oxygen transport. The cell performance is under the control of activation loss and ohmic loss, which are the same for these three cases at low current density. When the current density reaches 0.5 $A \cdot cm^{-2}$, there is a significant amount of liquid water accumulating. The present result is from transient to steady state.

Figure 2-7 shows the evolution profiles of saturation level with V_s =0.2V, 0.4V and 0.6 V respectively. The liquid water saturation level increases with time till steady state is reached. The amount of the generated liquid water will begin to affect the system after 1 sec and the generated liquid water in the catalyst layer start to occupy the pores. First, the water is generated at catalyst layer, and then diffuses to the gas diffusion layer. The liquid water saturation level in the catalyst layer is higher than the level in the gas diffusion layer. The water transport in the catalyst layer includes gas-phase diffusion, evaporation and capillary action. Driving force of the liquid water is capillary action. The liquid water is transported from CL to GDL by capillary force. In the cases of high cell voltage, say V_s = 0.6V, the electrochemical reaction is not strong and less liquid water is generated. Thus liquid water saturation level is less than the level when lower cell voltage is applied. The lower cell voltage is applied, the more liquid water is generated. The pores are occupied by the liquid water. The oxygen can not be transported to the catalyst surface, thus the cell performance will down. Then the mass transport limit occurs. The transport of liquid water is slow, and it reaches the steady state in the order of 10 sec.

The distribution of saturation level in the steady state with various cell voltages is shown in Figure 2-8. The liquid water saturation level in the catalyst layer is much higher than the level in the gas diffusion layer. The difference of saturation level between CL and GDL are 30%, 34% and 53% when V_s =0.2V, 0.4V and 0.6V respectively. There are two reasons: (1) the CL porosity is much smaller than GDL porosity; (2) the permeability of liquid water in the CL is much smaller than that in the GDL.

Figure 2-9 demonstrates the evolution profiles of ionic potential with V_s=0.2V, 0.4V and 0.6V respectively. When the cell voltage is higher, both oxygen reduction reaction and the loss of ionic potential will be lower. When the cell voltage is lower (i.e., the current density increases), oxygen reduction reaction and the loss of ionic potential will be larger. It can be clearly seen from Fig. 2-9 that the ionic potential will not decrease monotonically with time. It reaches a critical value then increases with time until the steady state is obtained. Thus the difference between the critical value and the steady state of any given ionic potential is dependent on the cell voltage applied. When the cell voltage is 0.2V, the difference is about 20%. The ionic potential reaches 80% of its critical value in 0.005sec and reaches the critical value in the order of 10^{-1} sec.

The distribution of ionic potential in the steady state with various cell voltages is shown in Figure 2-10. In the membrane, the shape of the ionic potential distribution is a straight line. This is due to that there is not any gas to be consumed. In the catalyst layer, the ionic potential distribution is nonlinear because oxygen and protons have been consumed by the reduction reaction. The protons move much faster than the liquid water. The lower the cell voltage is applied, the larger the ionic potential loss will be.

Figure 2-11 presents the evolution profiles of oxygen concentration with V_s=0.2V, 0.4V and 0.6V respectively. At the initial state, it assumes that there is no oxygen in the cell. After start up, the oxygen transport from the gas channel to the catalyst layer via gas diffusion layer. In the gas diffusion layer, the oxygen diffuses continuously to the catalyst layer along the pores. In the meantime, the oxygen dissolves into the Nafion film and reaches the pellet surface. Then liquid water is generated. At the inlet, the distribution of oxygen concentration is constant. Within 5sec, it changes dramatically at the very beginning and then decreases with time in the catalyst layer. After 5sec, when V_s=0.2V and 0.6V, it remains. But when V_s=0.4V, the turning point is 10sec. After 5sec and when V_s=0.2V, the oxygen transport is affected by liquid water. When V_s=0.4V, the liquid water is less than when V_s=0.2V, thus it needs more time to reach the steady state. When V_s=0.6V, because the electrochemical reaction reacts moderately, it consumes less oxygen. And it generates less liquid water than others, thus it reaches the steady state quickly.

The distribution of oxygen concentration in the steady state with various cell voltages is shown in Figure 2-12. The transportation of oxygen is diffusion only in the GDL, thus the distribution of the oxygen concentration is linear. The electrochemical reaction occurs in the catalyst layer, thus the oxygen distribution is nonlinear. The lower the cell voltage is applied, the more the oxygen is

consumed.

Figure 2-13 plots the evolution profiles of vapor water concentration with V_s=0.2V, 0.4V and 0.6V respectively. In the initial state, it is assumed that the concentration is zero in the cell. Then start up, the air begins flowing into the cell. Vapor water comes from air and evaporation of liquid water. The concentration of vapor water increases with time. At the inlet, the distribution of vapor water concentration remains. Within 5sec, it changes dramatically at the very beginning and then increases with time in the catalyst layer. After 5sec and when V_s=0.2V, it remains. When V_s=0.4 and V_s=0.6V, the turning point is 10sec. But when V_s=0.6V, the values of the concentration are smaller than others.

The distribution of vapor water concentration in the steady state with various cell voltages is shown in Figure 2-14. The vapor water concentration in CL is higher than in GDL, because the liquid water saturation level in CL is higher than in GDL too. The liquid water is evaporated to vapor. It is obvious seen that is nonlinear in CL when V_s=0.6V. When lower cell voltage is applied, the vapor water is saturated, thus the profiles are similar in CL when V_s=0.2V and 0.4V.

2.5.1. Effect of operating temperature

Figure 2-15 depicts the time evolution of polarization curves with various operating temperatures. In the cases of lower cell voltage, the current density overshoots as time evolving. This is due to the lower ohmic resistance that fully hydrated membrane exhibits and the lower humidity of gas in the catalyst layer. This phenomenon corresponds to the loss of ionic potential. On the other hand, the chemical reaction is moderately when higher cell voltage is applied, then the overshoot is subtle. The higher the operating temperature is, the smaller the overshot will be. The overshot are 13%, 11% and 7% when the operating temperature is 60^oC, 70^oC and 80^oC respectively. The activity of catalyst is better when the operating temperature is high. Thus the activation over-voltage becomes smaller, and then the overshot is smaller.

Table 2-1. Correlation used in Chapter 2.

Water content in membrane		
	$\lambda = \frac{C_w^N}{C_f}$	
Diffusivity of liquid water in Nafion membrane		
	$C_{w(\lambda>4)}^N = 10^{-6} \exp\left[2416\left(\frac{1}{303}-\frac{1}{T}\right)\right]\left(2.563-0.33\lambda+0.0246\lambda^2-0.000671\lambda^3\right)$	
	$C_{w(3>\lambda\geq4)}^N = 10^{-6} \exp\left[2416\left(\frac{1}{303}-\frac{1}{T}\right)\right]\left(6.89-1.33\lambda\right)$	
	$C_{w(2>\lambda\geq3)}^N = 10^{-6} \exp\left[2416\left(\frac{1}{303}-\frac{1}{T}\right)\right]\left(-3.1+2.0\lambda\right)$	
Conductivity of Nafion membrane		
	$\kappa_N = \exp\left[1268\left(\frac{1}{303}-\frac{1}{T}\right)\right]\left(0.005139\lambda-0.00326\right)$	
Net electro-osmotic drag coefficient		
	$n_d = \frac{2.5}{22\lambda}$	
Diffusivity in gas stream		
	$D_{O_2}^N = 0.0031\exp\left(-\frac{2768}{T}\right)$	
	$D_{O_2}^W = 2.41\times10^{-5}\left(\frac{\mu_{T_r}}{\mu_T}\right)^{1.026}\left(\frac{T}{T_r}\right)$	
	$D_{O_2}^g = 0.1775\left(\frac{T}{273.15}\right)^{1.823}$	
	$D_v^g = 0.256\left(\frac{T}{307.15_r}\right)^{2.334}$	
Henry's constant		
	$H_{O_2}^N = 1.33\times10^6 \exp\left(-\frac{666}{T}\right)$	
	$H_{O_2}^W = 5.08\times10^6 \exp\left(-\frac{498}{T}\right)$	

Table 2-2. Parameters used in simulation.

Gas diffusion layer properties			
	Porosity	0.3	
	Thickness	0.025	cm
	Permeability	10^{-9}	cm^2
	$\left(-dp_c/ds\right)$	284.2	Dyne cm^{-2}
Catalyst layer properties			
	Porosity	0.06	
	Thickness	0.0016	cm
	Permeability	3×10^{-11}	cm^2
	$\left(-dp_c/ds\right)$	568.4	Dyne cm^{-2}
	Catalyst loading (m_{Pt})	0.4	
	Specific surface area of Pt (a_{Pt})	1000	cm^2(mg Pt)$^{-1}$
	Volumetric fraction of Naion in catalyst pellet ($\varepsilon^P{}_N$)	0.393	
	Raduis of catalyst pellet, (R_{agg})	10^{-5}	cm
	Thickness of Nafion	10^{-6}	Cm
	Exchange current density, ($i_{0,ref}$ 0°C)	10^{-6}	Acm^{-2}
Membrane properties			
	Thickness	0.005	cm
	Porosity	0.35	
	Fixed charge site concentration	1.2×10^{-3}	mol cm^{-3}
Operation conditions			
	Temperature	60	^oC
	Pressure	1	atm
	Mole fraction of oxygen in the air let	0.206	
	Humidity in air inlet		
	Humidity at anode		

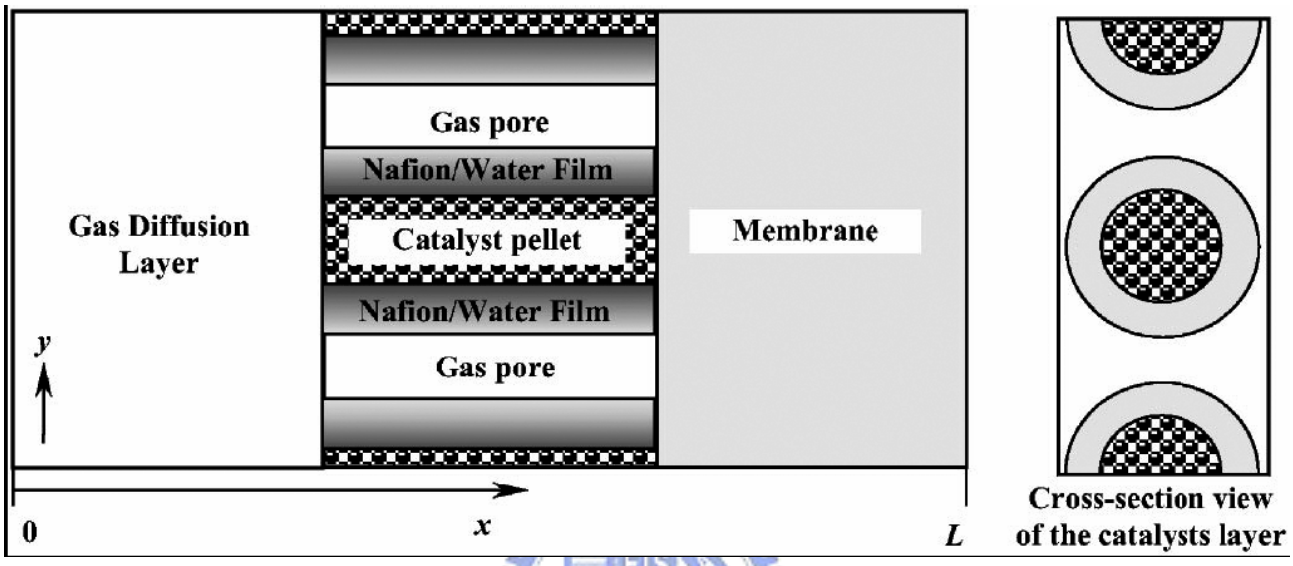

Fig 2-1. Schematic of the model domain[91]

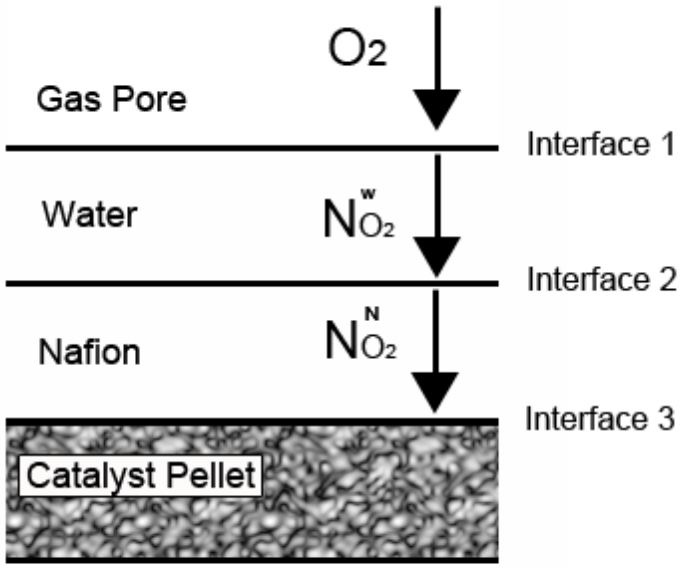

Fig 2-2. The scheme of catalyst pellet domain

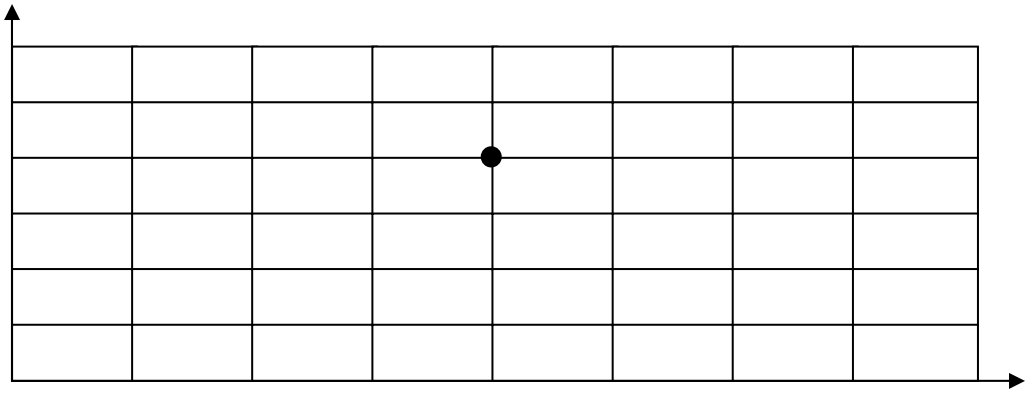

Fig 2-3. Grid spacing

$$\frac{u_j^{n+1}-u_j^n}{\Delta t}-\alpha\frac{u_{j-1}^{n+1}-2u_j^{n+1}+u_{j+1}^{n+1}}{\Delta x^2}=0$$

$$\downarrow$$

$$-su_{j-1}^{n+1}+(1+2s)u_{j-1}^{n+1}-su_{j+1}^{n+1}=u_j^n \qquad \text{with } s=\alpha\frac{\Delta t}{\Delta x^2}$$

$$\downarrow$$

$$\begin{bmatrix} 1+2s & -s & 0 & 0 & 0 & \cdots & 0 \\ -s & 1+2s & -s & 0 & 0 & \cdots & 0 \\ 0 & -s & 1+2s & -s & 0 & \cdots & 0 \\ 0 & 0 & \ddots & \ddots & \ddots & \cdots & \vdots \\ 0 & 0 & 0 & -s & 1+2s & -s & 0 \\ \vdots & 0 & 0 & 0 & -s & 1+2s & -s \\ 0 & 0 & 0 & 0 & 0 & -s & 1+2s \end{bmatrix} \begin{Bmatrix} u_1^{n+1} \\ u_2^{n+1} \\ u_3^{n+1} \\ u_4^{n+1} \\ \vdots \\ u_{J-2}^{n+1} \\ u_{J-1}^{n+1} \end{Bmatrix} = \begin{bmatrix} u_1^n+su_0^{n+1} \\ u_2^n \\ u_3^n \\ u_4^n \\ \vdots \\ u_{J-2}^n \\ u_{J-1}^n+su_J^{n+1} \end{bmatrix}$$

$$\overline{\overline{A}} \qquad \overline{B} \qquad \overline{C}$$

Fig 2-4. Implicit formulation and solution technique

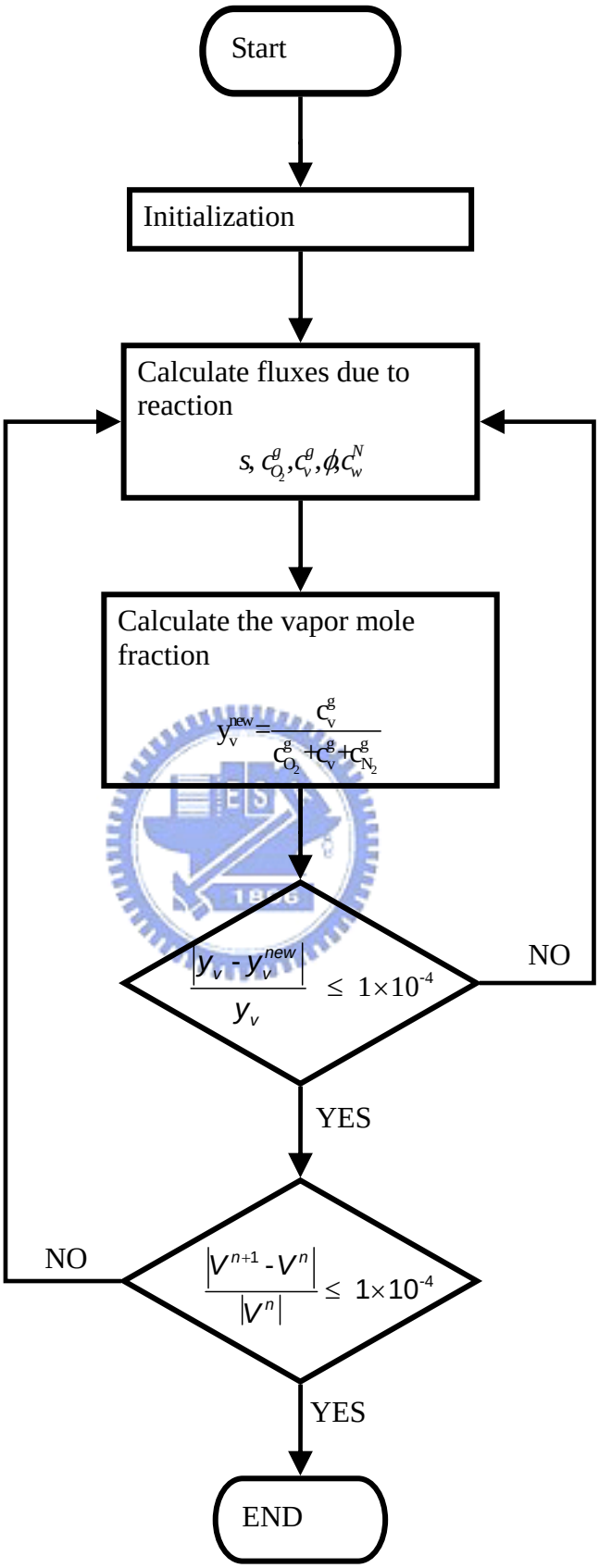

Fig 2-5. Flow chart.

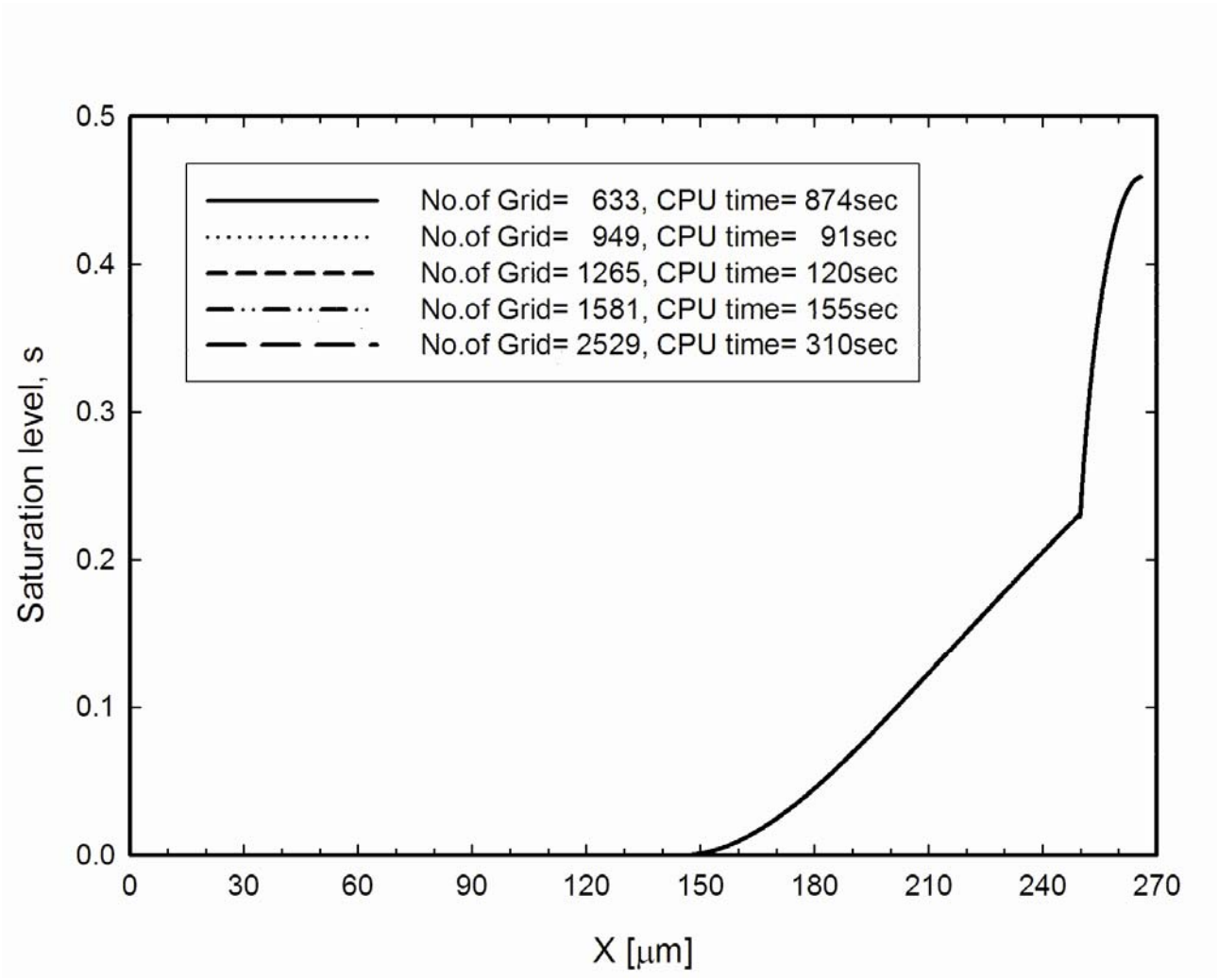

Fig 2-6. Spatial grid analysis.

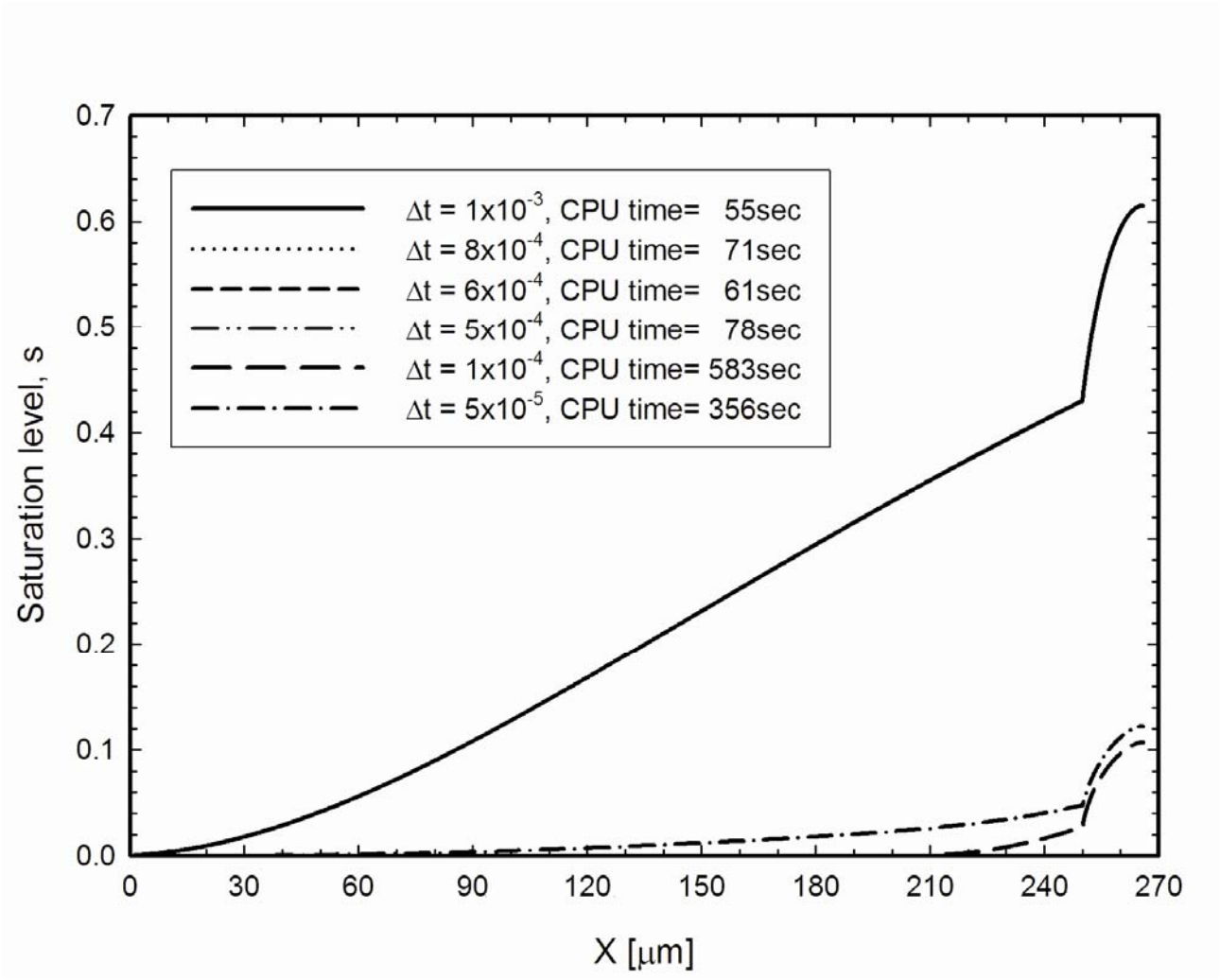

Fig 2-7. Time step analysis.

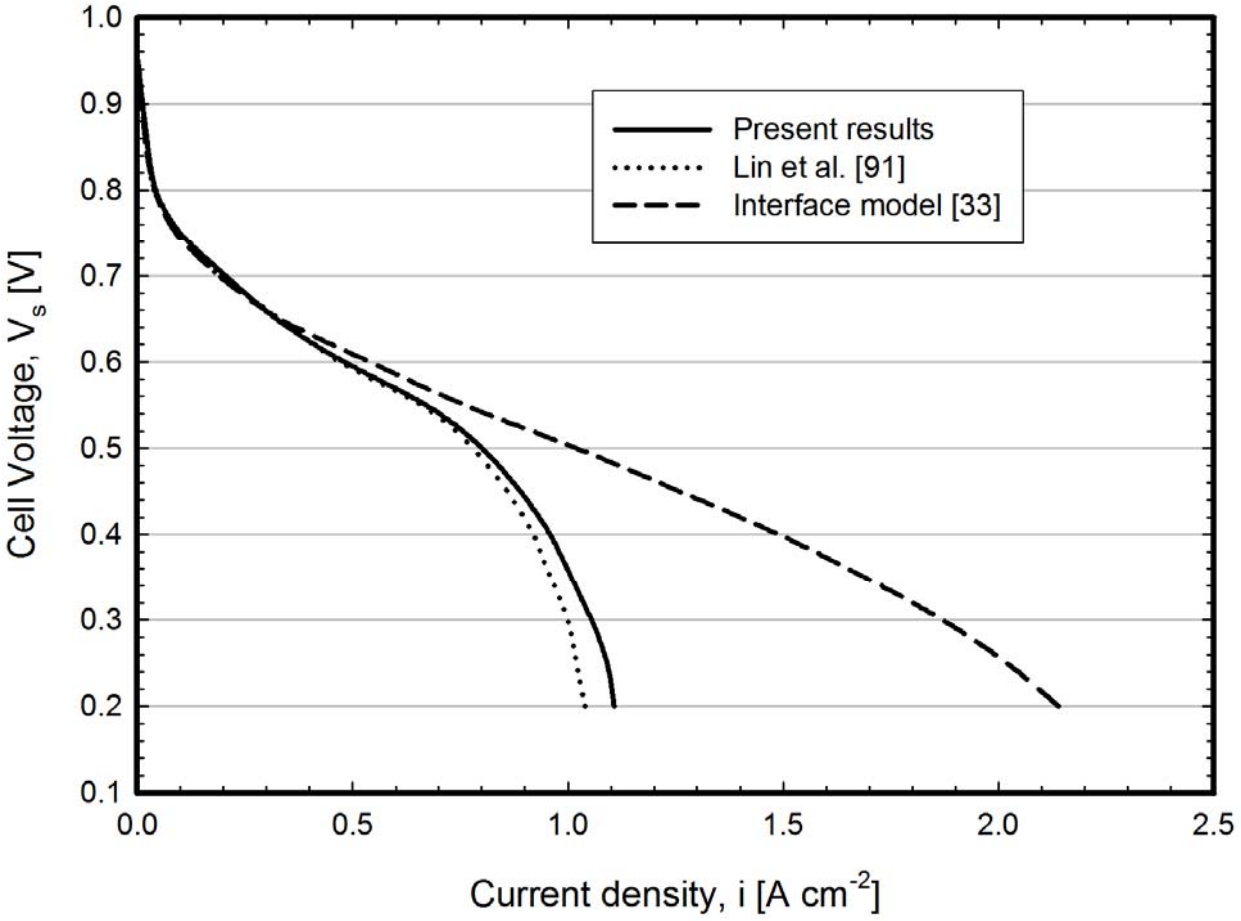

Fig 2-8. Performance comparison with different models.

(a)

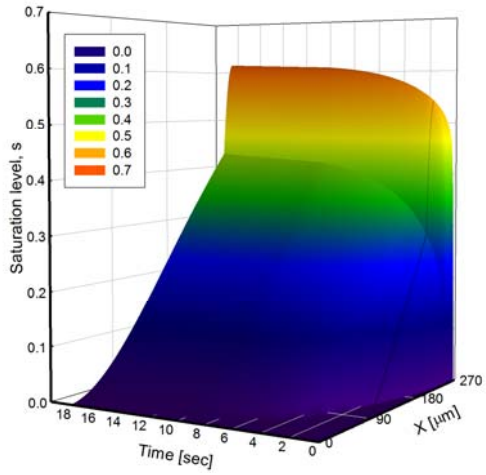

(b)

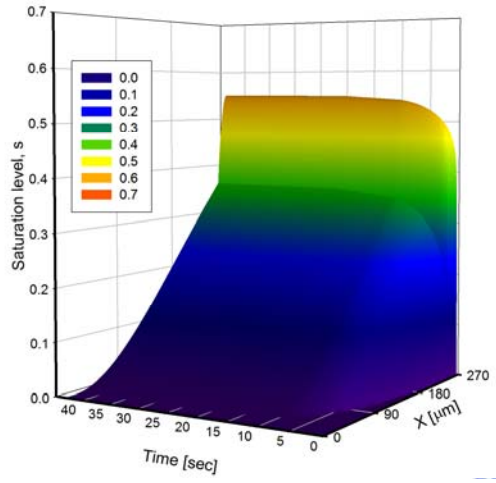

(c)

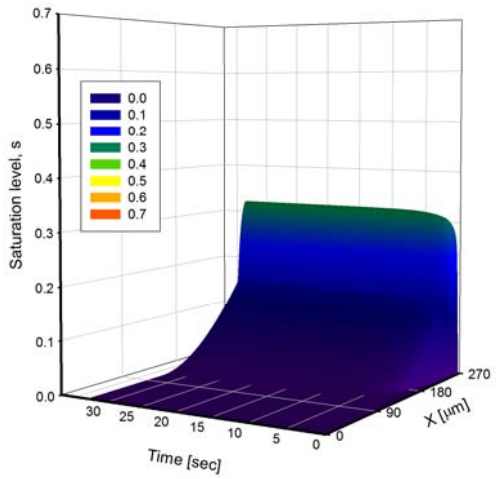

Fig 2-9. The evolution profile of saturation level (base case) (a) V_s =0.2V, (b) V_s =0.4V, (c) V_s =0.6V

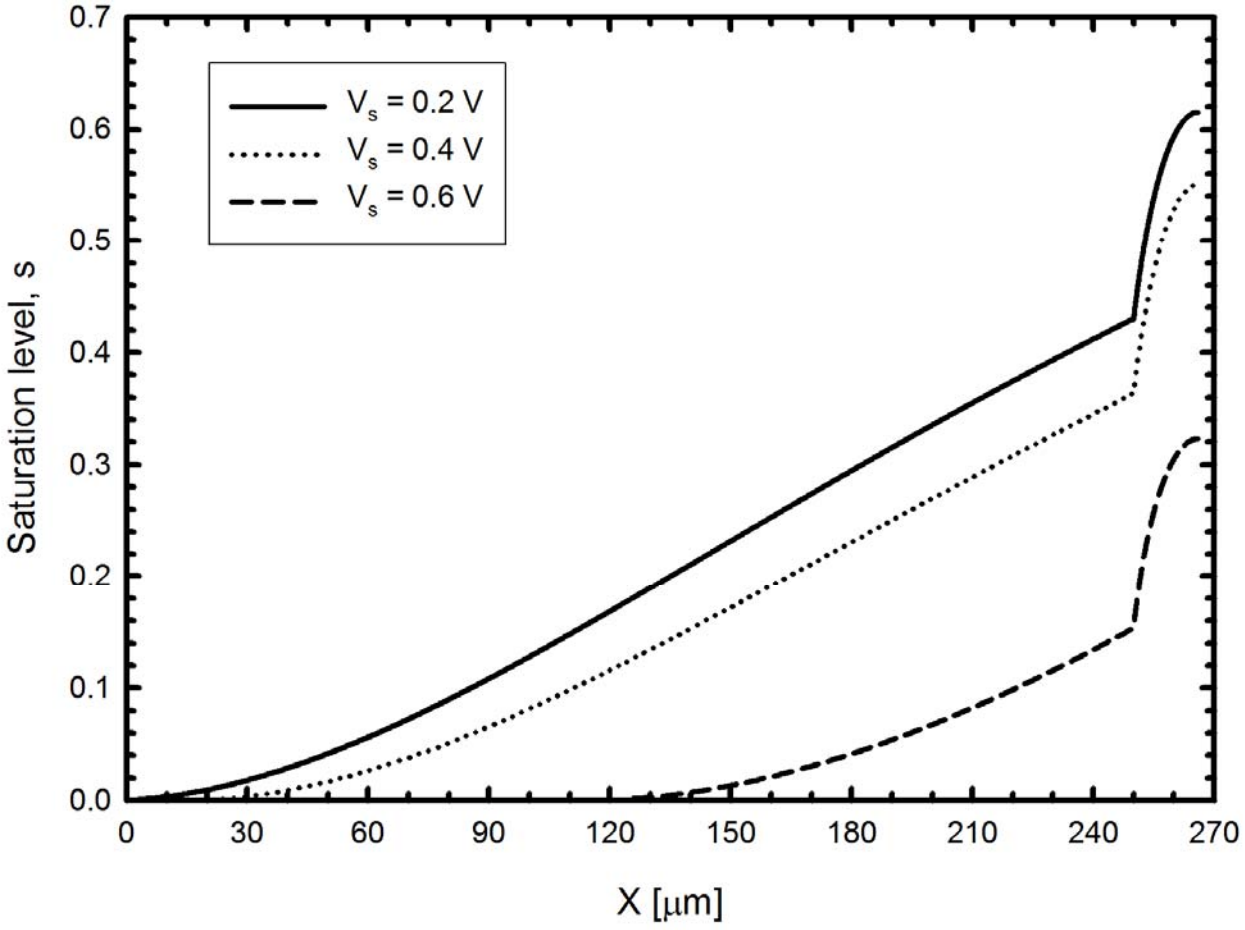

Fig 2-10. The distribution of saturation level with various cell voltages in the steady state.

(a)

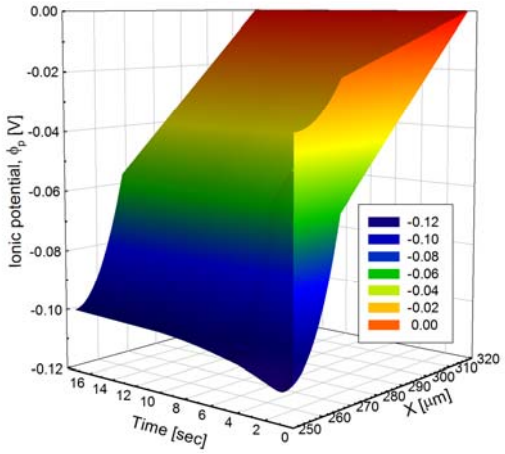

(b)

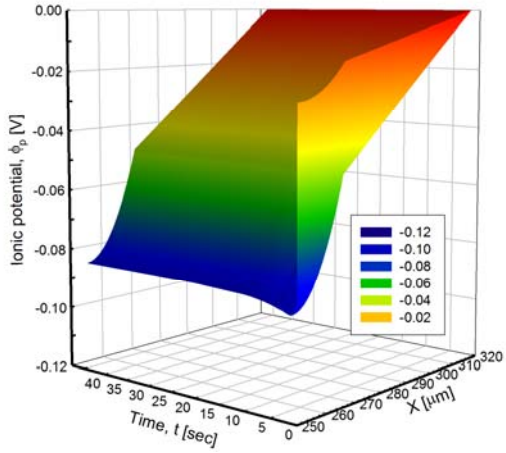

(c)

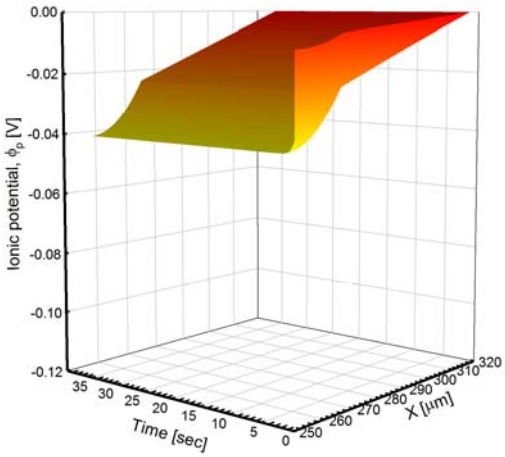

Fig 2-11. The evolution profiles of ionic potential ε_{CL} =0.1 (a) V_s =0.2V, (b) V_s =0.4V, (c) V_s =0.6V

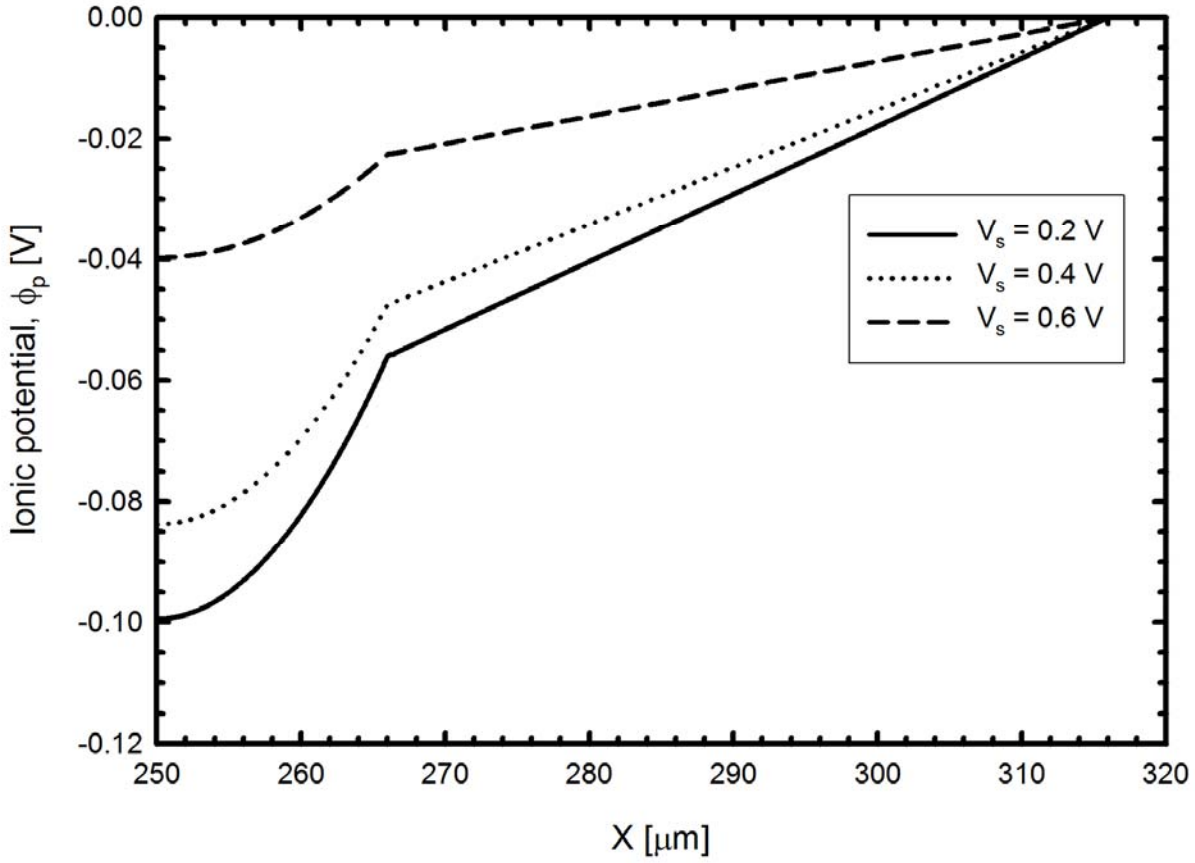

Fig 2-12. The distribution of ionic potential with various cell voltages in the steady state. (a) V_s =0.2V, (b) V_s =0.4V, (c) V_s =0.6V

(a)

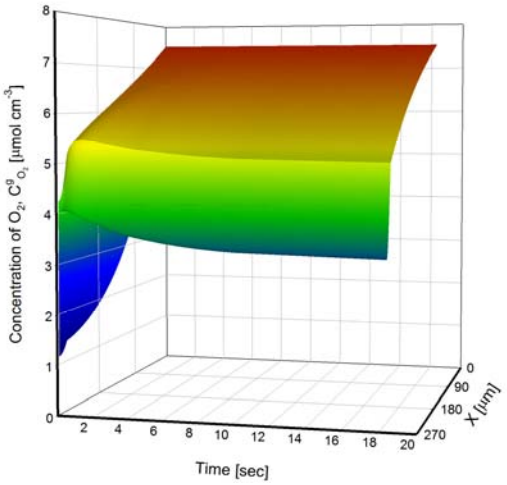

(b)

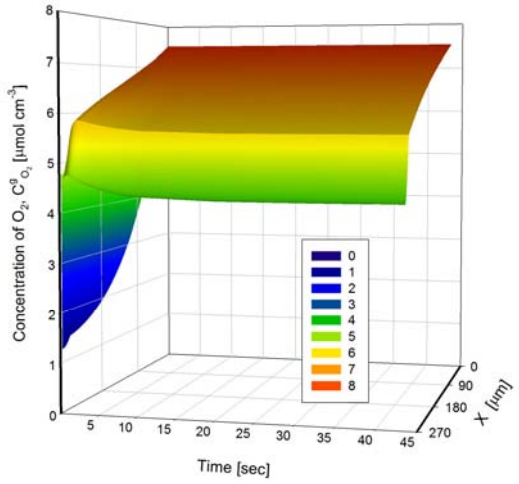

(c)

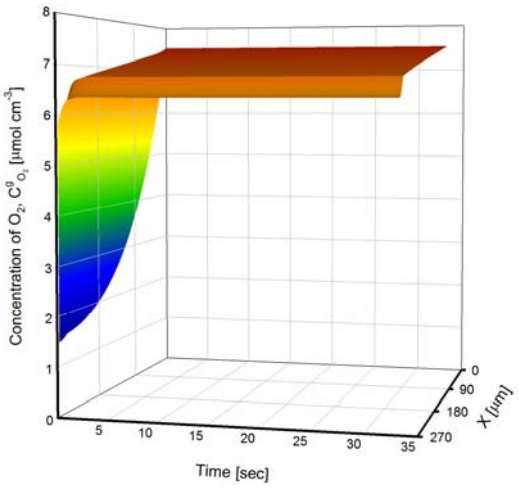

Fig 2-13. The evolution profiles of oxygen concentration (a) V_s =0.2V, (b) V_s =0.4V, (c) V_s =0.6V

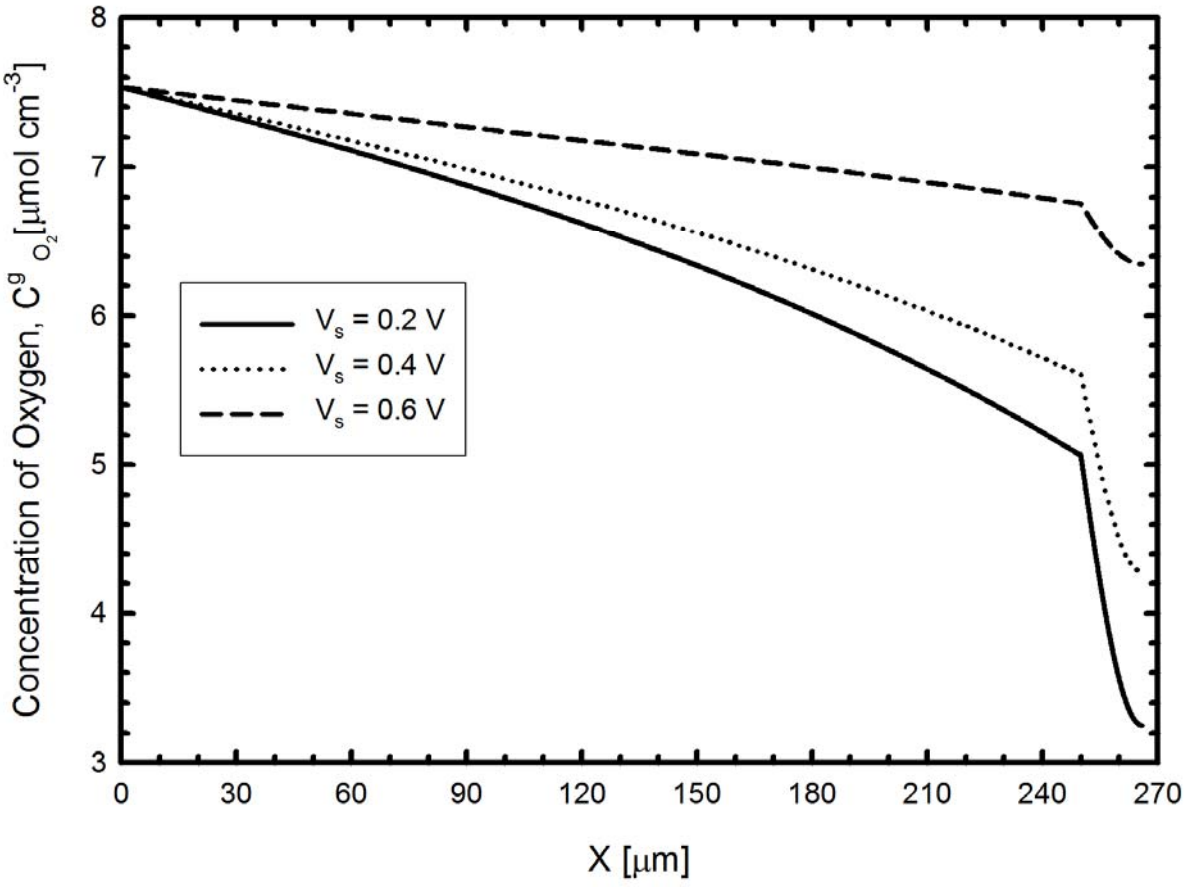

Fig 2-14. The distribution of oxygen concentration with various cell voltages in the steady state.

(a)

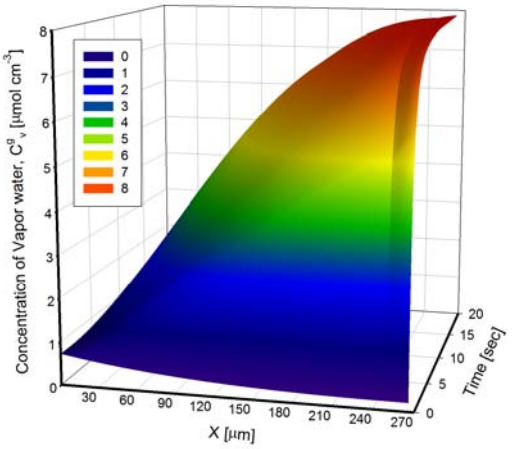

(b)

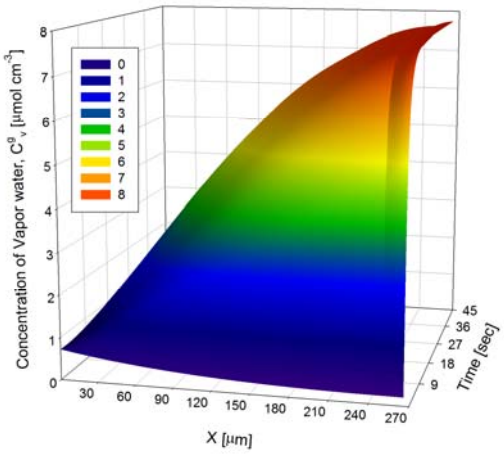

(c)

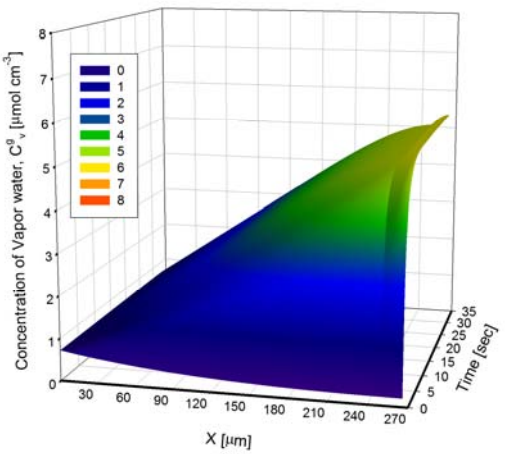

Fig 2-15. The evolution of vapor water concentration (a) V_s =0.2V, (b) V_s =0.4V, (c) V_s =0.6V

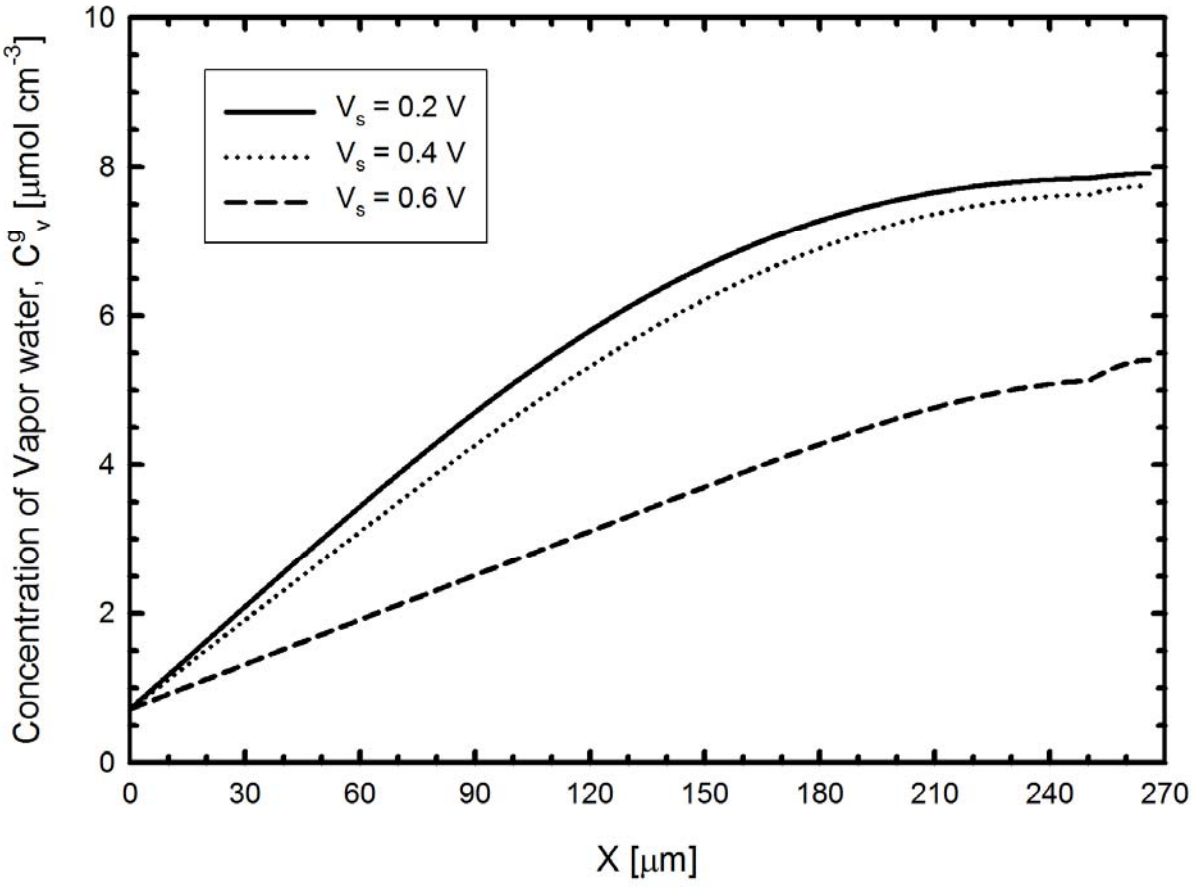

Fig 2-16. The distribution of vapor water concentration with various cell voltages in the steady state.

(a)

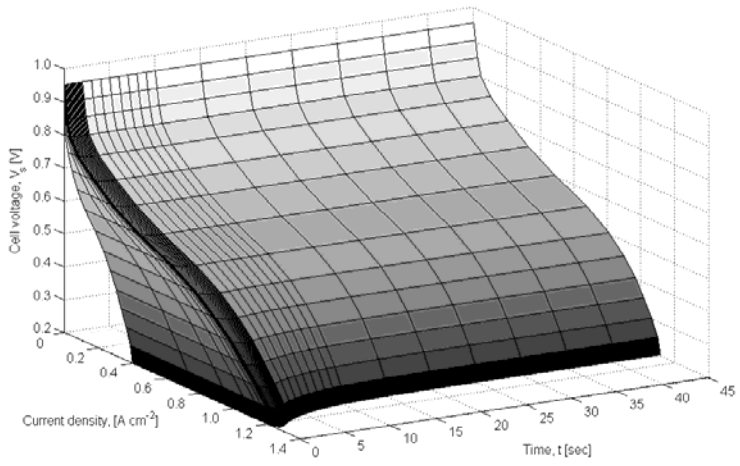

(b)

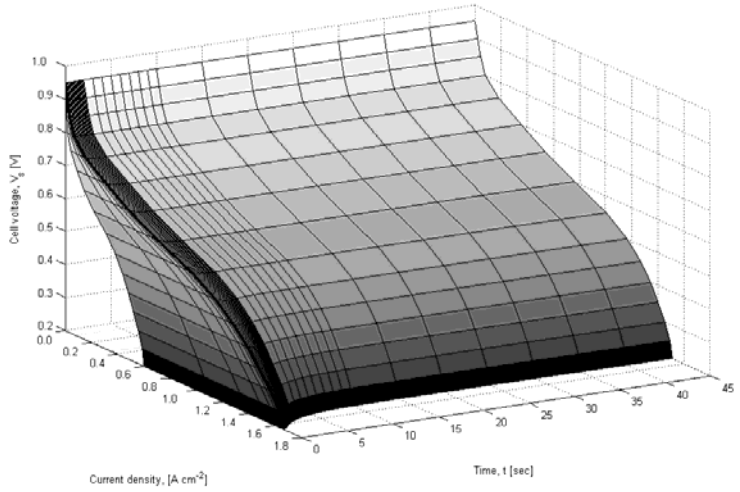

(c)

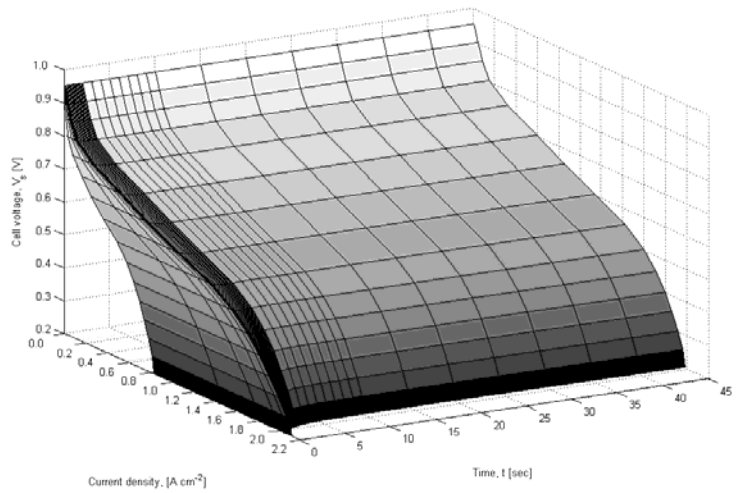

Fig 2-17. The evolution profiles of polarization curves. (a) $60^{o}C$, (b) $70^{o}C$, (c) $80^{o}C$

3. Parametric study for the cylindrical thin film-agglomerate model

In the preceding chapter, the model depicting the transient evolutions of various properties as well as performance of a PEMFC is developed and preliminary results from on the base case are present. In order to obtain a global and insightful aspect of the cell behaviors, this chapter is devoted to investigate the parameters which can affect the cell performance, such as the porosity gas diffusion layer, the porosity of catalyst layer, the thickness of catalyst layer and radius of agglomerate etc.

3.1. Effects of gas diffusion layer porosity

The evolutions of cell current density at cell voltages of 0.2V, 0.4V and 0.6V for various porosities of GDL are shown in Figure 3-1 which is a semi-logarithm plot and the horizontal axis indicates time domain. The plot indicates that, within 10^{-2} sec, current density increases rapidly. Between 10^{-2}sec and 10^{-1}sec, the current density remains constant and after 1sec, it changes by the effect of the generated water. The water generation is related to the GDL porosity and cell voltage. The higher the cell voltage is applied, the less the liquid water is generated. The larger GDL porosity will produce higher current density, but it has little effect on the cell current density. At lower cell voltage, the reduction of oxygen reacts dramatically, and generates more liquid water. The lower GDL porosity cannot drain effectively. In the meantime, the cell current density downs. (Figure 3-1.a, b) After 1sec, if lower cell voltage is applied and ε_{GDL}=0.2, the cell current density goes down lower. When ε_{GDL}=0.2 and V_s=0.4V, current density decreases 6%. While V_s=0.2V, current density decreases 15%. The higher the GDL porosity is, the more liquid water will be drained. But the more liquid water has few effects on the oxygen transport. So, when ε_{GDL} = 0.5, the current density won't go down after 1 sec.

In the steady state, the effect of GDL porosity and cell current density is shown in Figure 3-2. Under the same cell voltage, the more the porosity of gas diffusion layer is, the higher the cell current density will be. The most performance difference occurs at V_s=0.2V. The current density difference between ε_{GDL}=0.2 and ε_{GDL}=0.5 is over 40%. The larger the catalyst layer porosity is, the more liquid water will be drained. When V_s=0.2V, more liquid water is generated. Lower porosity of GDL can not drain rapidly and the liquid water resists the transportation of oxygen. But

the higher the cell voltage is applied, the fewer the liquid water is generated. Therefore the difference between ε_{GDL}=0.2 and ε_{GDL}=0.5 is subtle.

3.2. Effects of catalyst layer porosity

Under different porosity of CL, the cell current density curves are shown in Figure 3-3 and cell voltage are 0.2V, 0.4V and 0.6V respectively. Within 10^{-2}sec, the cell current density rises rapidly. Between 10^{-2}sec and 10^{-1}sec, there is a plateau. After 1sec, the current density relates with the cell voltage and the porosity of catalyst layer. When V_s=0.6V, it is obvious that the smaller the porosity CL is, the higher the current density will be. After 1sec, the current density will rise again. When V_s=0.4V and ε_{CL}=0.04, the value of the maximum of current density is different from V_s=0.6. At the first plateau, there is a maximum of current density when ε_{CL}=0.06. But at the steady state, when ε_{CL}=0.06, 0.08 and 0.10 the value of cell current density are identical. After 1sec and when ε_{CL}=0.04, the current density decreases with time about 10%. The others decrease within 5%.

After 1sec and when V_s=0.2V, the current density drops with time, except when ε_{CL}=0.3. When ε_{CL}=0.04, the current density drop down the most, ε_{CL}=0.06 the second. When ε_{CL}=0.04, the current density decreases 17%. While ε_{CL}=0.06 and ε_{CL}=0.08, it decreases about 10%. This is affected by the liquid water in the catalyst layer. The larger the catalyst layer porosity is, the more liquid water will be drained. The liquid water has almost no effect on the PEMFC. But the amount of platinum loading in the catalyst layer decreases at the same time. And the activity energy decreases as well. The cell performance goes down. The lower catalyst layer porosity can not drain effectively. The oxygen can not get to the catalyst surface and the cell performance drop.

For the porosity of catalyst layer, there is extreme value of current density when V_s=0.4 and so does V_s=0.2V. When V_s=0.4, the optimum appears between ε_{CL}=0.06 and ε_{CL}=0.08. But when V_s=0.2, the optimum appears between ε_{CL}=0.08 and ε_{CL}=0.1. Under lower cell voltage, lower catalyst layer porosity can not provide enough room to hold the large quantity of the generated liquid water. The accumulation of the liquid water resists the transportation of oxygen. This lowers the cell current density. Larger catalyst layer porosity drains more water but the catalyst loading is lower. Because the catalyst decreases, the cell current density decreases as well. Under higher cell voltage, the porosity of catalyst layer and current density are inversed. Lower catalyst layer porosity gets higher current density. Less liquid water does not affect the system much. The higher the platinum loading is, the higher the current density will be.

3.3. Effects of catalyst layer thickness

Figure 3-5 is a semi-logarithm plot and the horizontal axis indicates time. Under different thickness of CL, the cell current density curves are shown in Figure 3-5 and V_s=0.2V, 0.4V and 0.6V respectively. Within 10^{-2}sec, the cell current density rises rapidly. Between 10^{-2}sec and 10^{-1}sec, there is a plateau. When $\delta_{CL}=3\,\mu m$, the current density are always lower, because the catalyst layer is quite thin, the platinum loading is too low to facilitate the electrochemical reaction. When V_s=0.2V (Figure 3-5a), when $\delta_{CL}=10\,\mu m$, after 10^{-1}sec the curve rises slightly first and then goes down. When it reaches the steady state, the results are similar when $\delta_{CL}=10\,\mu m$ and $16\,\mu m$. After 1sec, the curves go down. The current density decreases 11.6%, 13.3%, 16.8% and 19% in the steady state when $\delta_{CL}=10\,\mu m$, $16\,\mu m$, $24\,\mu m$ and $30\,\mu m$ respectively. When V_s=0.4V (Figure 3-5b), after 1sec, it decreases very little. When V_s=0.6V, after 1sec, the curves rise slightly first and then remain. Figure 3-6 and Figure 3-7 are the distribution of oxygen concentration and saturation level respectively in the steady state with V_s=0.6V. When $\delta_{CL}=30\,\mu m$, the oxygen consumption is 12% of the inlet oxygen concentration inside the catalyst layer and the liquid water saturation level is 0.4. In the meantime, more pores are occupied by the accumulated liquid water. This limits the oxygen transport. The current density downs. For a thicker catalyst layer, there is even more accumulated liquid water. The current density decreases rapidly.

Figure 3-8 is the relationship between current density and catalyst layer thickness in the steady state with various cell voltages. The optimum values of catalyst layer thickness appears between $\delta_{CL}=10\,\mu m$ and $13\,\mu m$.

3.4. Effects of agglomerate radius

Figure 3-9 presents the current density curves under various agglomerate radii. In the Fig. 3-9a, 3-9b, 3-9c are V_s=0.2V, 0.4V and 0.6V respectively. Within 10^{-2}sec, the cell current density rises rapidly. Between 10^{-2}sec and 1sec, there is a plateau. After 1sec, the current density relates with the cell voltage and the agglomerate radius. When V_s=0.2V (Fig. 3-9a), the current density decreases 16.6%, 14.9% and 11.7% when R_{agg}=5nm, 50nm and 100nm respectively. When V_s=0.4V (Fig. 3-9b) the current density decrease 7.9%, 7.2% and 5.5% when R_{agg}=5nm, 50nm and 100nm respectively. When V_s=0.6V (Fig. 3-9c), after 1sec, the current density rises again. When R_{agg} value is larger than 500nm, the current density remains lower.

Figure 3-10 and 3-11 are the distribution of oxygen concentration and saturation level in the steady state with various agglomerate radii and V_s =0.4V. The oxygen consumptions are 20.3%, 11.7% and 2.6% of the inlet oxygen concentration inside the catalyst layer when R_{agg} =10nm, 200nm and 1000nm respectively. When the agglomerate is larger, the electrochemical reaction occurs only on the surface. The catalyst inside the agglomerate does not participate in the electrochemical reactions. Therefore the current density and the utilization of catalyst are inversed.

Figure 3-12 is the relationship between the current density and agglomerate radius in the steady state with various cell voltages. If the value of R_{agg} is too high, the current density will stay low. While the R_{agg} is below 80nm, the current density and agglomerate radius are independent.

(a)

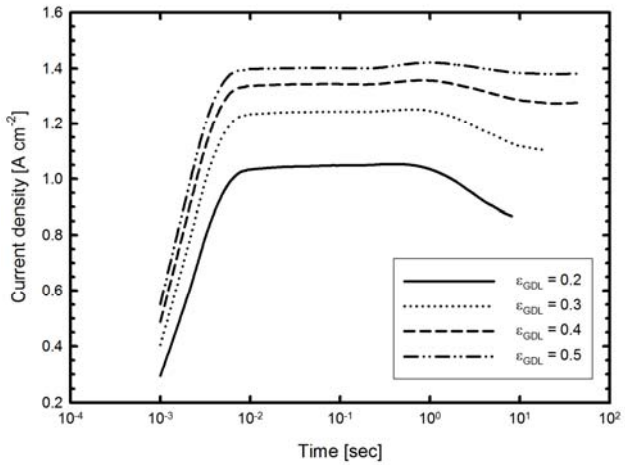

(b)

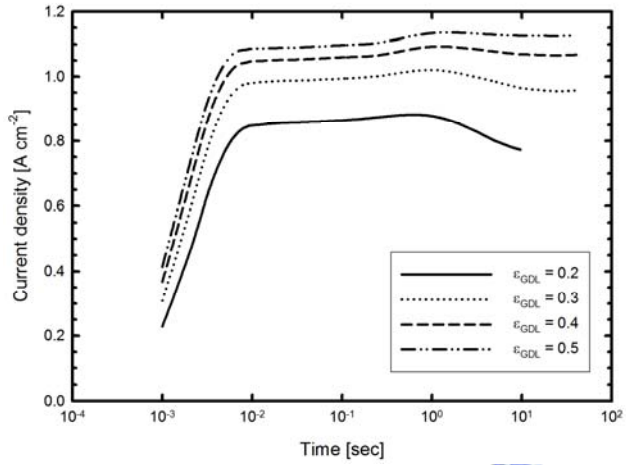

(c)

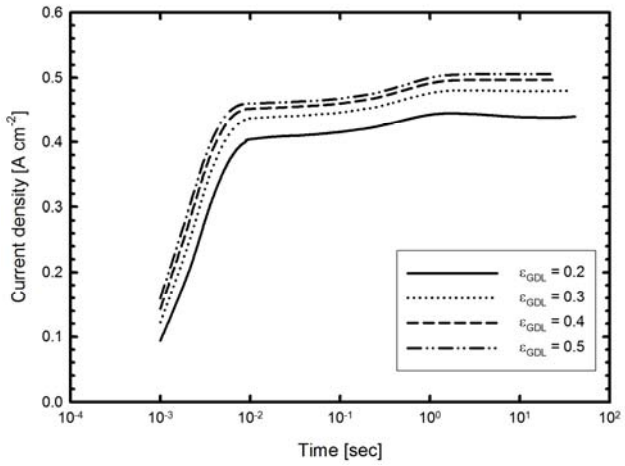

Fig 3-1.The evolution profiles of current density with various GDL porosity (a) V_s =0.2V, (b) V_s =0.4V, (c) V_s =0.6V

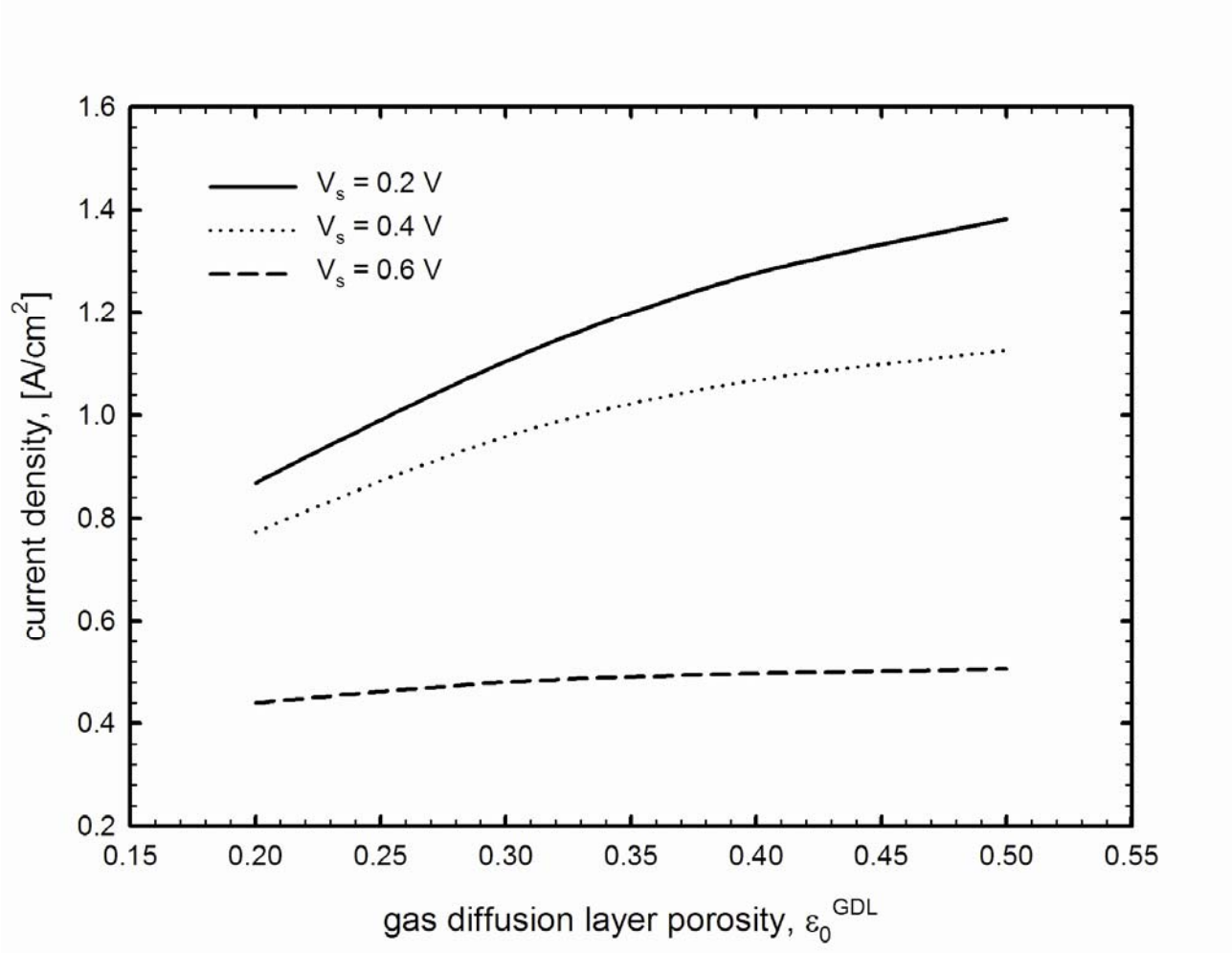

Fig 3-2.The Effect of gas diffusion layer porosity with various cell voltages in the steady state.

(a)

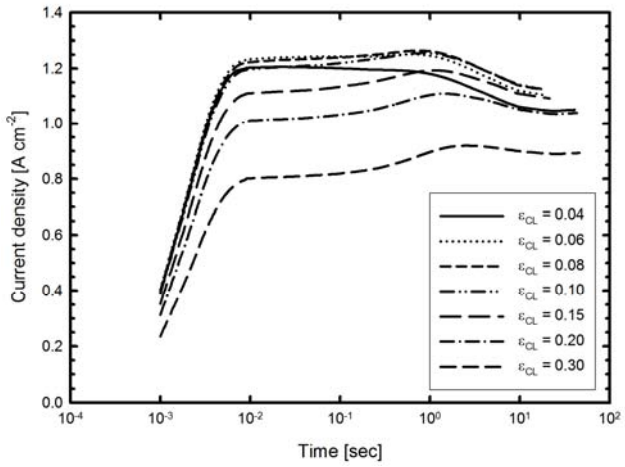

(b)

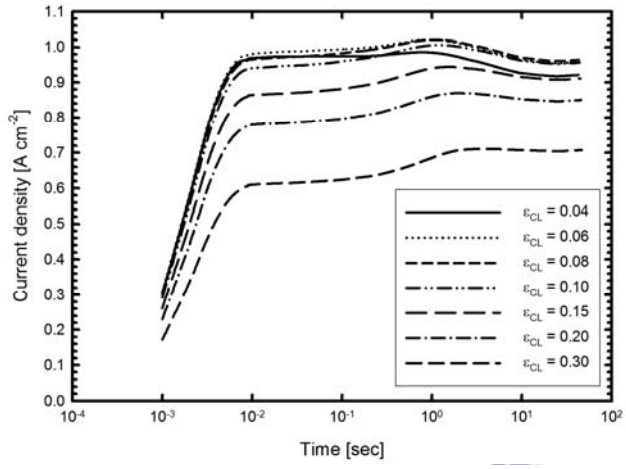

(c)

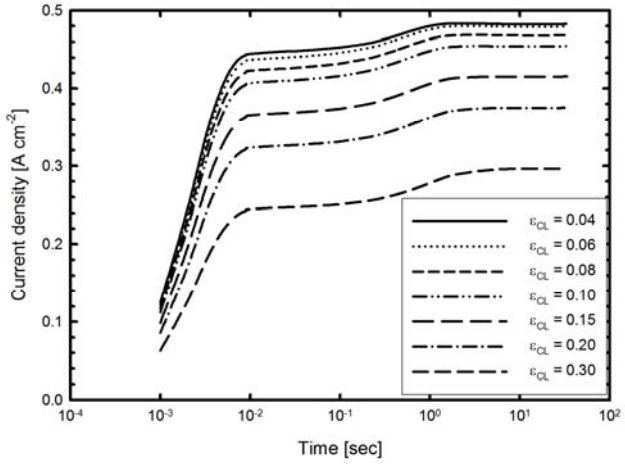

Fig 3-3.The evolution profiles of current density with various CL porosity (a) V_s =0.2V, (b) V_s =0.4V, (c) V_s =0.6V

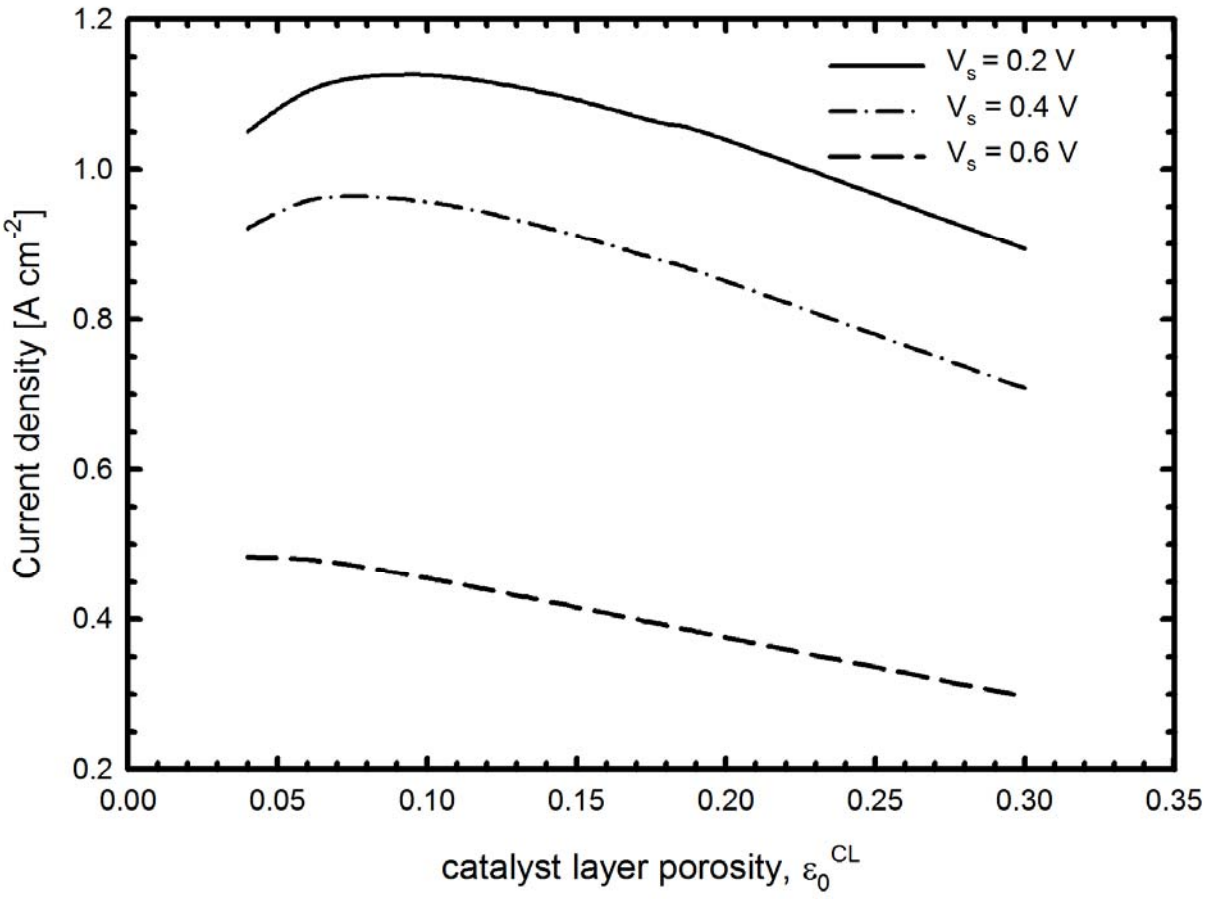

Fig 3-4.The effect of catalyst layer porosity with various cell voltages in the steady state.

(a)

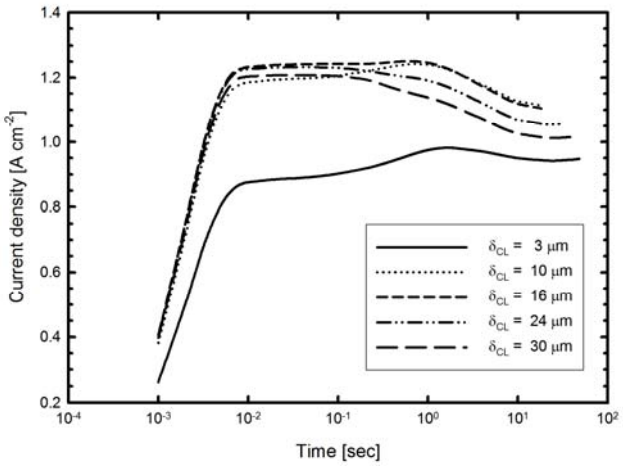

(b)

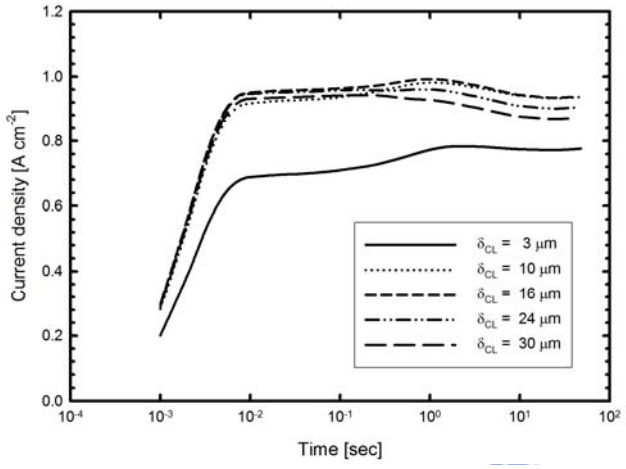

(c)

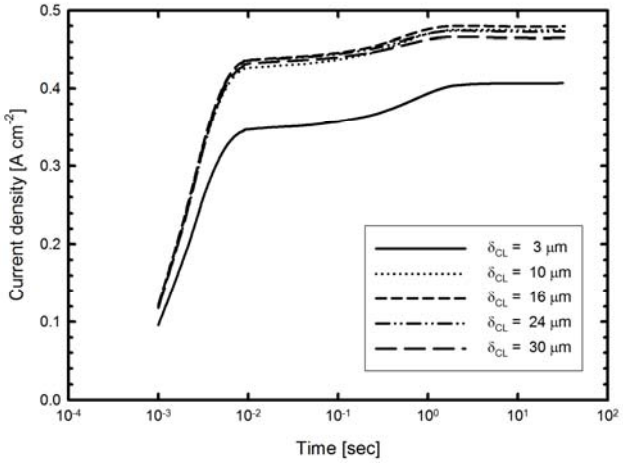

Fig 3-5.The evolution profiles of current density with various catalyst layer thicknesses (a) V_s =0.2V, (b) V_s =0.4V, (c) V_s =0.6V

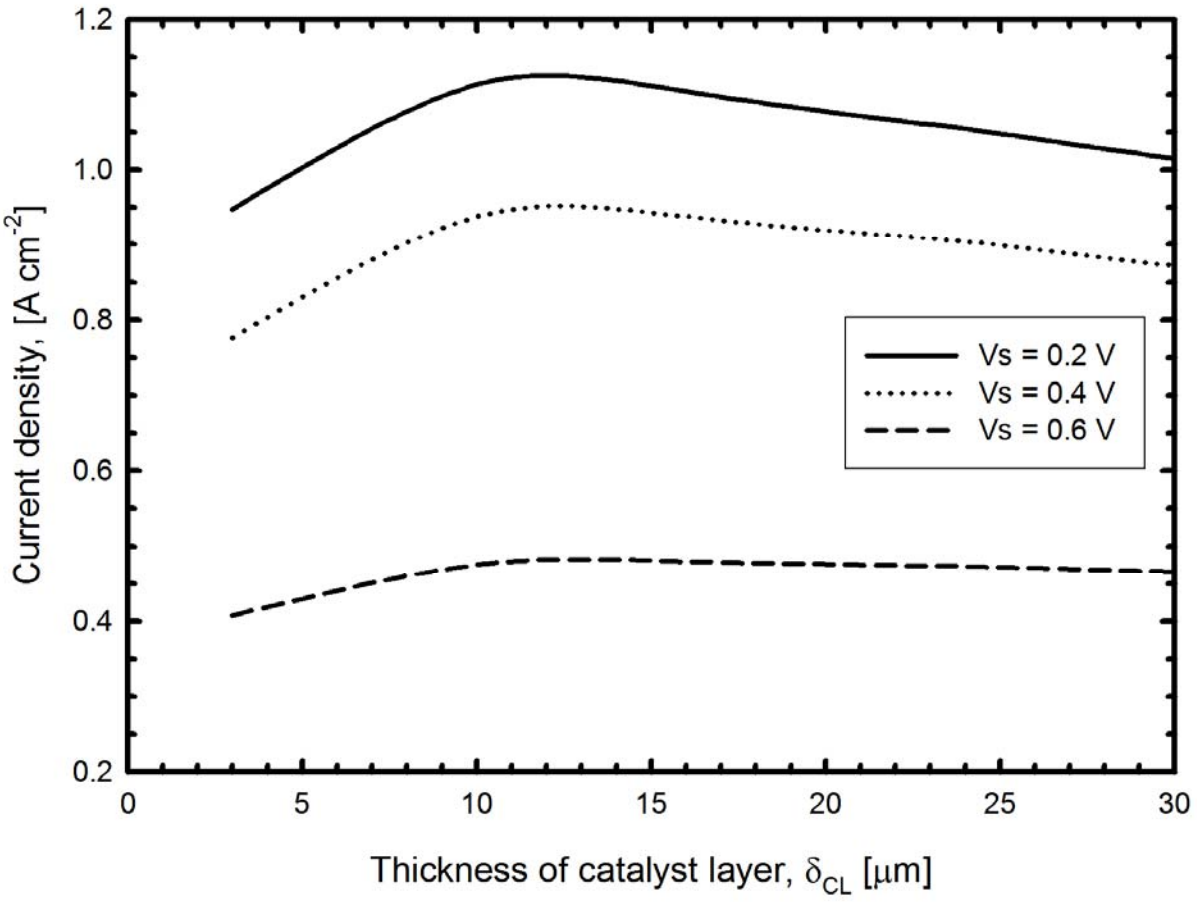

Fig 3-6.The effect of catalyst layer thickness with various cell voltages in the steady state.

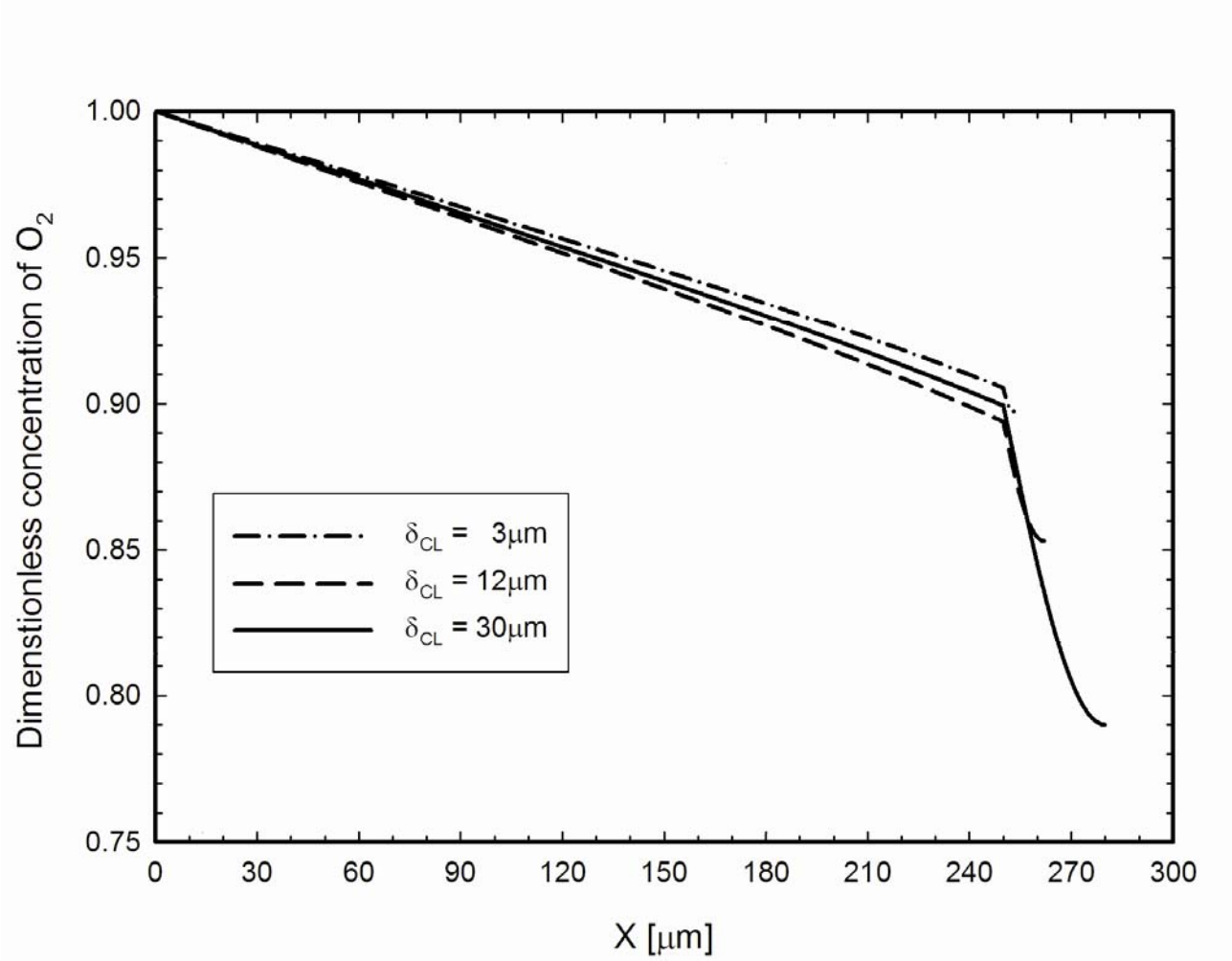

Fig 3-7.The distribution of dimensionless oxygen concentration with various CL thicknesses in the steady state. (V_s =0.6V and $R_{agg} = 80nm$)

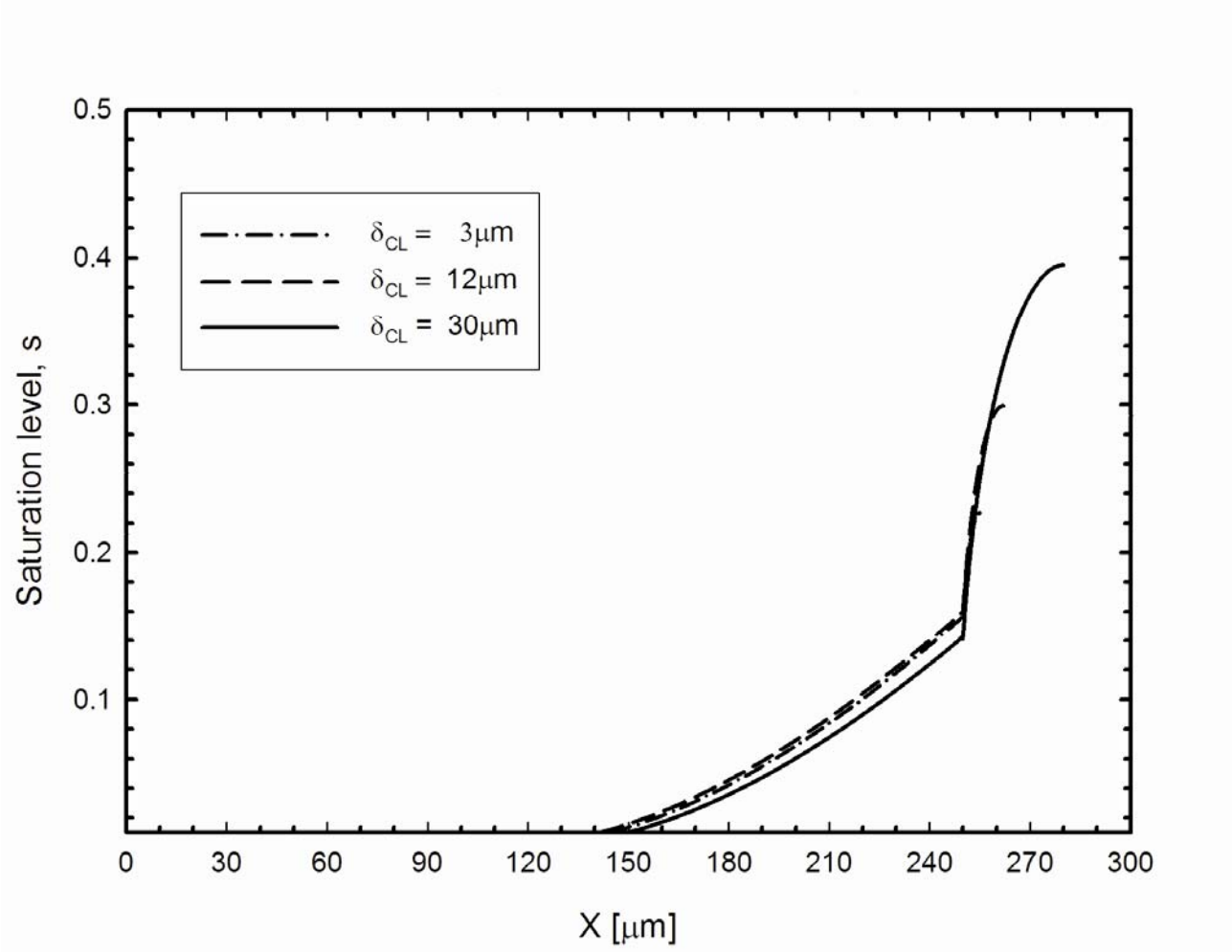

Fig 3-8.The distribution of saturation level with various CL thicknesses in the steady state.

(V_s =0.6V and $R_{agg} = 80nm$)

(a)

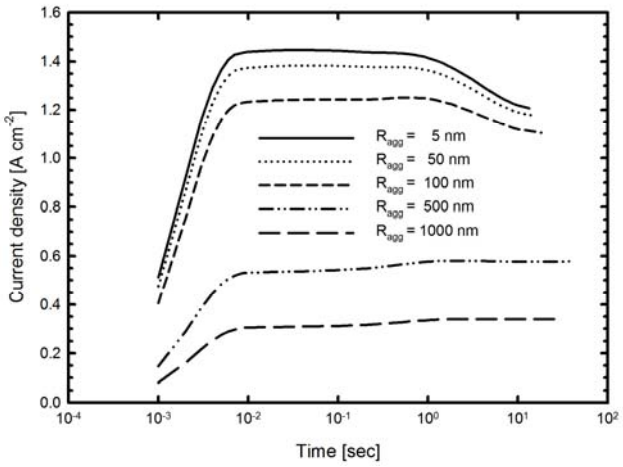

(b)

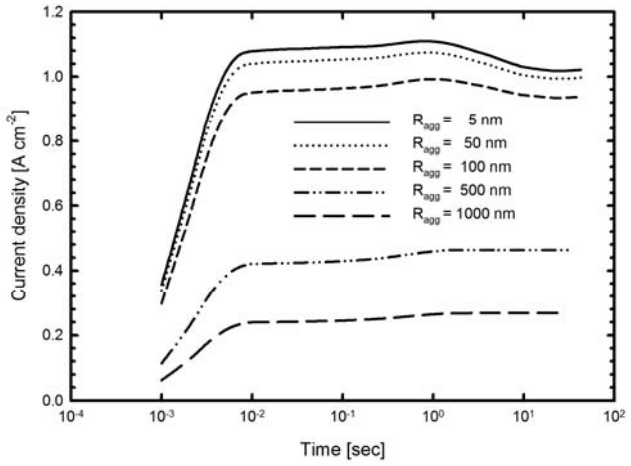

(c)

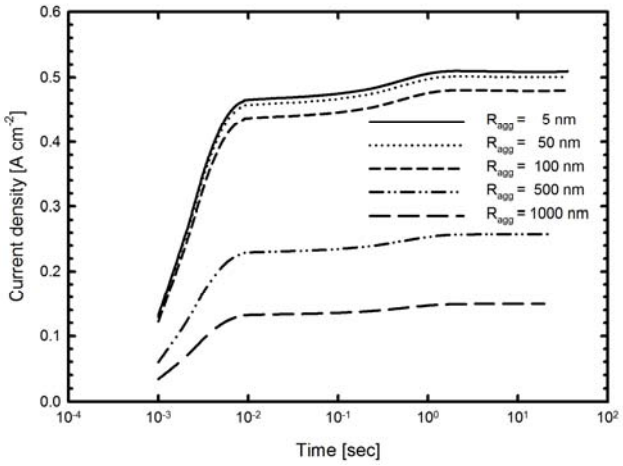

Fig 3-9.The evolution profiles of current density with various agglomerate radius. (a) V_s =0.2V, (b) V_s =0.4V, (c) V_s =0.6V

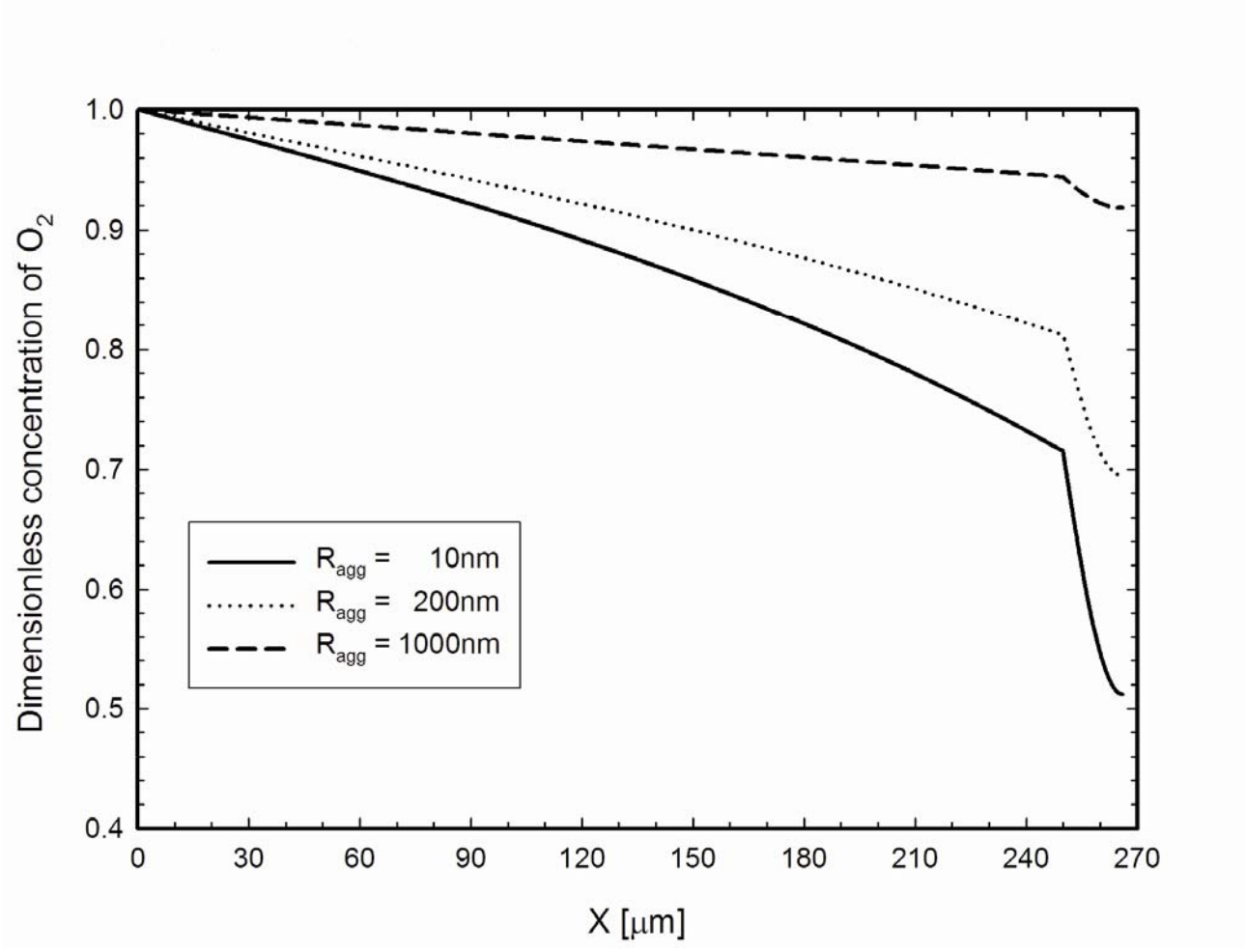

Fig 3-10.The distribution of dimensionless oxygen concentration with various agglomerate radii in the steady state. (V_s =0.4V and $\delta_{CL} = 16\mu m$)

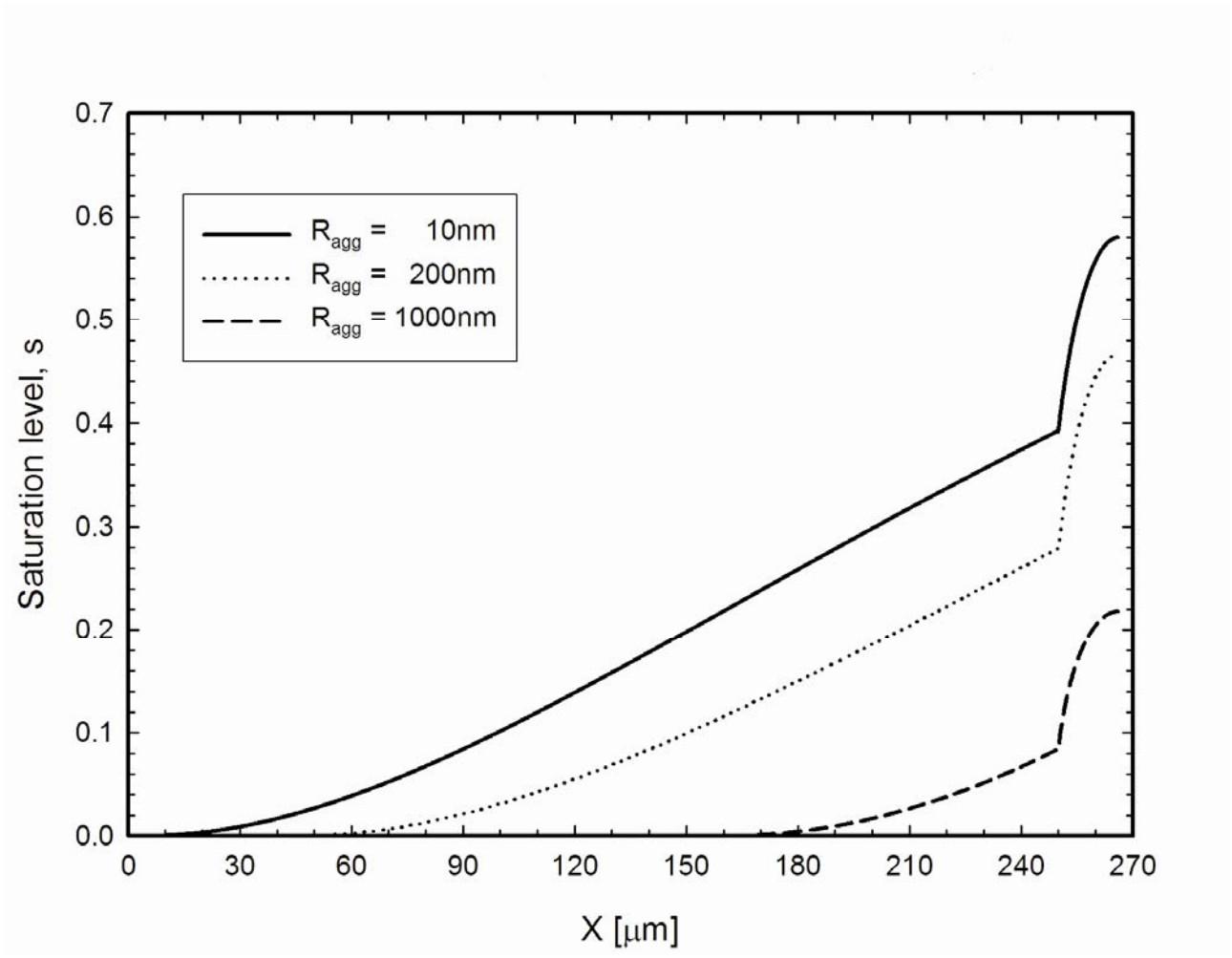

Fig 3-11.The distribution of saturation level with various agglomerate radii in the steady state.

(V_s =0.4V and $\delta_{CL} = 16\mu m$)

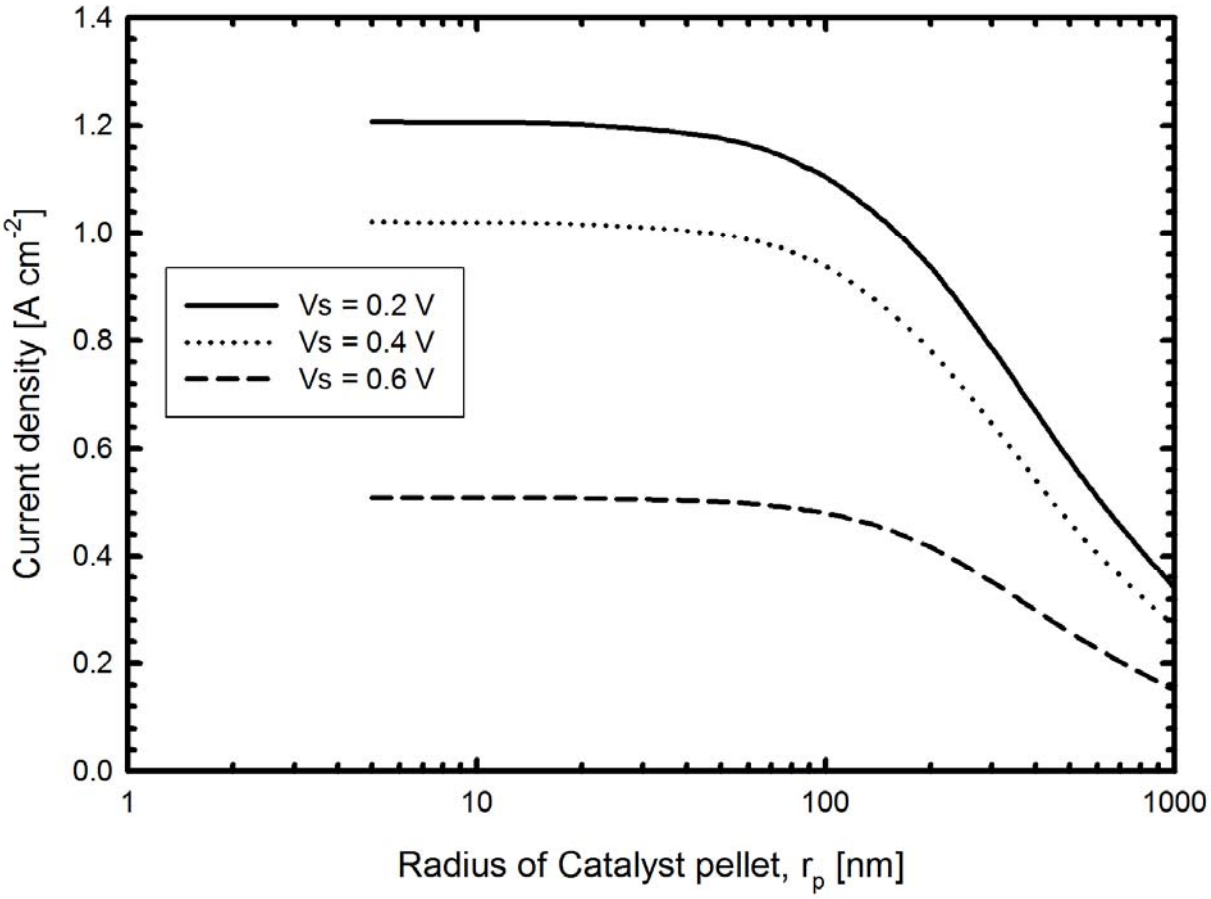

Fig 3-12.The effect of agglomerate radius with various cell voltages in the steady state.

4. Transient analysis of PEM fuel cells based on a spherical thin film-agglomerate model

Among the several components, the catalyst layer plays an essential role on the electrochemical reaction of a fuel cell. The structure and element combination affects the rate and efficiency of energy transformation drastically. The experimental results of TEM images by Siegel et al. [25] that carbon-supported, spherical Pt pellets exist in the catalyst layers. To mimic the actual morphology of the catalyst layers, a spherical thin film agglomerate expression along with a one-dimensional, two-phase model is developed in this chapter to investigate the transient evolutions of various model properties as well as cell performance. The boundary conditions at the CL/membrane interface also take into account the effects of water content on certain design parameters such as GDL permeability, CL permeability, catalyst loading, and GDL thickness.

4.1. Assumptions

The following assumptions are made in this chapter:

1. Electronic resistance is negligible in the GDL and CL.
2. The gas phase obeys the ideal gas law
3. The catalyst pellets are spherical, consist of carbon-supported platinum and Nafion, and are covered by a Nafion film.
4. All the catalyst pellets in the CL have the same radius and Nafion film thickness.
5. The catalyst pellets are homogeneous, and oxygen diffuses into them via the Nafion film.
6. The oxygen reduction reaction generates only liquid phase water.
7. The ionic potential between the anode catalyst layer and the membrane is approximately zero, because the hydrogen oxidation reaction is fast.

There are five variables used in the modeling:

(1). The concentration of oxygen in the gas phase, [$C_{O_2}^g$].

(2). The concentration of vapor water in the gas phase, [C_v^g].

(3). The liquid water saturation level, [s]. (the ratio between the liquid water volume and the total void volume in the porous medium)

(4). The concentration of liquid water in Nafion phase, [C_w^N].

(5). The ionic potential, [ϕ] (potential in Nafion phase).

4.2. Governing equations

4.2.1. Governing equations in the gas diffusion layer

The mass conservation equation for the oxygen is

$$\frac{\partial}{\partial \mathrm{t}}\left(\left(1-s\right)\varepsilon_0^{GDL}C_{O_2}^g\right)=\mathrm{D}_{\mathrm{O}_2}\varepsilon_0^{\mathrm{GDL}^\tau}\left[\left[\left(1-s\right)\right]^\tau\nabla^2C_{O_2}^g+\nabla\cdot\left[\left(1-s\right)\right]^\tau\nabla\cdot C_{O_2}^g\right] \tag{4-1}$$

LHS is the oxygen concentration's increasing rate with time. ε_0^{GDL} is the porosity of gas diffusion layer. The liquid water in GDL reduces the gas porosity, so that $\left(1-s\right)$. RHS is a diffusion term, and is the oxygen molar flux, and τ is tortuosity.

The mass conservation equation for the vapor water in the gas phase is

$$\frac{\partial}{\partial \mathrm{t}}\left(\left(1-s\right)\varepsilon_0^{GDL}C_v^g\right)=\mathrm{D}_{\mathrm{v}}\varepsilon_0^{\mathrm{GDL}^\tau}\left[\left[\left(1-s\right)\right]^\tau\nabla^2C_v^g+\nabla\cdot\left[\left(1-s\right)\right]^\tau\nabla\cdot C_v^g\right]-\mathrm{R}_{\mathrm{w}} \tag{4-2}$$

LHS is the concentration of vapor water. The 1st term of the RHS is the diffusion term. 2nd term is a source term. R_w is the interfacial transfer rate of water between liquid and vapor water.

$$R_w=k_c\frac{\varepsilon_0^{GDL}\left(1-s\right)y_v}{RT}\left(y_vP-P_v^{sat}\right)q+k_v\frac{\varepsilon_0^{GDL}s\rho_w}{M_w}\left(y_vP-P_v^{sat}\right)\left(1-q\right) \tag{4-3}$$

k_c and k_v are the condensation rate and evaporation rate constants respectively; y_v is the molar fraction of vapor water in the gas phase; P and P_v^{sat} are the operating pressure and water vapor saturation pressure respectively. M_w and ρ_w are the molecular weight and density of liquid water respectively. q is a switch function and is defined as,

$$q = \frac{1 + \left| y_v P - P_v^{sat} \right| \Big/ \left(y_v P - P_v^{sat} \right)}{2} \tag{4-4}$$

The liquid water transport in the GDL and CL is driven by capillary force. Darcy law is used to describe the flow of the liquid water in the porous media.

$$N_w = -\frac{\rho_w K_w(s)}{M_w \mu_w} \nabla P_l \tag{4-5}$$

P_l is the pressure of liquid water, and K_w is permeability of liquid water. Since

$$P_l = P_g - P_c \tag{4-6}$$

P_g is the gas phase pressure and is a constant over the domain. Eq.(4-5) becomes

$$N_w = -\frac{\rho_w K_w(s)}{M_w \mu_w} \nabla(-P_c) \tag{4-7}$$

The relation between the liquid water permeability and saturation level is linear [1].

$$K_s(s) = K_{w,0} s \tag{4-8}$$

$K_{w,0}$ is the permeability of liquid water at 100% saturation level. Thus,

$$N_w = -\frac{\rho_w K_{w,0}}{M_w \mu_w} \left(-\frac{dP_c}{ds} \right) s \nabla s \tag{4-9}$$

$\left(-\frac{dP_c}{ds} \right)$ is treated as a constant in order to reduce the total number of adjustable fitting parameters, and different values are used for different porous media, such as the GDL and CL. Therefore, the transport equation of liquid water saturation level is

$$\frac{\varepsilon_0^{GDL} \rho_w}{M_w} \frac{\partial s}{\partial t} = \frac{\rho_w K_{w,0}}{M_w \mu_w} \left(-\frac{dp_c}{ds} \right) \left(s \nabla^2 s + (\nabla \cdot s)^2 \right) + R_w \tag{4-10}$$

D_w^N is the diffusivity of liquid water in the Nafion phase and is function of the water content as listed in Table 4-3.

4.2.2. Governing equations in the catalyst layer

The mass conservation equation of oxygen in the gas phase is

$$\frac{\partial}{\partial t}\left(\left(1-s\right)\varepsilon_0^{CL}C_{O_2}^{g}\right)=D_{O_2}\varepsilon_0^{CL^{\tau}}\left[\left[\left(1-s\right)\right]^{\tau}\nabla^2 C_{O_2}^{g}+\nabla\cdot\left[\left(1-s\right)\right]^{\tau}\nabla\cdot C_{O_2}^{g}\right]-R_{O_2} \tag{4-11}$$

It is similar to the equation in the GDL, but the last term in RHS. The electrochemical reacts in the catalyst layer. R_{O_2} is a source term, but then oxygen is consumed in the CL.

Experimental studies [25, 71] have shown that the carbon-supported Pt catalysts in the CL are approximately spherical. As mentioned above, this chapter treats them as perfect spheres. The derivation of spherical thin film-agglomerate model described here is based on the cylindrical models in Chapter 2. The principal difference between the cylindrical model and the spherical model is the outer surface area per unit volume of the agglomerate. The surface area per unit volume of the agglomerate is defined as,

$$a_r=\frac{\text{Agglomerate's surface area}}{\text{Geometric volume}} \tag{4-12}$$

For spherical thin film-agglomerate model, a_r is

$$\begin{aligned} a_r &= \frac{4\pi\left(\mathrm{r_p}+\delta_N\right)^2}{\frac{4}{3}\pi\left(\mathrm{r_p}+\delta_N\right)^3/\left(1-\varepsilon_0^{CL}\right)} \\ &= \frac{3}{\left(\mathrm{r_p}+\delta_N\right)}\left(1-\varepsilon_0^{CL}\right) \end{aligned} \tag{4-13}$$

The reaction rate of oxygen within the catalyst pellets is

$$R_{O_2}=\frac{\frac{RT}{H_{O_2}^{N}}}{\frac{\delta_N}{a_r D_{O_2}^{N}}+\frac{\delta_w}{a_r D_{O_2}^{w}}+\frac{1}{\xi k_T}}C_{O_2}^{g} \tag{4-14}$$

$H_{O_2}^{N}$ and $H_{O_2}^{W}$ are the Henry's constants. $H_{O_2}^{N}$ is the oxygen between air and the Nafion phase and $H_{O_2}^{W}$ is the oxygen between air and liquid water. δ_N is the thickness of the Nafion film. $D_{O_2}^{N}$ is the diffusivity of oxygen in the Nafion, and $D_{O_2}^{w}$ is the diffusivity of oxygen in the liquid water. r_{Agg} is the radius of a catalyst pellet. Liquid water forms a film around the top of Nafion film. If it is not evaporated, its thickness can be estimated by

$$\delta_w = \frac{\varepsilon_0^{CL} s}{a_r} \tag{4-15}$$

The reaction rate constant

$$k_T = \left(1-\varepsilon_0^{CL}\right)\frac{1}{4FC_{O_2,eff}} a_{Pt}^{agg} i_0 \exp\left[-\frac{2.303\left(V_s-\phi-U_{ref}\right)}{b}\right] \tag{4-16}$$

The active catalyst surface area per unit volume of agglomerates

$$a_{Pt}^{agg} = \frac{a_{Pt} m_{Pt}}{\delta_{CL}\left(1-\varepsilon_0^{CL}\right)} \tag{4-17}$$

a_{Pt} is the surface area per mass. m_{Pt} is the catalyst loading of the electrode. δ_{CL} is the thickness of catalyst layer and b is the Tafel slope.

The effectiveness factor

$$\xi = \frac{1}{\varphi}\frac{3\varphi\coth\left(3\varphi\right)-1}{3\varphi} \tag{4-18}$$

The Thiele modulus

$$\varphi = \frac{r_{Agg}}{2}\sqrt{\frac{k_T \Big/ \left(1-\varepsilon_0^{CL}\right)}{D_{O_2,eff}^N}} \tag{4-19}$$

$D_{O_2,eff}^N$ is the effective diffusivity of oxygen in the Nafion phase within the catalyst pellets.

$$D_{O_2,.eff}^N = D_{O_2}^N\left[\left(1-\varepsilon_0^{CL}\right)\varepsilon_N^P\right]^\tau \tag{4-20}$$

ε_N^P is the volumetric fraction of Nafion within the catalyst pellets.

The mass conservation equation of vapor water in the gas phase is

$$\frac{\partial}{\partial \mathrm{t}}\left(\left(1-s\right)\varepsilon_0^{CL} C_v^g\right) = \mathrm{D_v}\varepsilon_0^{\mathrm{CL}^\tau}\left[\left[\left(1-s\right)\right]^\tau \nabla^2 C_v^g + \nabla\cdot\left[\left(1-s\right)\right]^\tau \nabla\cdot C_v^g\right] - \mathrm{R_w} \tag{4-21}$$

The transport equation of liquid water saturation level is

$$\frac{\varepsilon_0^{CL}\rho_w}{M_w}\frac{\partial s}{\partial t} = \frac{\rho_w K_{w,0}}{M_w \mu_w}\left(-\frac{dp_c}{ds}\right)\left(s\nabla^2 s + \left(\nabla\cdot s\right)^2\right) + R_w + \left(4n_d^{CL}+2\right)R_{O_2} \tag{4-22}$$

It is similar to the equation in the GDL, but the last term is generated by electrochemical reaction and electro-osmotic effect. n_d^{CL} is the net electro-osmotic drag coefficient and is a functions of the water content as listed in Table 4-3.

The mass conservation equation for the concentration of liquid water in Nafion phase is the same as the equation in GDL.

The flux expression of charges in the catalyst layer is

$$i_p = -\kappa_{N,eff} \nabla \phi \tag{4-23}$$

The conservation equation of ionic current is

$$\kappa_{N,eff} \nabla^2 \phi - 4FR_{O_2} = 0 \tag{4-24}$$

It is based on the stoichiometry of the oxygen reduction reaction. The consumption rate of protons is proportional to the reaction rate of oxygen $\kappa_{N,eff}$ is the effective electric conductivity of the Nafion phase.

$$\kappa_{N,eff} = \kappa_N \left[\left(1 - \varepsilon_0^{CL}\right) \varepsilon_N^P \right]^\tau \tag{4-25}$$

4.2.3. Governing equations in the membrane

In the membrane, the liquid water transport is driven by the water concentration gradient and electro-osmotic drag. The concentration of the liquid water in the Nafion phase is

$$\varepsilon_m \frac{\partial C_W^N}{\partial t} = D_w^N \nabla^2 C_w^N + \frac{n_d \kappa_N}{F} \nabla^2 \phi \tag{4-26}$$

κ_N and D_w^N are the bulk electric conductivity in the Nafion phase and diffusivity of liquid water in the Nafion phase, respectively. And both of them are function of the water content as listed in table 4-3.

In the anode, protons are produced and transported through the membrane to the catalyst layer. The flux expression of charges in the membrane is

$$i_p = -\kappa_N \nabla \phi \tag{4-27}$$

The electrochemical reaction does not react in the membrane. The equation of ionic current is

$$\nabla^2 \phi = 0 \tag{4-28}$$

4.3. Initial and boundary conditions

The simplification of all the differential equations and closure relations (governing and constitutive equations) previously presented allows one to write a system of five differential equations in the cathode of a PEMFC. Thus, one has to solve for 5 constitutive variables:

(1). The concentration of oxygen in the gas phase, [$C_{O_2}^{g}$].

(2). The concentration of vapor water in the gas phase, [C_{v}^{g}].

(3). The liquid water saturation level, [s]. (the ratio between the liquid water volume and the total void volume in the porous medium)

(4). The concentration of liquid water in Nafion phase, [C_{w}^{N}].

(5). The ionic potential, [ϕ].

To denote the location of a particular interface, the following notation will be used for subscripts in the expression of boundary conditions:

(1). The first letter symbolizes the domain:

GDL : gas diffusion layer,

CL : catalyst layer,

MEM : membrane.

(2). The second indicates the side of the interface:

\+ : higher values of x-coordinates, perpendicular to the surface,

\- : lower values of x-coordinates, perpendicular to the surface.

Oxygen concentration in the gas phase [$C_{O_2}^{g}\left(t,x\right)$]

The mass conservation equation for oxygen requires one initial condition and 4 boundary conditions

The initial condition is assumed to be zero. Thus,

$$C_{O_2}^{g}\left(0,x\right)=0 \tag{4-29}$$

At the gas channel boundary, we assume that inlet gas is air. Thus,

$$C_{O_2}^{g}\left(t,0\right)=C_{O_2}^{air} \tag{4-30}$$

At the interface between the GDL and CL, both the oxygen concentration and the oxygen flux are continuous so that,

$$C_{O_2}^g\Big|_{t,x=GDL^-} = C_{O_2}^g\Big|_{t,x=GDL^+} \tag{4-31}$$

$$N_{O_2}^g\Big|_{t,x=GDL^-} = N_{O_2}^g\Big|_{t,x=GDL^+} \tag{4-32}$$

At the interface between the CL and the membrane, it is assumed that no oxygen leaves, i.e.

$$N_{O_2}^g\Big|_{t,x=CL^-} = 0 \tag{4-33}$$

Vapor water concentration in the gas phase [$C_v^g\left(t,x\right)$].

The mass conservation equation for the concentration of vapor water requires one initial condition and 4 boundary conditions. The initial condition is assumed to be zero. Thus,

$$C_v^g\left(0,x\right) = 0 \tag{4-34}$$

At the gas channel boundary, we assume that inlet gas is air. Thus,

$$C_v^g\left(t,0\right) = C_v^{air} \tag{4-35}$$

At the interface between the GDL and CL, both the oxygen concentration and oxygen flux are continuous so that,

$$C_v^g\Big|_{t,x=GDL^-} = C_v^g\Big|_{t,x=GDL^+} \tag{4-36}$$

$$N_v^g\Big|_{t,x=GDL^-} = N_v^g\Big|_{t,x=GDL^+} \tag{4-37}$$

At the interface between the CL and the membrane, it is assumed that vapor water cannot permeate into the membrane, i.e.

$$N_v^g\Big|_{t,x=CL^-} = 0 \tag{4-38}$$

Saturation level of liquid water in porous media [$s\left(t,x\right)$]

The transport equation for the liquid water saturation level requires one initial condition and 4 boundary conditions. As to the initial condition, the saturation level profile is assumed to be zero, thus

$$s\left(0,x\right)=0 \tag{4-39}$$

At the gas channel boundary, it is assumed that there is no liquid water, i.e.

$$s(t,0)=0 \tag{4-40}$$

At the interface between the GDL and CL, it is assumed that the saturation level and liquid water flux is continuous. Thus,

$$s\big|_{t,x=GDL^-} = s\big|_{t,x=GDL^+} \tag{4-41}$$

$$N_w\big|_{t,x=GDL^-} = N_w\big|_{t,x=GDL^+} \tag{4-42}$$

At the interface between the CL and the membrane, the flux of liquid water saturation level is assumed to be zero.

$$N_w\big|_{t,x=CL^-} = 0 \tag{4-43}$$

Concentration of liquid water in Nafion phase [$C_w^N(t,x)$]

The mass conservation equation for the concentration of liquid water in Nafion phase requires one initial condition and 4 boundary conditions. As the initial state, the Nafion phase had fully hydrated. Thus the concentration of liquid water in Nafion phase is assumed to be in equilibrium with the vapor water activity in the gas phase, i.e.

$$C_w^N(0,x) = C_{w(anode)}^{N,eq} \tag{4-44}$$

$$C_{w(anode)}^{N,eq} = C_f\left(0.043+17.81\alpha-39.85\alpha^2+36.0\alpha^3\right) \tag{4-45}$$

At the interface between the GDL and CL, the flux of liquid water in Nafion phase is assumed to be zero, i.e.

$$N_w^N\big|_{t,x=GDL^+} = 0 \tag{4-46}$$

The CL/membrane interface boundary condition for the concentration of liquid water in the Nafion phase (Equation 3) is taken from the model of Lin & Nguyen [92], where the water content below 14 mol H_2O/mol SO_3^- was determined by water vapor activity. When the gas stream is saturated, however, and liquid water exists in the pores of the CL (between 14 and 16.8 mol H_2O/mol SO^-_3), the water content varies linearly with the liquid water saturation level [27]. Since liquid water is generated when a fuel cell starts up, any liquid water in the CL/MEM interface pores can dissolve into the Nafion phase. This leads to the boundary condition

$$C_w^N\Big|_{t,x=CL+} = C_f\left(0.043+17.81\alpha-39.85\alpha^2+36.0\alpha^3\right)+2.8C_f s \tag{4-47}$$

At x=L , the concentration of liquid water in membrane is assumed to be in equilibrium with the vapor water activity in the gas phase.

$$C_w^N\Big|_{t,x=L} = C_{w(anode)}^{N,eq} \tag{4-48}$$

Ionic potential [$\phi(t,x)$]

The potential equation requires 4 boundary conditions. At the GDL boundary, the ionic current is zero.

$$i_p\Big|_{x=GDL^+} = 0 \tag{4-49}$$

At the interface between the CL and the membrane, the ionic potential and ionic current are continuous. Thus,

$$\phi\Big|_{x=CL^-} = \phi\Big|_{x=CL^+} \tag{4-50}$$

$$i_p\Big|_{x=CL^-} = i_p\Big|_{x=CL^+} \tag{4-51}$$

At x=L , the ionic potential is zero.

$$\phi\Big|_{x=L} = 0 \tag{4-52}$$

4.4. Methods of solution

The numerical solution techniques used here are the same as in the Chapter 2 and the solution procedure is showed in the Figure 2-3.

The governing equations and boundary conditions are discretized by the finite difference method. The convergence criteria for a steady state are

$$\left|\frac{V_i^{new}-V_i^{old}}{V_i^{old}}\right| \le 1\times10^{-4} \tag{4-53}$$

where V_i is an arbitrary variable.

4.5. Results and discussion

Water management plays an important role on the performance of PEM fuel cells. Understanding their starting process and performance evolution are also crucial in the actual operating applications. Simulation results for this issue by employing the PEM fuel cell cathode model is presented in the following sections. Investigations on how the structural parameters of the cell such as GDL permeability, CL permeability, catalyst loading, and GDL thickness affect its performance are also demonstrated.

To validate the numerical model, the comparison of calculation results and Navessin et al.'s experimental results are carried out. The comparison results are shown in Figure 4-2. The experimental operating conditions and parameters of Navessin et al. are listed in Table 4-4, and those of the model are listed in Table 4-5. The I-V polarization curve represents the fuel cell's steady state at an operating temperature of $25^{o}C$. The PEM fuel cell operates under uniform conditions from the time it is turned on until a steady state is achieved. It is found that current model results agree well with the experimental data.

Figure 4-3 shows the evolution of the liquid water saturation level, measured at various cell voltages. The liquid water saturation level plot can be divided into four sections. From startup to 10^{-2} sec, liquid water accumulates in the catalyst layer. Between 10^{-2} sec and 0.5 sec, liquid water begins diffusing into the gas diffusion layer. During the next phase, from 0.5 sec to 2 sec, the liquid water saturation level in the CL decreases as more and more liquid water occupies pores in the GDL. In the final phase, the liquid water saturation level increase in both CL and GDL until a steady state is reached. Although the liquid water saturation level decreases in the CL between 0.5 sec and 2 sec, note that it will increase again once the electrochemical reaction rate generates enough liquid water to fill the Nafion phase. When V_s =0.6 V, for example, the electrochemical reaction rate is moderate and less liquid water is generated. In this case, at the time after 2 sec, the liquid water saturation level decreases (Fig. 4-3c). In contrast, the liquid water saturation level increases after 2 sec for V_s =0.2 V and 0.4 V (Figs. 4-3a, 4-3b).

Figure 4-4 demonstrates the evolution profiles of ionic potential at various cell voltages. When the cell voltage is higher, both oxygen reduction reaction and the loss of ionic potential will be lower. When the cell voltage is lower (i.e., the current density increases), oxygen reduction reaction and the loss of ionic potential will be larger. It can be clearly seen from Fig. 4-4 that the ionic potential will not decrease monotonically with time. It reaches a critical value then increases with time until the steady state is obtained. Thus the difference between the critical value and the steady

state of any given ionic potential is dependent on the cell voltage applied. When the cell voltage is 0.2V, the difference is about 20%. The ionic potential reaches 80% of its critical value in 0.005sec and reaches the critical value in the order of 10^{-1} sec.

Figure 4-5 presents the evolution profiles of oxygen concentration at various cell voltages. At the initial state, it assumes that there is no oxygen in the cell. After start up, the oxygen transport from the gas channel to the catalyst layer via gas diffusion layer. In the gas diffusion layer, the oxygen diffuses continuously to the catalyst layer along the pores. In the meantime, the oxygen dissolves into the Nafion film and reaches the pellet surface. Then liquid water is generated. At the inlet, the distribution of oxygen concentration is constant. Within 5sec, it changes dramatically at the very beginning and then decreases with time in the catalyst layer. After 5sec, when V_s=0.2V and 0.6V, it remains. But when V_s=0.4V, the turning point is 10sec. After 5sec and when V_s=0.2V, the oxygen transport is affected by liquid water. When V_s=0.4V, the liquid water is less than when V_s=0.2V, thus it needs more time to reach the steady state. When V_s=0.6V, because the electrochemical reaction reacts moderately, it consumes less oxygen. And it generates less liquid water than others, thus it reaches the steady state quickly.

The fuel cell cannot be turned on if the Nafion phase is completely dry, so it is assumed that the concentration of liquid water in the Nafion phase is equal to the concentration of fixed charge sites at the anode. Figure 4-6 shows the evolution of the CL water content over time at three different cell voltages. These plots can be divided into three sections: from startup to 3 sec, the water content decreases; from 3 sec to 13 sec, the water content increases; and in the final phase, the water content is constant. Initially there is less liquid water amount in the gas pores than in the Nafion phase, so at first liquid water flows from the Nafion phase to the gas pores. When more liquid water begins to be generated, it dissolves into the Nafion phase again and we see increasing water content in both the CL and the membrane.

Figure 4-7 displays the evolution of the total ionic potential drop (IPD) in the catalyst layer, for three different cell voltages V_s.

$$\text{IPD} = \sum_{x=GDL}^{x=CL} \left(\phi_p \big|_{x=CL} - \phi_p(x) \right). \tag{4-54}$$

This plot can be divided into five sections: (1) a rapid rise, which lasts from startup to 0.01 sec; (2) from 0.01 sec to 0.1sec, the potential plateaus (remains approximately constant); (3) at 0.1 sec the potential rises rapidly again to its maximum value; (4) the potential drops again; and (5) a second

plateau is reached representing the steady state.

The total dimensionless oxygen consumption (TOC) in the catalyst layer also evolves over time, as shown in Figure 4-8. This quantity is defined as

$$\mathrm{TOC} = \sum_{x=GDL}^{x=CL} \frac{C_{O_2}^{g}\Big|_{x=GDL} - C_{O_2}^{g}(x)}{C_{O_2}^{g,inlet}}. \tag{4-55}$$

The plot can be divided into six sections: (1) a rapid rise from startup to 5×10^{-3} sec; (2) the first plateau, which lasts from 5×10^{-3} sec to 5×10^{-2} sec (consumption increases slightly during this phase); (3) another rise from 5×10^{-2} sec to 0.5 sec; (4) a second plateau from 0.5 sec to 2 sec (where the consumption decreases slightly); (5) a rapid rise to the peak value from 2 sec onward; and finally (6) a steady-state plateau. Oxygen consumption increases less than 15% in the first plateau, and decreases by only 2% in the second plateau. As the IPD increases, the fuel cell must overcome higher and higher activation energies to maintain a higher rate of electrochemical reaction. After the fuel cell overcomes the maximum activation energy, the IPD decreases. As shown in Fig. 4-8, when V_s=0.2 V and 0.4 V, after 2 sec, the TOC increases rapidly. Thus, after a fuel cell overcomes the maximum activation energy, it retains a high electrochemical reaction rate with a lower IPD.

The current density evolution for various cell voltages is shown in Figure 4-9. These plots can be divided into five sections. From startup to 5×10^{-3} sec, the current density rises rapidly. From 5×10^{-3} sec to 2×10^{-2} sec, the current density plateaus. The current density begins to rise rapidly again at 2×10^{-2} sec, eventually reaching its maximum value, then drops briefly. Finally, it reaches a steady-state plateau. As seen in Fig. 4-3, liquid water hinders oxygen transport as it diffuses from the CL to the GDL. The electrical conductivity is also reduced during this period, due to decreased water content, and the current density levels off as a result. Note that the total oxygen consumption increases rapidly after 0.05 sec (Fig. 4-8), and that the ionic potential drop increases rapidly after 0.1 sec (Fig. 4-7). Thus, the current density increases rapidly after 0.1 sec. Oxygen transport resistance increases after 0.1 sec, however, because at this point the liquid water saturation level is increasing in both GDL and CL (Fig.4-3). Thus, the current density levels off after 1 sec.

The current density drops off after reaching its maximum value for the following reason. The higher the current density, the more liquid water is generated and the more gas pores are occupied by liquid water. When this happens, however, the catalyst pellets also have less oxygen on their exposed surface. This tends to reduce the electrochemical reaction rate and causes a drop in the

current density. At lower cell voltages the electrochemical reaction rate is higher, so more liquid water is generated and we see a more extreme drop in the current density. For instance, when V_s =0.2 V the drop is more than 30%

Figure 4-10 shows the effect of modifying GDL permeability for V_s =0.4 V. Cases 1 through 4 used permeabilities of 9×10^{-10} cm^2, 1×10^{-9} cm^2, 1×10^{-8} cm^2, and 1×10^{-7} cm^2 respectively. The higher the permeability, the more liquid water will be drained; this lowers the amount of liquid waver available and reduces the current density. If the GDL permeability is too low, however, liquid water cannot drain effectively. This will reduce the available oxygen on the catalyst surface, decreasing cell performance and limiting mass transport.

Figure 4-11 examines the effect of CL permeability when V_s =0.4V; cases 1 through 4 use values of 8×10^{-12} cm^2, 3×10^{-11} cm^2, 3×10^{-10} cm^2, and 3×10^{-9} cm^2, respectively. Cases 3 and 4 have the highest permeabilities and effective water drainage. But when liquid water drains from the fuel cell quickly, it also reduces the water content of the Nafion phase. Thus, a lower CL permeability means that there will be more liquid water in the Nafion phase. The maximum current densities achieved in cases 1 and 2 are similar, but the steady-state current density in Case 2 is higher. This is because in case 1, liquid water is occupying more of the gas pores and effectively covering the catalyst pellet surface, causing series concentration overpotential.

The current density evolution for V_s =0.4V is shown in Figure 4-12, under catalyst loadings of 0.2 mg, 0.3 mg, 0.4 mg, and 0.5 mg for Cases 1 through 4 respectively. A higher catalyst loading means a more rapid electrochemical reaction. The current densities in Cases 1 and 2 are obviously lower than those in Cases 3 and 4, because the catalyst loading is too low in the former to drive the reaction. The maximum current density in Case 4 drops rapidly, on the other hand, because of fuel cell flooding. Oxygen cannot reach the surface of the catalyst pellets when there is too much liquid water. This suggests that excessive catalyst loading does not improve cell performance.

Finally, Figure 4-13 demonstrates the evolution of current density for V_s =0.4V under various thicknesses of the gas diffusion layer. Through Case 1 to 6, the thicknesses are 220 μm, 235 μm, 240 μm, 245 μm, 250 μm, and 265 μm, respectively. The current density increases to a constant (steady state) value after 2 sec for GDL layers less than or equal to 240 μm thick. For the remaining cases, the current density rises again after 2 sec, reaches its maximum, then decreases in value and reaches a steady state. A thicker gas diffusion layer means a higher maximum current density, but this value may overshoot the sustainable current. Thicker GDL also imposes a greater

resistance to liquid water transport, which promotes flooding of the fuel cell. Liquid water drains more quickly with a thinner gas diffusion layer, but the fuel cell cannot be too dry or its performance will deteriorate.

Table 4-1. Governing equations

Variables	GDL	CL	MEM
$C_{O_2}^{g}$	$\frac{\partial}{\partial t}\left((1-s)\varepsilon_0^{GDL}C_{O_2}^{g}\right)=$ $D_{O_2}\varepsilon_0^{GDL^{\tau}}\left[\left[(1-s)\right]^{\tau}\nabla^2 C_{O_2}^{g}+\nabla\cdot\left[(1-s)\right]^{\tau}\nabla\cdot C_{O_2}^{g}\right]$	$\frac{\partial}{\partial t}\left((1-s)\varepsilon_0^{CL}C_{O_2}^{g}\right)=-R_{O_2}+$ $D_{O_2}\varepsilon_0^{CL^{\tau}}\left[\left[(1-s)\right]^{\tau}\nabla^2 C_{O_2}^{g}+\nabla\cdot\left[(1-s)\right]^{\tau}\nabla\cdot C_{O_2}^{g}\right]$	-
C_{v}^{g}	$\frac{\partial}{\partial t}\left((1-s)\varepsilon_0^{GDL}C_{v}^{g}\right)=-R_{w}+$ $D_{v}\varepsilon_0^{GDL^{\tau}}\left[\left[(1-s)\right]^{\tau}\nabla^2 C_{v}^{g}+\nabla\cdot\left[(1-s)\right]^{\tau}\nabla\cdot C_{v}^{g}\right]$	$\frac{\partial}{\partial t}\left((1-s)\varepsilon_0^{CL}C_{v}^{g}\right)=-R_{w}+$ $D_{v}\varepsilon_0^{CL^{\tau}}\left[\left[(1-s)\right]^{\tau}\nabla^2 C_{v}^{g}+\nabla\cdot\left[(1-s)\right]^{\tau}\nabla\cdot C_{v}^{g}\right]$	-
S	$\frac{\varepsilon_0^{GDL}\rho_w}{M_w}\frac{\partial s}{\partial t}=R_w+$ $\frac{\rho_w K_{w,0}}{M_w\mu_w}\left(-\frac{dp_c}{ds}\right)\left(s\nabla^2 s+(\nabla\cdot s)^2\right)$	$\frac{\varepsilon_0^{CL}\rho_w}{M_w}\frac{\partial s}{\partial t}=\left(4n_d^{CL}+2\right)R_{O_2}+R_w+$ $\frac{\rho_w K_{w,0}}{M_w\mu_w}\left(-\frac{dp_c}{ds}\right)\left(s\nabla^2 s+(\nabla\cdot s)^2\right)$	-
C_{w}^{N}	-	$\varepsilon_m^{CL}\frac{\partial C_W^N}{\partial t}=D_w^N\nabla^2 C_w^N$	$\varepsilon_m\frac{\partial C_W^N}{\partial t}=D_w^N\nabla^2 C_w^N+\frac{n_d\kappa_N}{F}\nabla^2 V_+$
ϕ	-	$\kappa_{N,eff}\nabla^2\phi-4FR_{O_2}=0$	$\nabla^2\phi=0$

Table 4-2. Boundary conditions

Variables	X=0	GDL/CL	CL/MEM	X=L
$C_{O_2}^{g}$	$C_{O_2}^{g}=C_{O_2}^{air}$	$N_{O_2}^{g}\big\|_{GDL}=N_{O_2}^{g}\big\|_{GDL}$	$N_{O_2}^{g}\big\|_{CL}=0$	-
C_{v}^{g}	$C_{v}^{g}=C_{v}^{air}$	$N_{v}^{g}\big\|_{GDL}=N_{v}^{g}\big\|_{GDL}$	$N_{v}^{g}\big\|_{CL}=0$	-
S	s=0	$N_{w}\big\|_{GDL}=N_{w}\big\|_{GDL}$	$N_{w}\big\|_{CL}=0$	-
C_{w}^{N}	-	$N_{w}^{N}\big\|_{GDL}=0$	$C_{w}^{N,eq}=\left(0.043+17.81\alpha-39.8\alpha^{2}+36.0\alpha^{3}\right)C_{f}+2.8C_{f}s$	$C_{w}^{N}\big\|_{MEM}=C_{w(anode)}^{N,eq}$
ϕ	-	$i_{p}\big\|_{GDL}=0$	$i_{p}\big\|_{CL}=i_{p}\big\|_{CL}$	$\phi=0$

Table 4-3. Correlations used in Chapter 4.

Diffusivity of Oxygen in Nafion membrane[64]	$D_{O_2}^N = 0.0031\exp\left(-\frac{2768}{T}\right)$	cm^2/s
Diffusivity of Oxygen in liquid water	$D_{O_2}^W = 2.41\times10^{-5}\left(\frac{\mu_{T_r}}{\mu_T}\right)^{1.026}\left(\frac{T}{T_r}\right)$	cm^2/s
Diffusivity of Oxygen in gas stream[93]	$D_{O_2}^g = 0.1775\left(\frac{T}{273.15}\right)^{1.823}$	cm^2/s
Diffusivity of vapor water in gas stream[93]	$D_v^g = 0.256\left(\frac{T}{307.15_r}\right)^{2.334}$	cm^2/s
Henry's constant for oxygen between Nafion and air[64]	$H_{O_2}^N = 1.33\times10^6\exp\left(\frac{-498}{T}\right)$	cm^3/mol
Henry's constant for oxygen between liquid water and air[2]	$H_{O_2}^N = 1.33\times10^6\exp\left(\frac{-498}{T}\right)$	cm^3/mol
Water content	$\lambda = C_w^N / C_f$	
Net electro-osmotic drag coefficient[27]	$n_d = 2.5/22\lambda$	
Conductivity of Nafion membrane[27]	$\kappa_N = \exp\left[1268\left(\frac{1}{303}-\frac{1}{T}\right)\right](0.005139\lambda-0.00326)$	$l/\Omega cm$
Diffusivity of liquid water in Nafion membrane[27]		cm^2/s
	$C_{w(2>\lambda\geq3)}^N = 10^{-6}\exp\left[2416\left(\frac{1}{303}-\frac{1}{T}\right)\right](-3.1+2.0\lambda)$	
	$C_{w(3>\lambda\geq4)}^N = 10^{-6}\exp\left[2416\left(\frac{1}{303}-\frac{1}{T}\right)\right](6.89-1.33\lambda)$	
	$C_{w(\lambda>4)}^N = 10^{-6}\exp\left[2416\left(\frac{1}{303}-\frac{1}{T}\right)\right](2.563-0.33\lambda+0.0246\lambda^2-0.000671\lambda^3)$	

Table 4-4. Parameters used by Navessin et al.[82]

Gas diffusion layer properties			
	Porosity	0.6	
	Thickness	0.035	cm
Catalyst layer properties			
	Porosity	0.55	
	Thickness	0.005	cm
	Catalyst loading (m_{Pt})	0.78	mg
	Area per unit volume [1]	727,664	m^{-1}
	Volumetric fraction of Naion in catalyst pellet (ε^{P}_{N})	0.2	
	Raduis of catalyst pellet, (R_{agg})	2.5×10^{-5}	cm
	Exchange current density [1]	1.27,1.66	mA cm^{-2}
	Reference concentration of O_2,($C_{o_2,ref}$)[1]	2.34,2.25	μmol cm^{-3}
Membrane properties			
	Porosity	0.35	
	Thickness[1]	0.0062, 0.0061	cm
Operation conditions			
	Temperature	25.0	^{o}C
	Pressure	1.0	atm

[1] Lists value for HMEA-2 and HMEA-3, respectively.

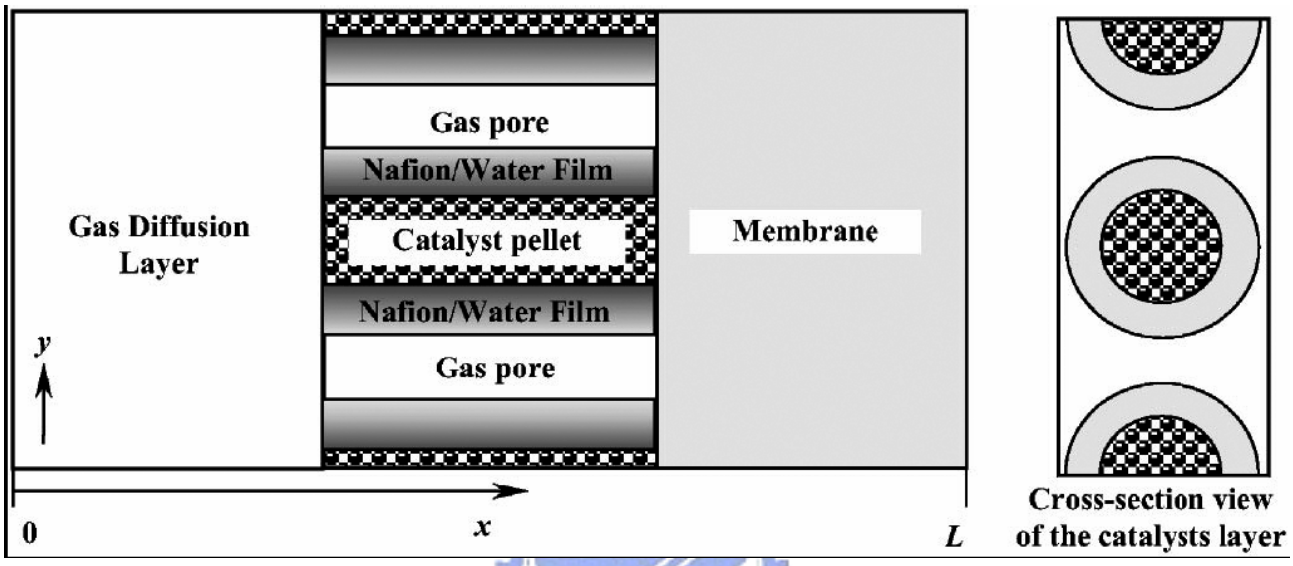

Fig 4-1. Schematic of the model domain. [91]

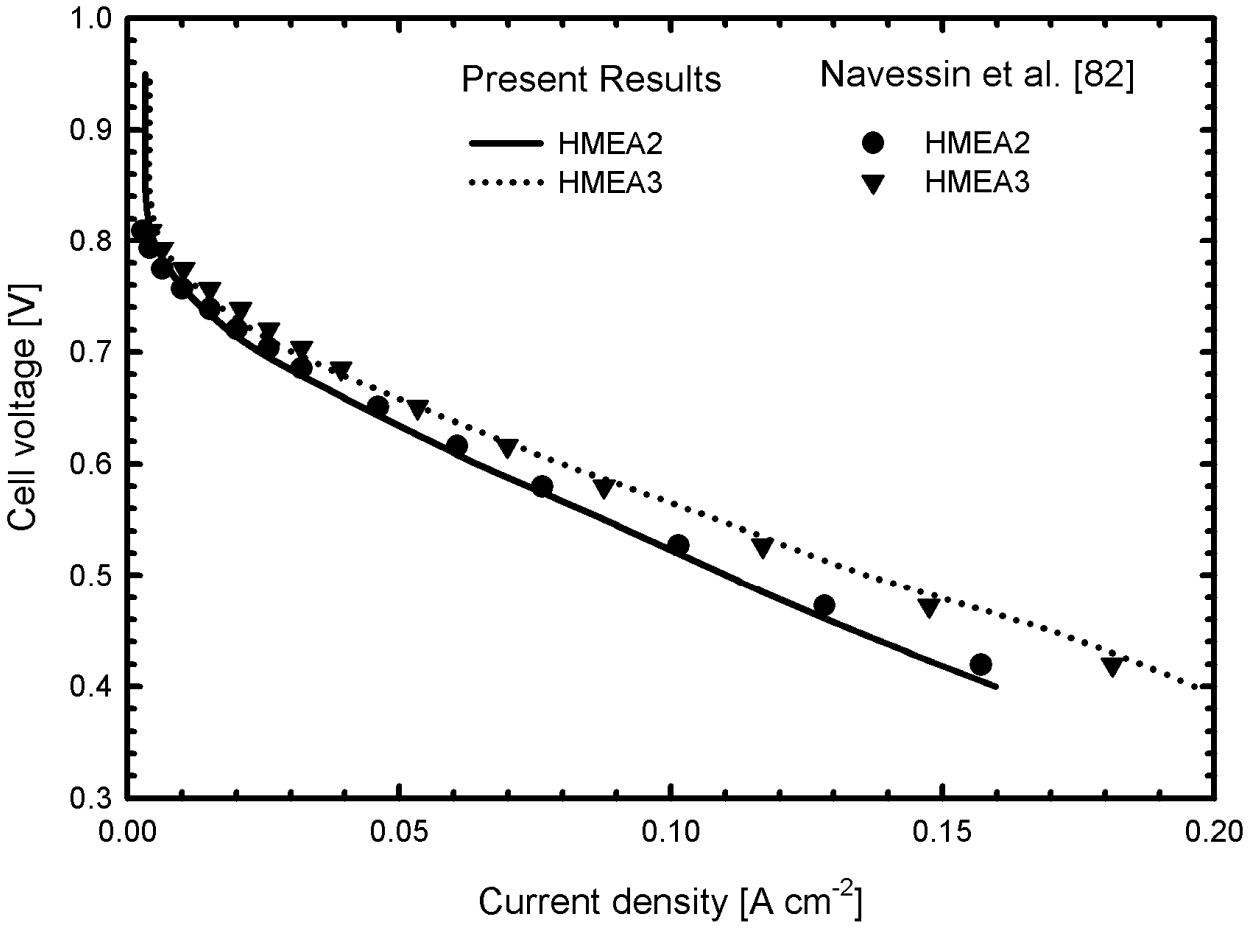

Fig 4-2. A comparison of the model to experimental data.

(a)

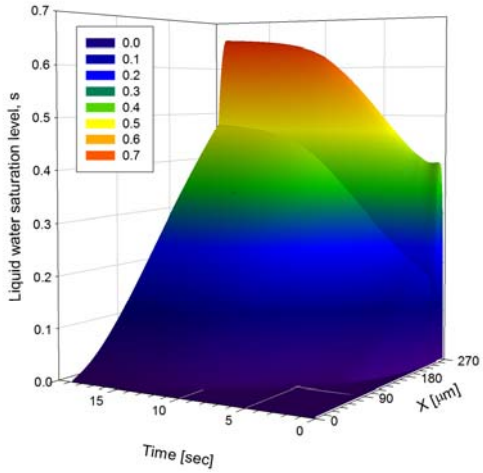

(b)

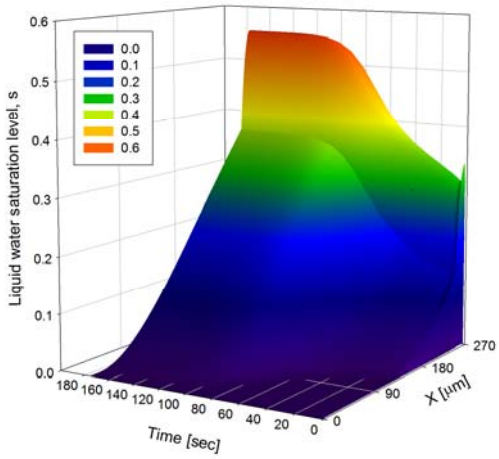

(c)

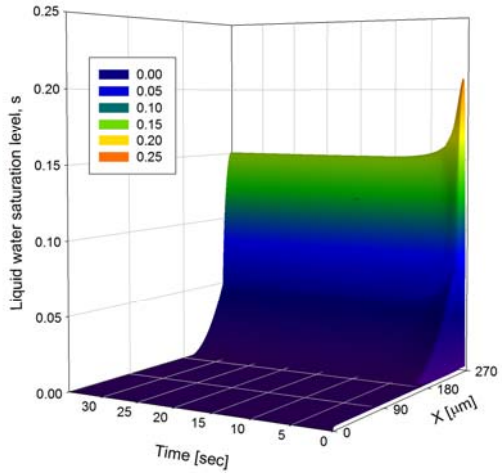

Fig 4-3. Evolution of the liquid water saturation level under various cell voltages. (a) V_s =0.2 V, (b) V_s =0.4 V, (c) V_s =0.6 V

(a)

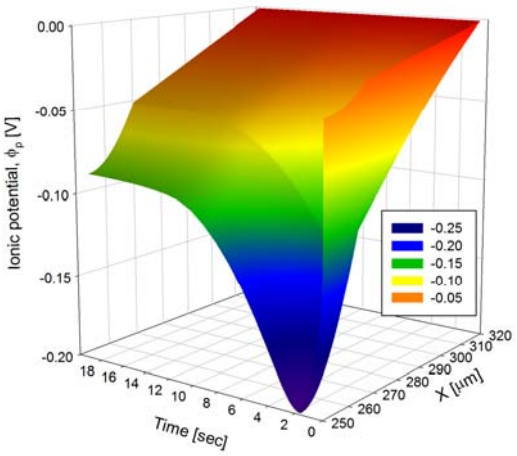

(b)

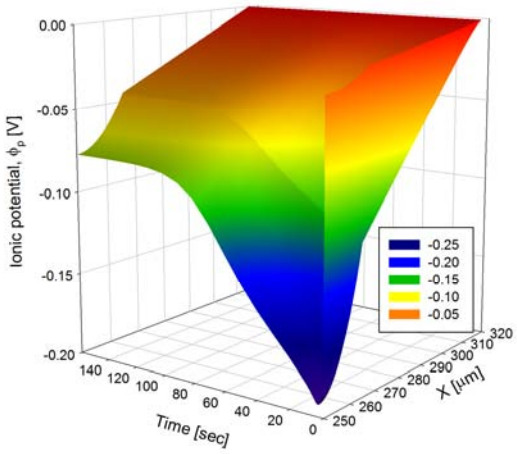

(c)

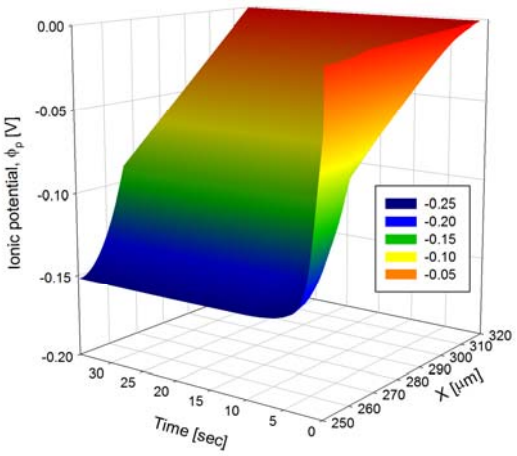

Fig 4-4. Evolution of the ionic potential distribution under various cell voltages. (a) V_s =0.2 V, (b) V_s =0.4 V, (c) V_s =0.6 V

(a)

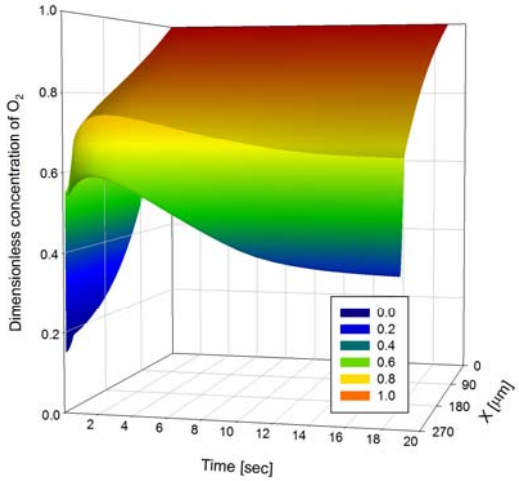

(b)

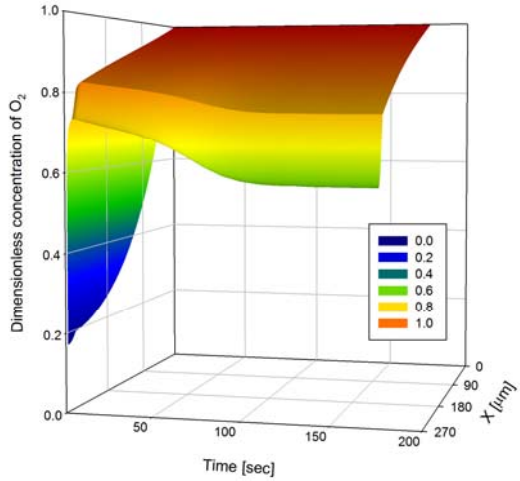

(c)

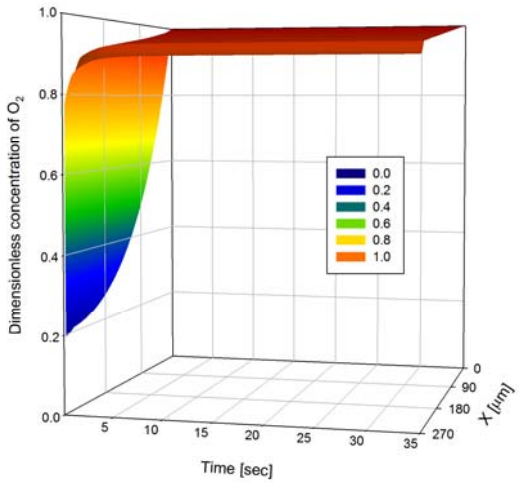

Fig 4-5. Evolution of the dimensionless oxygen concentration distribution under various cell voltages. (a) V_s =0.2 V, (b) V_s =0.4 V, (c) V_s =0.6 V

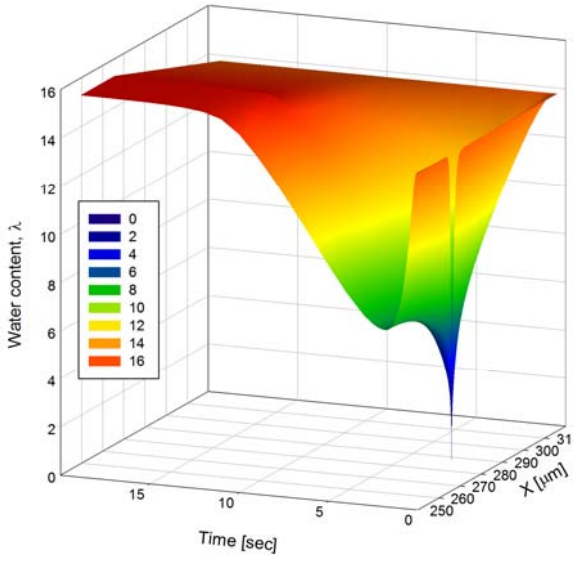

(a)

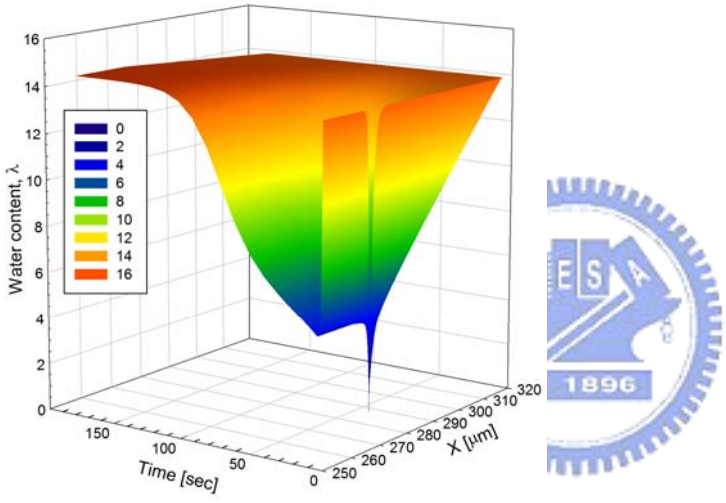

(b)

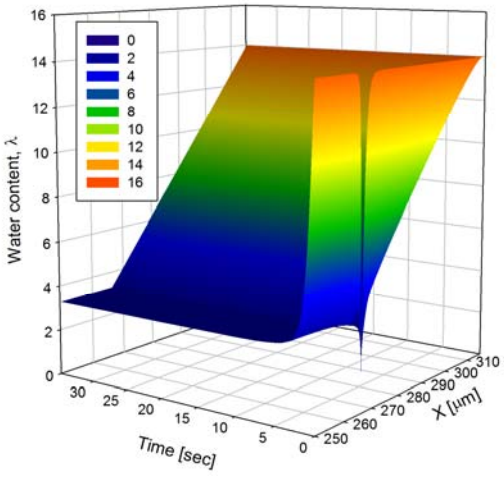

(c)

Fig 4-6. Evolution of the water content under various cell voltages. (a) V_s =0.2 V, (b) V_s =0.4 V, (c) V_s =0.6 V

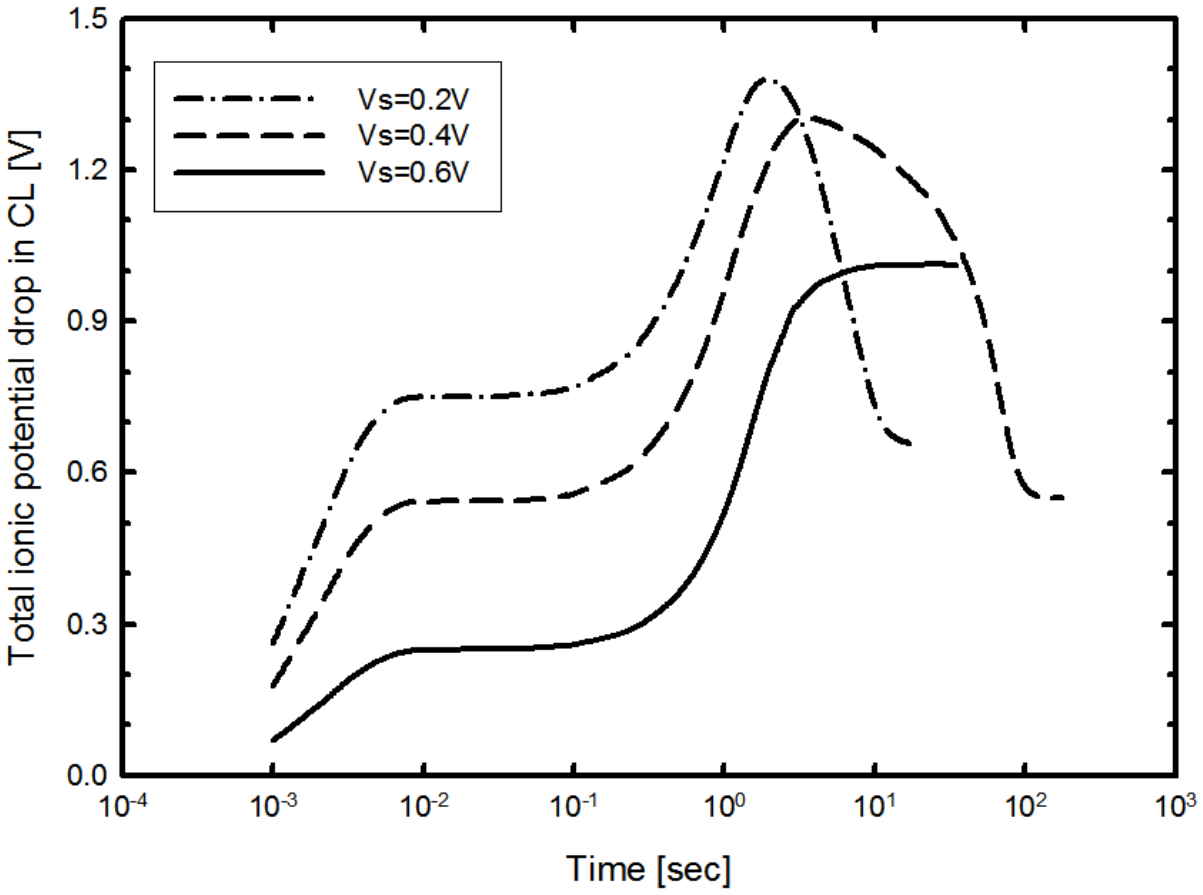

Fig 4-7. Evolution of the total ionic potential drop in the catalyst layer under various cell voltages.

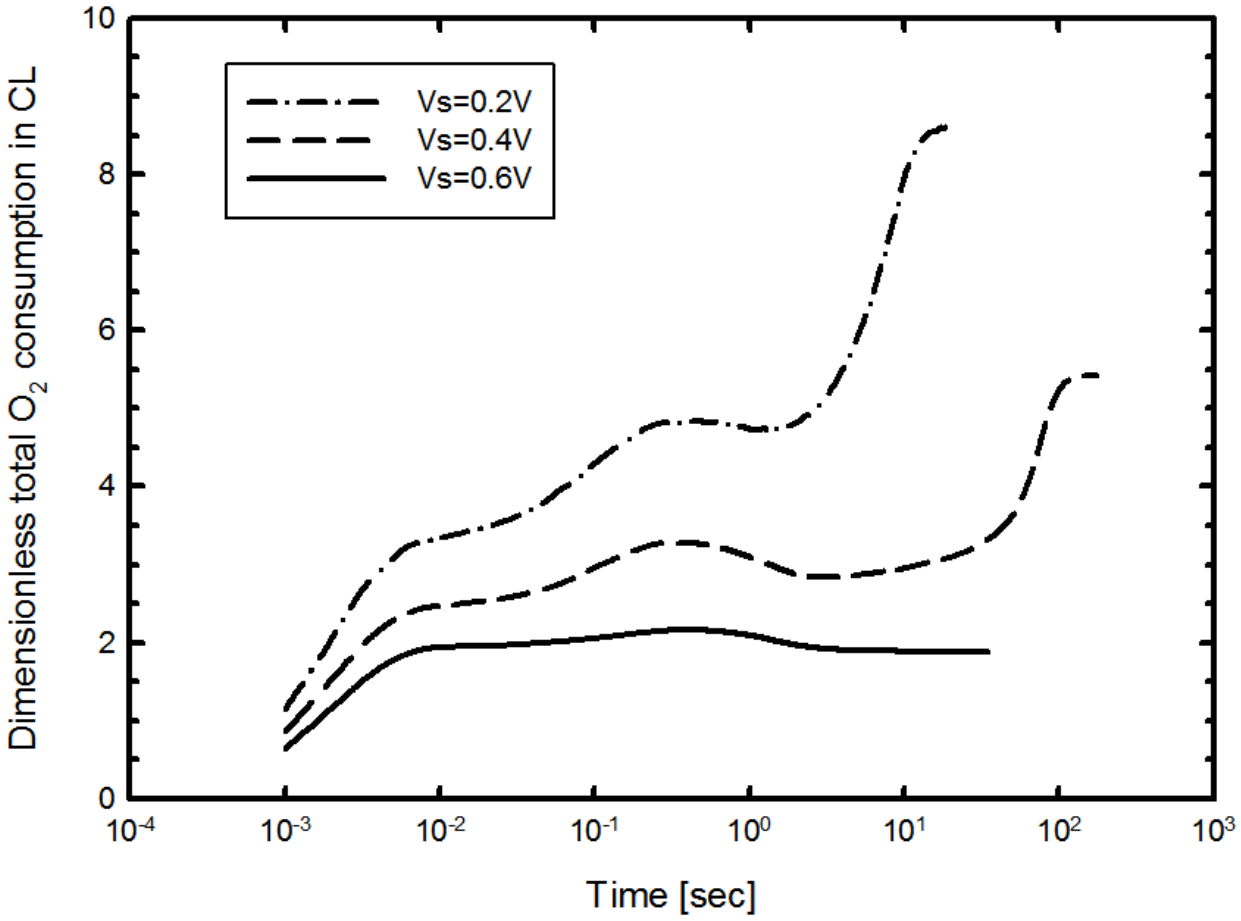

Fig 4-8. Evolution of the total dimensionless oxygen consumption in the catalyst layer under various cell voltages.

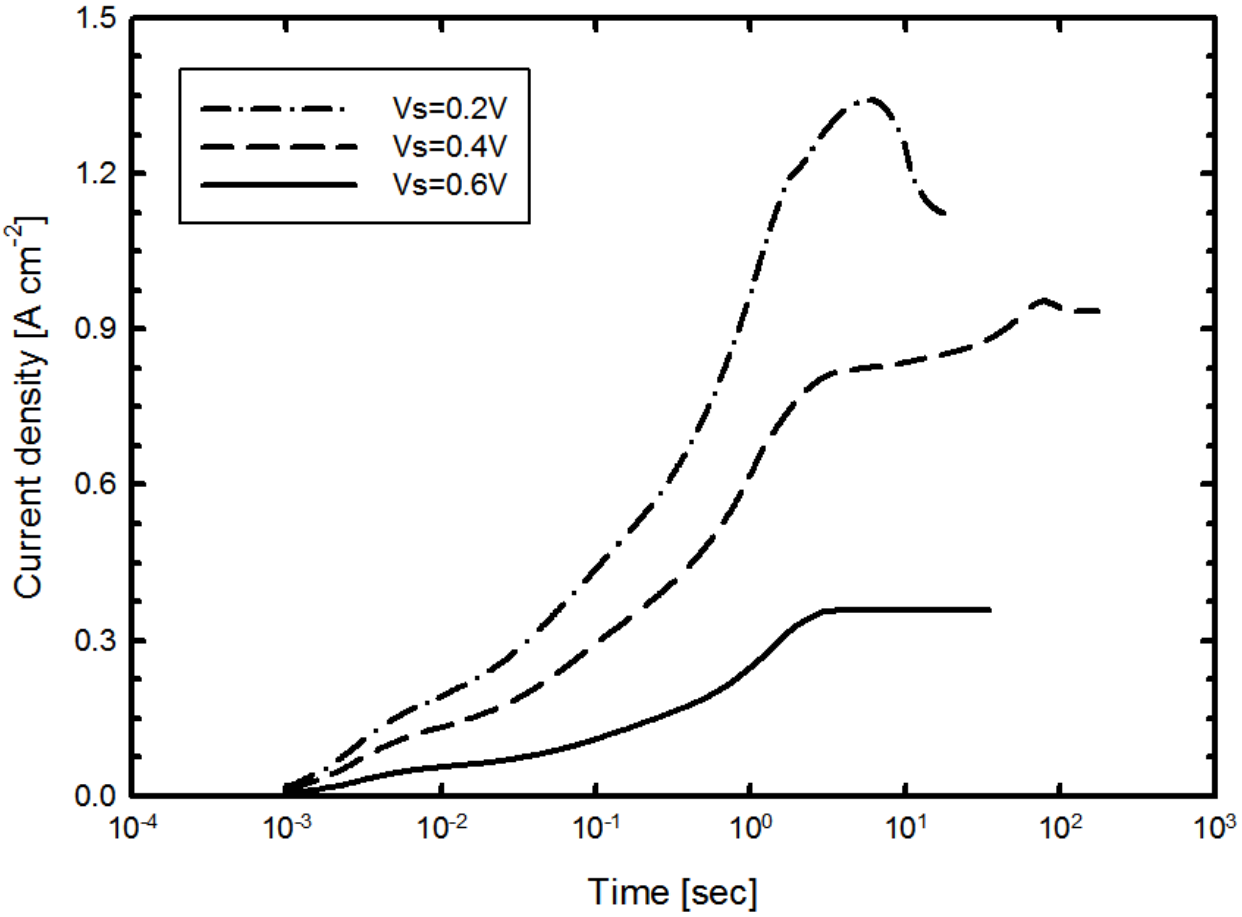

Fig 4-9. Evolution of the current density under various cell voltages.

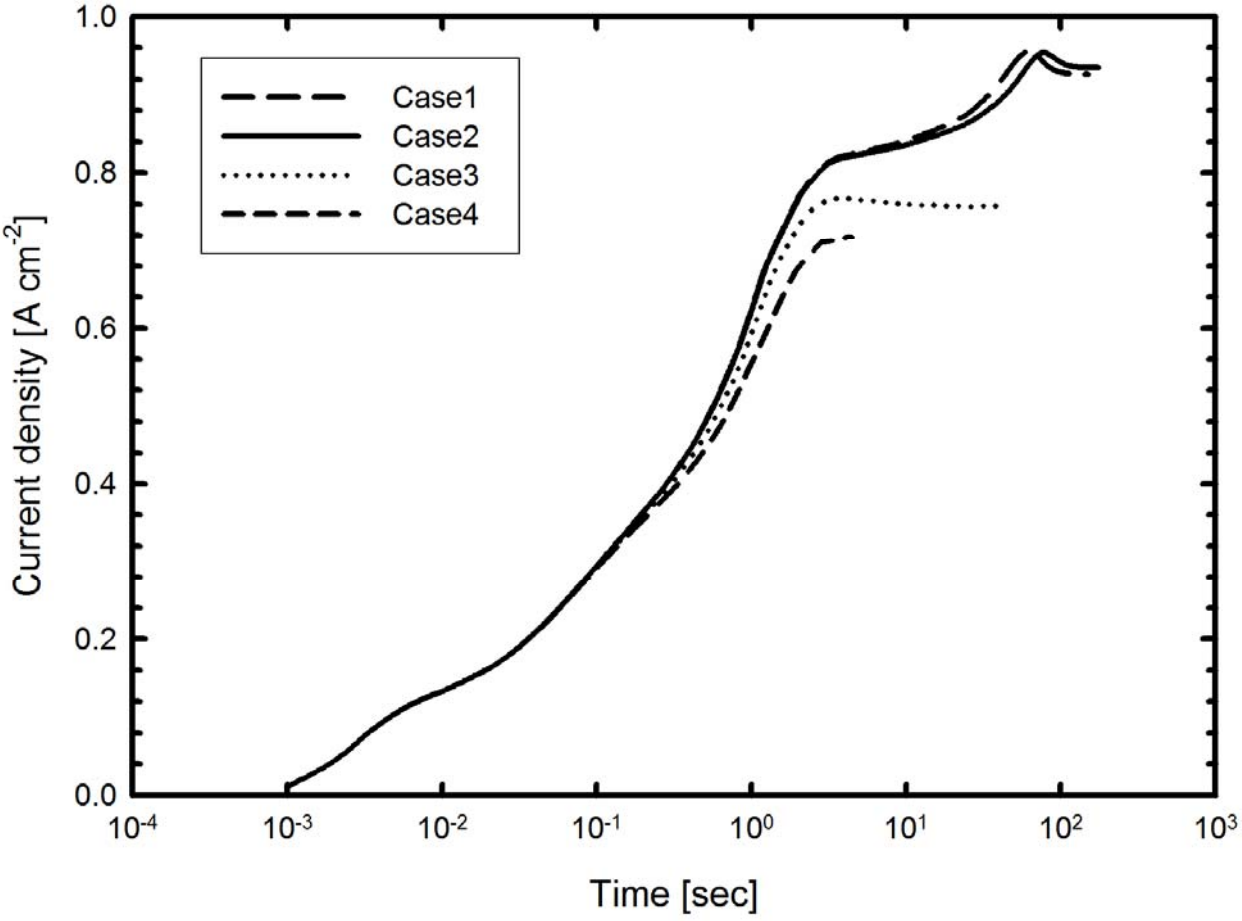

Fig 4-10. The effect of GDL permeability on the current density (V_s =0.4 V)

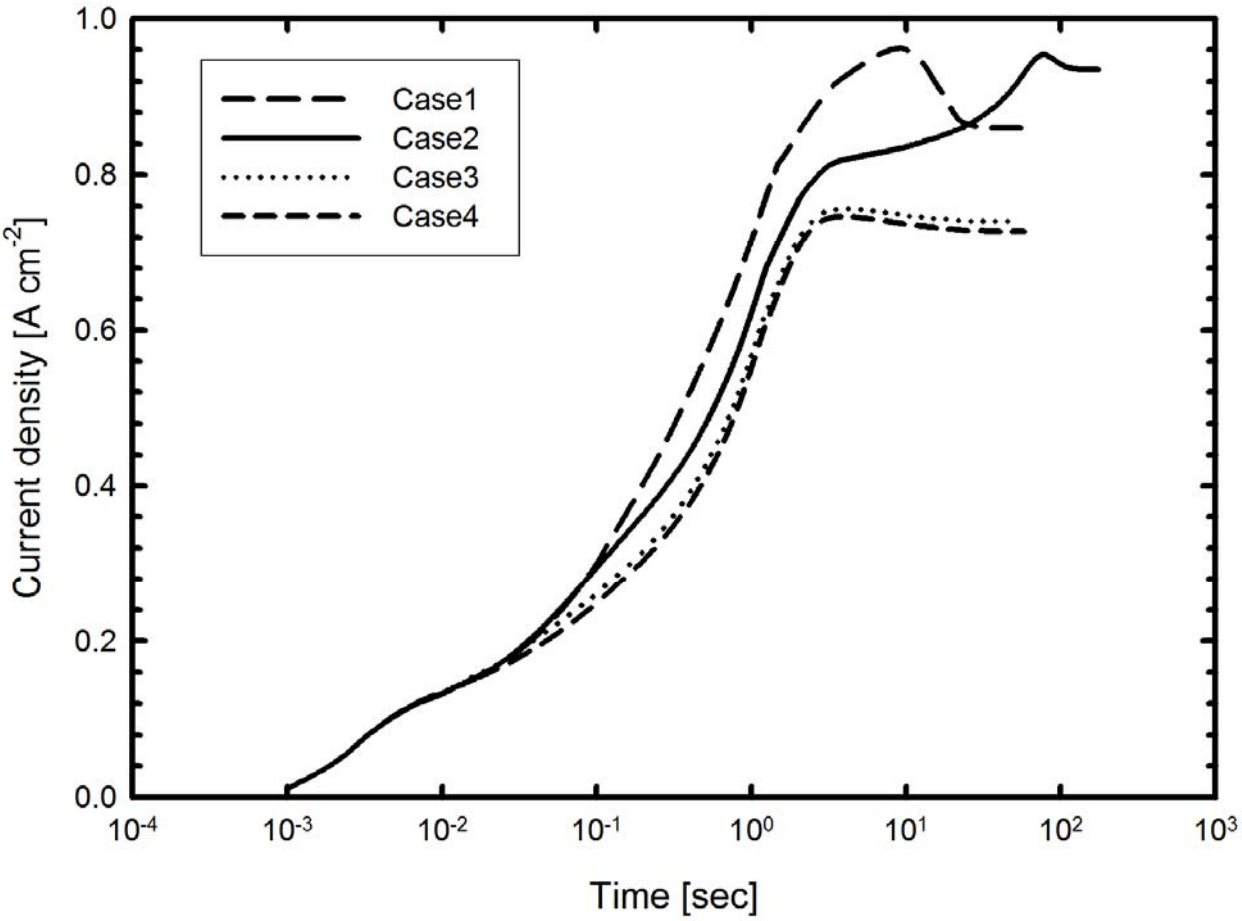

Fig 4-11. The effect of CL permeability on the current density (V_s =0.4 V)

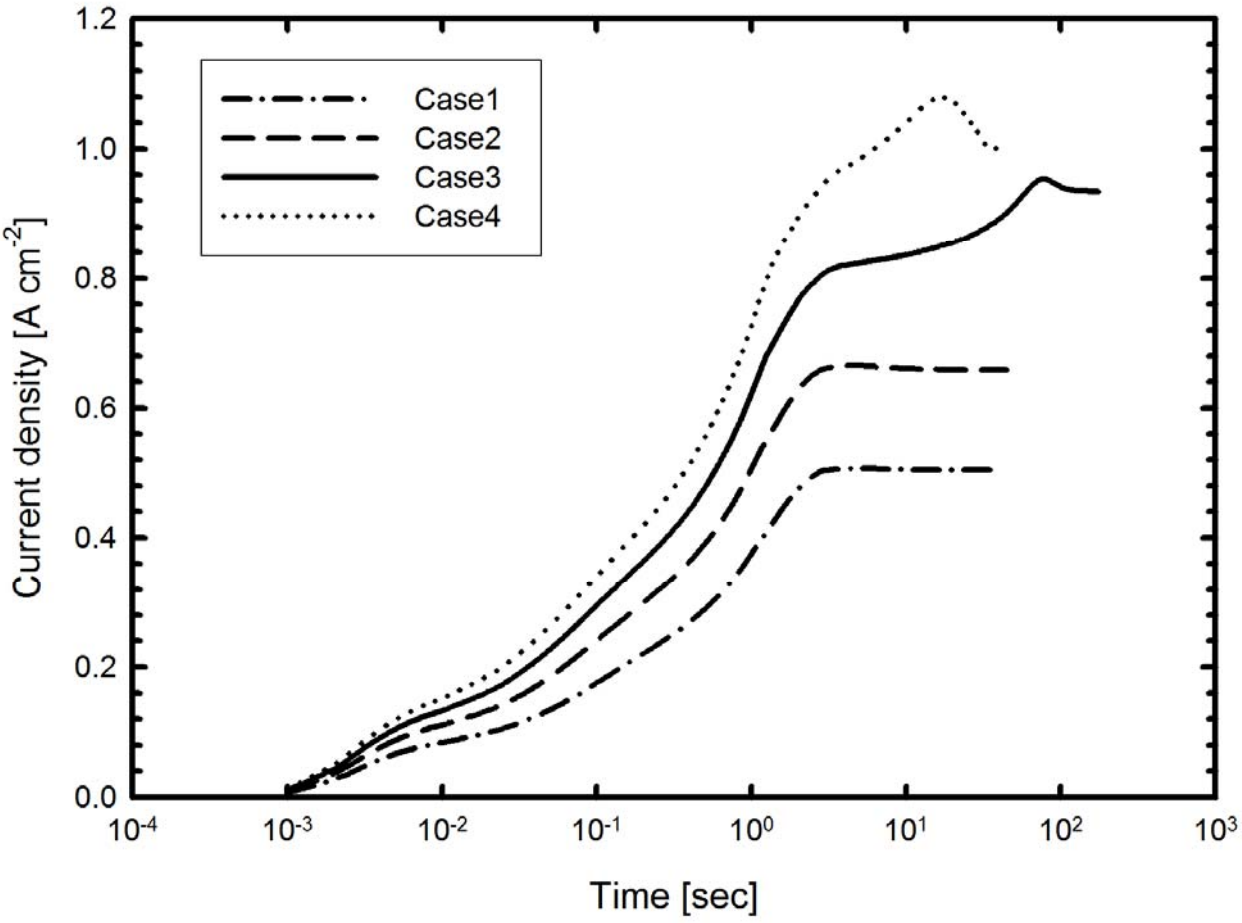

Fig 4-12. The effect of catalyst loading on the current density (V_s =0.4 V)

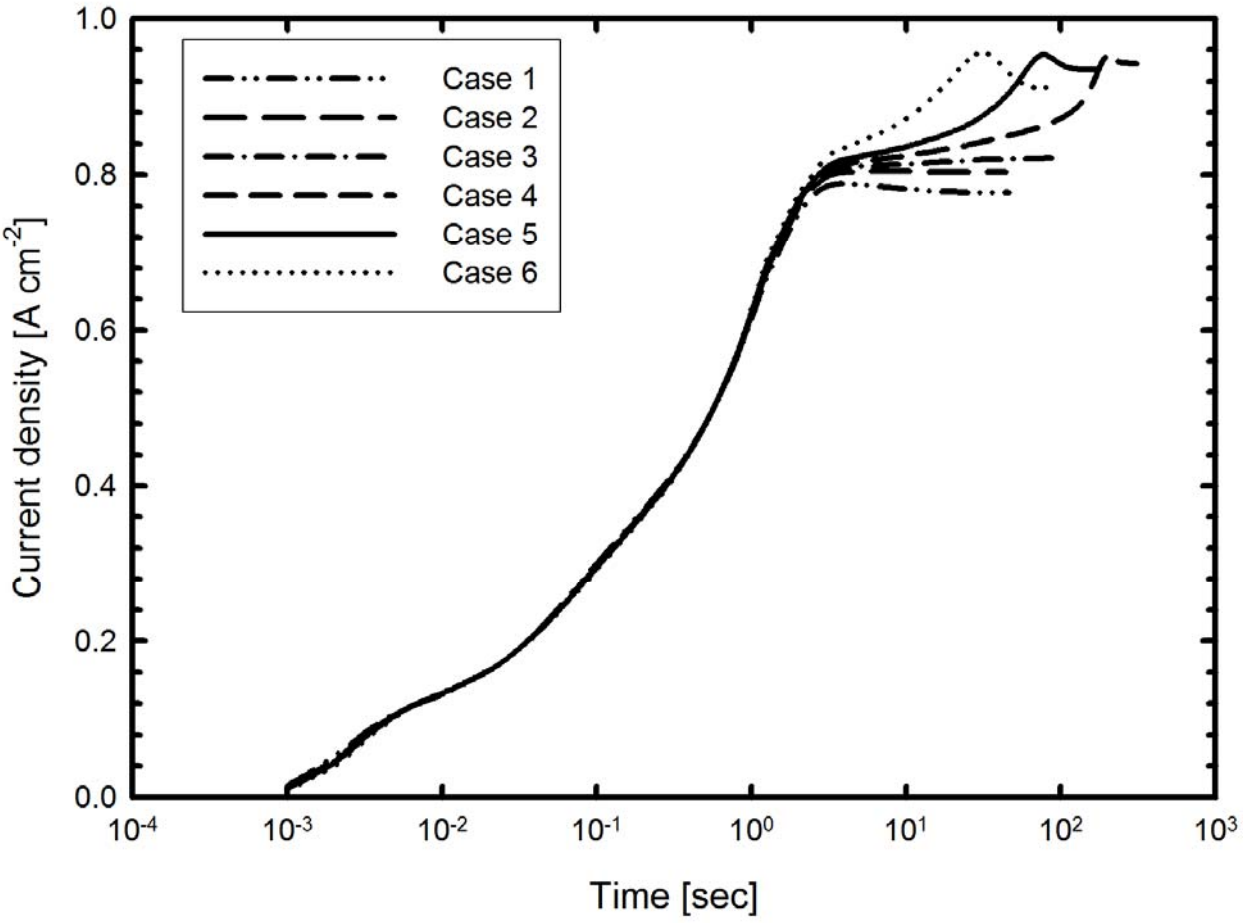

Fig 4-13. The effect of GDL thickness on the current density (V_s =0.4 V)

5. Conclusions and recommendations

This work includes the development, validation, and application of a mathematical model of a proton exchange membrane fuel cell cathode. The catalyst layer is treated as a thin film-agglomerate model. Two different geometric thin film-agglomerate models are used to investigate the transient transport of gaseous species, protons, and liquid water. The results agree well with the experimental data. Results generated by the model illustrate how the various species transport occurs within the fuel cell. Parametric studies of other design factors' effects reveal there optimum values which lead to a greater current output during its evolution period.

5.1. Conclusion regarding the cylindrical thin film-agglomerate model

In Chapter 2, a transient, two-phase model is developed to investigate the effect of water flooding in the gas diffusion layer and catalyst layer of the cathode on the overall cell performance. This model is developed to investigate the transient transport of gaseous species, protons, and liquid water. The effects of operating temperature and relative humidity of the air inlet on the cell performance are also studied. It is found from simulation results that the liquid water accumulation in the GDL and CL leads to electrode flooding if it is not drained efficiently. Moreover, the effect of liquid water in the catalyst layer should be taken in to account in modeling because it bears substantial impact upon the transient evolution of model properties and cell performance.

Modeling data also reveal that the transport of proton is much faster than the others. The ionic potential reaches the steady state in the order of 10^{-1} sec but the liquid water transport takes place in the order of 10 sec. The ionic potential does not decrease monotonically with time. It first reaches a critical value then increases with time till the steady state. This phenomenon is obvious under the condition that lower cell voltage is applied.

In the cases of lower cell voltage, the current density overshoots as time evolving. The overshot are 13%, 11% and 7% when the operating temperature is $60^{o}C$, $70^{o}C$ and $80^{o}C$ respectively. The higher the operating temperature is, the higher the cell performance will be. In the steady state.

In the parametric study on the transient evolution demonstrate that, within 10^{-2}sec, the current density rises rapidly. Between 10^{-2}sec and 10^{-1}sec, there is a plateau. After 1sec, the current density relates with cell voltage, gas diffusion layer porosity, catalyst layer porosity, catalyst layer thickness and agglomerate radius. For gas diffusion layer porosity, between ε_{GDL}=0.2 and ε_{GDL}=0.5, the higher the GDL porosity is, the higher the cell current density will be. After 1sec, if the GDL porosity is below 0.3, the current density will go down. When ε_{GDL}=0.2 and V_s=0.4V, the current density decreases 6%. But when V_s=0.2V, the current density decreases 15%. When ε_{GDL}=0.3 and V_s=0.2V, the current density decreases 8%. This is affected by the liquid water in the gas diffusion layer. When ε_{GDL}=0.5, the current density changes subtly.

For the catalyst layer porosity, the current density will decrease when the CL porosity is too low. When ε_{CL}=0.04 and V_s=0.2, the current density decreases about 20%. This is affected by the liquid water in the catalyst layer. The higher the CL porosity is, the more the water is drained. But the electric conductivity drops in the meantime. For catalyst layer porosity, optimum current density appears between ε_{CL}=0.06 and ε_{CL}=0.1.

During the simulation of the catalyst layer thickness effects, it is found that a thinner catalyst layer leads to lower platinum loading for the electrochemical reaction. On the contrary, a thicker catalyst layer, results in even more accumulated liquid water and the current density decreases rapidly. The optimum values of catalyst layer thickness appears between δ_{CL}=10 μm and 13 μm.

For the agglomerate radius study, the result reveal that a larger agglomerate causes the electrochemical reaction occurs only on the surface. The catalyst inside the agglomerate does not participate in the electrochemical reactions. Therefore, the current density and the utilization of catalyst are inversed. It suggests that the agglomerate radius should smaller than 100nm for a higher utilization of catalyst.

5.2. Conclusions regarding the spherical thin film-agglomerate model

A transient, one-dimensional, two-phase model of a PEM fuel cell cathode is presented in Chapter 4 with the catalyst layer treated as a spherical thin film-agglomerate. This model is used to investigate the transient transport of gaseous species, protons, and liquid water. The effects of GDL permeability, CL permeability, catalyst loading, and GDL thickness on cell performance are also investigated.

The model results agree well with the experimental data. The observed IPD and TOC variations show that after the fuel cell overcomes its maximum activation energy, a high electrochemical reaction rate with low IPD is maintained. Electrochemical reactions affect the amount of liquid water in the cell; when less water is generated, the cell reaction rate is reduced. Nevertheless, the higher liquid water content and saturation level tend to lead to the flooding catastrophe.

Parametric sensitivity analysis also shows that at higher permeability, more liquid water is able to drain from the cell. Cell performance will decrease if there is too little liquid water, but may also be influenced if the water cannot drain effectively. Among the values adopted in this chapter, the optimum GDL permeability is $K_{w,0}^{GDL} = 1 \times 10^{-9} cm^2$ and the optimum CL permeability is $K_{w,0}^{CL} = 3 \times 10^{-11} cm^2$.

Moreover, a cell with higher catalyst loading leads to more rapid electrochemical reactions, but this may also result in too much liquid water generation. This ultimately impedes oxygen transport, so excessive catalyst loading does not improve cell performance. Among the values considered in this chapter, the optimum loading is $m_{Pt} = 0.4mg$.

Finally, the GDL thickness is found to play an important role in liquid water transport. A thinner layer offers less resistance to liquid water diffusion and drainage. Water content and cell performance therefore tend to remain constant. When the gas diffusion layer is thick, liquid water cannot drain effectively and the catalyst pellets will have less surface oxygen. According to these results, the optimum thickness is $\delta_{GDL} = 245\mu m$.

5.3. Recommendations

In this work, the transient behavior for a PEM fuel cell via two-phase transient and half cell model which based on a thin film-agglomerate approach has been applied to investigate the transport of gaseous species, liquid water, proton, and electrochemical kinetics in great detail. Generally, the results obtained from this model are in agreement with experimental data. However, there are still a number of improvements for this model that can be done in the future.

1. Extend the model from one-dimensional to two-dimensional or higher-dimensional.
2. Extend the computation domain form cathode to a single cell.

References

1. Yi, J.S. and Van Nguyen, T., *Multicomponent transport in porous electrodes of proton exchange membrane fuel cells using the interdigitated gas distributors.* Journal of the Electrochemical Society, 1999. **146**(1): p. 38-45.
2. Amphlett, J.C., Baumert, R.M., Mann, R.F., Peppley, B.A., Roberge, P.R., and Harris, T.J., *Performance Modeling of the Ballard-Mark-Iv Solid Polymer Electrolyte Fuel-Cell .1. Mechanistic Model Development.* Journal of the Electrochemical Society, 1995. **142**(1): p. 1-8.
3. Amphlett, J.C., Baumert, R.M., Mann, R.F., Peppley, B.A., Roberge, P.R., and Harris, T.J., *Performance Modeling of the Ballard-Mark-Iv Sold Polymer Electrolyte Fuel-Cell .2. Empirical-Model Development.* Journal of the Electrochemical Society, 1995. **142**(1): p. 9-15.
4. Sena, D.R., Ticianelli, E.A., Paganin, V.A., and Gonzalez, E.R., *Effect of water transport in a PEFC at low temperatures operating with dry hydrogen*, in *Journal of Electroanalytical Chemistry*. 1999, Elsevier Science. p. 164 - 170.
5. Lee, S.J., Mukerjee, S., McBreen, J., Rho, Y.W., Kho, Y.T., and Lee, T.H., *Effects of Nafion impregnation on performances of PEMFC electrodes* Electrochimica Acta, 1998. **43**(24): p. 3693-3701.
6. Kim, J., Lee, S.M., Srinivasan, S., and Chamberlin, C.E., *Modeling of Proton-Exchange Membrane Fuel-Cell Performance with an Empirical-Equation.* Journal of the Electrochemical Society, 1995. **142**(8): p. 2670-2674.
7. Kulikovsky, A.A., *The voltage-current curve of a polymer electrolyte fuel cell: "exact" and fitting equations.* Electrochemistry Communications, 2002. **4**(11): p. 845-852.
8. Pisani, L., Murgia, G., Valentini, M., and D'Aguanno, B., *A new semi-empirical approach to performance curves of polymer electrolyte fuel cells.* Journal of Power Sources, 2002. **108**(1-2): p. 192-203.
9. Lufrano, F., Squadrito, G., Patti, A., and Giorgi, L., *Nafion content in the catalyst layer of polymer electrolyte fuel cells: effects on structure and performance*, in *Electrochimica Acta*. 2001, Elsevier Science. p. 799 - 805.
10. Squadrito, G., Maggio, G., Passalacqua, E., Lufrano, F., and Patti, A., *An empirical equation for polymer electrolyte fuel cell (PEFC) behaviour.* Journal of Applied Electrochemistry, 1999. **29**(12): p. 1449-1455.
11. Springer, T.E., Zawodzinski, T.A., Wilson, M.S., and Gottesfeld, S., *Characterization of*

polymer electrolyte fuel cells using AC impedance spectroscopy. Journal of the Electrochemical Society, 1996. **143**(2): p. 587-599.

12. Li, G.C. and Pickup, P.G., *Ionic conductivity of PEMFC electrodes - Effect of Nafion loading.* Journal of the Electrochemical Society, 2003. **150**(11): p. C745-C752.
13. Nam, J.H. and Kaviany, M., *Effective diffusivity and water-saturation distribution in single- and two-layer PEMFC diffusion medium.* International Journal of Heat and Mass Transfer, 2003. **46**(24): p. 4595-4611.
14. Kulikovsky, A.A., Divisek, J., and Kornyshev, A.A., *Modeling the cathode compartment of polymer electrolyte fuel cells: Dead and active reaction zones.* Journal of the Electrochemical Society, 1999. **146**(11): p. 3981-3991.
15. Kulikovsky, A.A., *Quasi-3D modeling of water transport in polymer electrolyte fuel cells.* Journal of the Electrochemical Society, 2003. **150**(11): p. A1432-A1439.
16. Weber, A.Z., Darling, R.M., and Newman, J., *Modeling two-phase behavior in PEFCs.* Journal of the Electrochemical Society, 2004. **151**(10): p. A1715-A1727.
17. Bird, R.B., Stewart, W.E., and Lightfoot, E.N., *Transport phenomena*. 1960, New York: Wiley. xxi, 780 p.
18. Gurau, V., Liu, H.T., and Kakac, S., *Two-dimensional model for proton exchange membrane fuel cells.* AIChE Journal, 1998. **44**(11): p. 2410-2422.
19. Dutta, S., Shimpalee, S., and Van Zee, J.W., *Three-dimensional numerical simulation of straight channel PEM fuel cells.* Journal of Applied Electrochemistry, 2000. **30**(2): p. 135-146.
20. Dutta, S., Shimpalee, S., and Van Zee, J.W., *Numerical prediction of mass-exchange between cathode and anode channels in a PEM fuel cell.* International Journal of Heat and Mass Transfer, 2001. **44**(11): p. 2029-2042.
21. He, W.S., Yi, J.S., and Van Nguyen, T., *Two-phase flow model of the cathode of PEM fuel cells using interdigitated flow fields.* AIChE Journal, 2000. **46**(10): p. 2053-2064.
22. Shimpalee, S. and Dutta, S., *Numerical prediction of temperature distribution in PEM fuel cells.* Numerical Heat Transfer Part a-Applications, 2000. **38**(2): p. 111-128.
23. Berning, T., Lu, D.M., and Djilali, N., *Three-dimensional computational analysis of transport phenomena in a PEM fuel cell.* Journal of Power Sources, 2002. **106**(1-2): p. 284-294.
24. Berning, T. and Djilali, N., *A 3D, multiphase, multicomponent model of the cathode and anode of a PEM fuel cell.* Journal of the Electrochemical Society, 2003. **150**(12): p. A1589-a1598.

25. Siegel, N.P., Ellis, M.W., Nelson, D.J., and von Spakovsky, M.R., *Single domain PEMFC model based on agglomerate catalyst geometry.* Journal of Power Sources, 2003. **115**(1): p. 81-89.
26. Um, S. and Wang, C.Y., *Three-dimensional analysis of transport and electrochemical reactions in polymer electrolyte fuel cells.* Journal of Power Sources, 2004. **125**(1): p. 40-51.
27. Springer, T.E., Zawodzinski, T.A., and Gottesfeld, S., *Polymer Electrolyte Fuel-Cell Model.* Journal of the Electrochemical Society, 1991. **138**(8): p. 2334-2342.
28. Springer, T.E., Wilson, M.S., and Gottesfeld, S., *Modeling and Experimental Diagnostics in Polymer Electrolyte Fuel-Cells.* Journal of the Electrochemical Society, 1993. **140**(12): p. 3513-3526.
29. Baschuk, J.J. and Li, X.H., *Modelling of polymer electrolyte membrane fuel cells with variable degrees of water flooding.* Journal of Power Sources, 2000. **86**(1-2): p. 181-196.
30. Gurau, V., Barbir, F., and Liu, H.T., *An analytical solution of a half-cell model for PEM fuel cells.* Journal of the Electrochemical Society, 2000. **147**(7): p. 2468-2477.
31. Chu, H.S., Yeh, C., and Chen, F., *Effects of porosity change of gas diffuser on performance of proton exchange membrane fuel cell.* Journal of Power Sources, 2003. **123**(1): p. 1-9.
32. Wood, D.L., Yi, Y.S., and Nguyen, T.V., *Effect of direct liquid water injection and interdigitated flow field on the performance of proton exchange membrane fuel cells.* Electrochimica Acta, 1998. **43**(24): p. 3795-3809.
33. Natarajan, D. and Van Nguyen, T., *A two-dimensional, two-phase, multicomponent, transient model for the cathode of a proton exchange membrane fuel cell using conventional gas distributors.* Journal of the Electrochemical Society, 2001. **148**(12): p. A1324-a1335.
34. Natarajan, D. and Van Nguyen, T., *Three-dimensional effects of liquid water flooding in the cathode of a PEM fuel cell.* Journal of Power Sources, 2003. **115**(1): p. 66-80.
35. Wang, Z.H., Wang, C.Y., and Chen, K.S., *Two-phase flow and transport in the air cathode of proton exchange membrane fuel cells.* Journal of Power Sources, 2001. **94**(1): p. 40-50.
36. Pasaogullari, U. and Wang, C.Y., *Liquid water transport in gas diffusion layer of polymer electrolyte fuel cells.* Journal of the Electrochemical Society, 2004. **151**(3): p. A399-A406.
37. Pasaogullari, U. and Wang, C.Y., *Two-phase transport and the role of micro-porous layer in polymer electrolyte fuel cells.* Electrochimica Acta, 2004. **49**(25): p. 4359-4369.
38. Pasaogullari, U. and Wang, C.Y., *Two-phase modeling and flooding prediction of polymer electrolyte fuel cells.* Journal of the Electrochemical Society, 2005. **152**(2): p. A380-A390.
39. Pasaogullari, U., Wang, C.Y., and Chen, K.S., *Two-phase transport in polymer electrolyte fuel cells with bilayer cathode gas diffusion media.* Journal of the Electrochemical Society,

2005. **152**(8): p. A1574-A1582.

40. Meng, H. and Wang, C.-Y., *Model of Two-Phase Flow and Flooding Dynamics in Polymer Electrolyte Fuel Cells.* Journal of the Electrochemical Society, 2005. **152**(9): p. A1733-A1741.
41. Meng, H. and Wang, C.Y., *Model of two-phase flow and flooding dynamics in polymer electrolyte fuel cells.* Journal of the Electrochemical Society, 2005. **152**(9): p. A1733-A1741.
42. Wang, Y. and Wang, C.-Y., *A nonisothermal, two-phase model for polymer electrolyte fuel cells.* Journal of the Electrochemical Society, 2006. **153**(6): p. A1193-A1200.
43. Cheng, P. and Wang, C.Y., *A multiphase mixture model for multiphase, multicomponent transport in capillary porous media .2. Numerical simulation of the transport of organic compounds in the subsurface.* International Journal of Heat and Mass Transfer, 1996. **39**(17): p. 3619-3632.
44. Wang, C.Y. and Cheng, P., *A multiphase mixture model for multiphase, multicomponent transport in capillary porous media .1. Model development.* International Journal of Heat and Mass Transfer, 1996. **39**(17): p. 3607-3618.
45. Jang, J.-H., Yan, W.-M., and Shih, C.-C., *Effects of the gas diffusion-layer parameters on cell performance of PEM fuel cells.* Journal of Power Sources, 2006. **161**(1): p. 323-332.
46. Wang, C.Y., *Fundamental models for fuel cell engineering.* Chemical Reviews, 2004. **104**(10): p. 4727-4765.
47. Weber, A.Z. and Newman, J., *Modeling transport in polymer-electrolyte fuel cells.* Chemical Reviews, 2004. **104**(10): p. 4679-4726.
48. Hwang, J.J., *A complete two-phase model of a porous cathode of a PEM fuel cell.* Journal of Power Sources, 2007. **164**(1): p. 174-181.
49. Schulz, V.P., Becker, J., Wiegmann, A., Mukherjee, P.P., and Wang, C.Y., *Modeling of two-phase behavior in the gas diffusion medium of PEFCs via full morphology approach.* Journal of the Electrochemical Society, 2007. **154**(4): p. B419-B426.
50. Weber, A.Z. and Newman, J., *Transport in polymer-electrolyte membranes - I. Physical model.* Journal of the Electrochemical Society, 2003. **150**(7): p. A1008-a1015.
51. Weber, A.Z. and Newman, J., *A theoretical study of membrane constraint in polymer-electrolyte fuel cells.* AIChE Journal, 2004. **50**(12): p. 3215-3226.
52. Weber, A.Z. and Newman, J., *Transport in polymer-electrolyte membranes - II. Mathematical model.* Journal of the Electrochemical Society, 2004. **151**(2): p. A311-a325.
53. Weber, A.Z. and Newman, J., *Transport in polymer-electrolyte membranes - III. Model validation in a simple fuel-cell model.* Journal of the Electrochemical Society, 2004. **151**(2):

p. A326-A339.

54. Bevers, D., Wohr, M., Yasuda, K., and Oguro, K., *Simulation of a polymer electrolyte fuel cell electrode.* Journal of Applied Electrochemistry, 1997. **27**(11): p. 1254-1264.

55. Rho, Y.W., Srinivasan, S., and Kho, Y.T., *Mass-Transport Phenomena in Proton-Exchange Membrane Fuel-Cells Using O2/He, O2/Ar, and O2/N2 Mixtures .2. Theoretical-Analysis.* Journal of the Electrochemical Society, 1994. **141**(8): p. 2089-2096.

56. Mazumder, S. and Cole, J.V., *Rigorous 3-d mathematical modeling of PEM fuel cells - II. Model predictions with liquid water transport.* Journal of the Electrochemical Society, 2003. **150**(11): p. A1510-A1517.

57. Nguyen, T.V. and White, R.E., *A Water and Heat Management Model for Proton-Exchange-Membrane Fuel-Cells.* Journal of the Electrochemical Society, 1993. **140**(8): p. 2178-2186.

58. Wang, J.T. and Savinell, R.F., *Simulation Studies on the Fuel Electrode of a H2-O2 Polymer Electrolyte Fuel-Cell.* Electrochimica Acta, 1992. **37**(15): p. 2737-2745.

59. Hsing, I.M. and Futerko, P., *Two-dimensional simulation of water transport in polymer electrolyte fuel cells.* Chemical Engineering Science, 2000. **55**(19): p. 4209-4218.

60. Lee, W.K., Shimpalee, S., and Van Zee, J.W., *Verifying predictions of water and current distributions in a serpentine flow field polymer electrolyte membrane fuel cell.* Journal of the Electrochemical Society, 2003. **150**(3): p. A341-A348.

61. Okada, T., Xie, G., Gorseth, O., Kjelstrup, S., Nakamura, N., and Arimura, T., *Ion and water transport characteristics of Nafion membranes as electrolytes.* Electrochimica Acta, 1998. **43**(24): p. 3741-3747.

62. Um, S., Wang, C.Y., and Chen, C.S., *Computational fluid dynamics modeling of proton exchange membrane fuel cells.* Journal of the Electrochemical Society, 2000. **147**(12): p. 4485-4493.

63. Rowe, A. and Li, X.G., *Mathematical modeling of proton exchange membrane fuel cells.* Journal of Power Sources, 2001. **102**(1-2): p. 82-96.

64. Bernardi, D.M. and Verbrugge, M.W., *Mathematical-Model of a Gas-Diffusion Electrode Bonded to a Polymer Electrolyte.* AIChE Journal, 1991. **37**(8): p. 1151-1163.

65. Bernardi, D.M. and Verbrugge, M.W., *A Mathematical-Model of the Solid-Polymer-Electrolyte Fuel-Cell.* Journal of the Electrochemical Society, 1992. **139**(9): p. 2477-2491.

66. Janssen, G.J.M., *A phenomenological model of water transport in a proton exchange membrane fuel cell.* Journal of the Electrochemical Society, 2001. **148**(12): p.

A1313-A1323.

67. Mann, R.F., Amphlett, J.C., Hooper, M.A.I., Jensen, H.M., Peppley, B.A., and Roberge, P.R., *Development and application of a generalised steady-state electrochemical model for a PEM fuel cell.* Journal of Power Sources, 2000. **86**(1-2): p. 173-180.
68. Perry, M.L., Newman, J., and Cairns, E.J., *Mass transport in gas-diffusion electrodes: A diagnostic tool for fuel-cell cathodes.* Journal of the Electrochemical Society, 1998. **145**(1): p. 5-15.
69. Marr, C. and Li, X.G., *Composition and performance modelling of catalyst layer in a proton exchange membrane fuel cell.* Journal of Power Sources, 1999. **77**(1): p. 17-27.
70. Eikerling, M. and Kornyshev, A.A., *Modelling the performance of the cathode catalyst layer of polymer electrolyte fuel cells.* Journal of Electroanalytical Chemistry, 1998. **453**(1-2): p. 89-106.
71. Broka, K. and Ekdunge, P., *Modelling the PEM fuel cell cathode.* Journal of Applied electrochemistry, 1997. **27**: p. 281-289.
72. Gloaguen, F. and Durand, R., *Simulations of PEFC cathodes: an effectiveness factor approach.* Journal of Applied Electrochemistry, 1997. **27**(9): p. 1029-1035.
73. Wang, Y. and Wang, C.Y., *Transient analysis of polymer electrolyte fuel cells.* Electrochimica Acta, 2005. **50**(6): p. 1307-1315.
74. Wang, Y. and Wang, C.-Y., *Dynamics of polymer electrolyte fuel cells undergoing load changes.* Electrochimica Acta, 2006. **51**(19): p. 3924-3933.
75. Fischer, A., Jindra, J., and Wendt, H., *Porosity and catalyst utilization of thin layer cathodes in air operated PEM-fuel cells.* Journal of Applied Electrochemistry, 1998. **28**(3): p. 277-282.
76. Bultel, Y., Ozil, P., and Durand, R., *Modified thin film and agglomerate models for active layers of PE fuel cells.* Electrochimica Acta, 1998. **43**(9): p. 1077-1087.
77. Gloaguen, F., Convert, P., Gamburzev, S., Velev, O.A., and Srinivasan, S., *An evaluation of the macro-homogeneous and agglomerate model for oxygen reduction in PEMFCs.* Electrochimica Acta, 1998. **43**(24): p. 3767-3772.
78. Ihonen, J., Jaouen, F., Lindbergh, G., Lundblad, A., and Sundholm, G., *Investigation of mass-transport limitations in the solid polymer fuel cell cathode - II. Experimental.* Journal of the Electrochemical Society, 2002. **149**(4): p. A448-A454.
79. Jaouen, F., Lindbergh, G., and Sundholm, G., *Investigation of mass-transport limitations in the solid polymer fuel cell cathode - I. Mathematical model.* Journal of the Electrochemical Society, 2002. **149**(4): p. A437-A447.

80. Fogler, H.S., *Elements of chemical reaction engineering*. 2nd ed. Prentice-Hall international series in the physical and chemical engineering sciences. 1992, Upper Saddle River, NJ: Prentice Hall PTR.
81. Navessin, T., Eikerling, M., Wang, Q.P., Song, D.T., Liu, Z.S., Horsfall, J., Lovell, K.V., and Holdcroft, S., *Influence of membrane ion exchange capacity on the catalyst layer performance in an operating PEM fuel cell.* Journal of the Electrochemical Society, 2005. **152**(4): p. A796-a805.
82. Navessin, T., Holdcroft, S., Wang, Q.P., Song, D.T., Liu, Z.S., Eikerling, M., Horsfall, J., and Lovell, K.V., *The role of membrane ion exchange capacity on membrane vertical bar gas diffusion electrode interfaces: a half-fuel cell electrochemical study.* Journal of Electroanalytical Chemistry, 2004. **567**(1): p. 111-122.
83. Wang, Q.P., Eikerling, M., Song, D.T., and Liu, Z.S., *Structure and performance of different types of agglomerates in cathode catalyst layers of PEM fuel cells.* Journal of Electroanalytical Chemistry, 2004. **573**(1): p. 61-69.
84. Wang, Q.P., Eikerling, M., Song, D.T., Liu, Z.S., Navessin, T., Xie, Z., and Holdcroft, S., *Functionally graded cathode catalyst layers for polymer electrolyte fuel cells - I. Theoretical modeling.* Journal of the Electrochemical Society, 2004. **151**(7): p. A950-a957.
85. Wang, Q.P., Song, D.T., Navessin, T., Holdcroft, S., and Liu, Z.S., *A mathematical model and optimization of the cathode catalyst layer structure in PEM fuel cells.* Electrochimica Acta, 2004. **50**(2-3): p. 725-730.
86. Wang, Y. and Wang, C.Y., *Simulation of flow and transport phenomena in a polymer electrolyte fuel cell under low-humidity operation.* Journal of Power Sources, 2005. **147**(1-2): p. 148-161.
87. Song, D.T., Wang, Q.P., Liu, Z.S., Eikerling, M., Xie, Z., Navessin, T., and Holdcroft, S., *A method for optimizing distributions of Nafion and Pt in cathode catalyst layers of PEM fuel cells.* Electrochimica Acta, 2005. **50**(16-17): p. 3347-3358.
88. Song, D.T., Wang, Q.P., Liu, Z.S., Navessin, T., Eioerling, M., and Holdcroft, S., *Numerical optimization study of the catalyst layer of PEM fuel cell cathode.* Journal of Power Sources, 2004. **126**(1-2): p. 104-111.
89. Song, D.T., Wang, Q.P., Liu, Z.S., Navessin, T., and Holdcroft, S., *Numerical study of PEM fuel cell cathode with non-uniform catalyst layer.* Electrochimica Acta, 2004. **50**(2-3): p. 731-737.
90. Ge, S.H. and Yi, B.L., *A mathematical model for PEMFC in different flow modes.* Journal of Power Sources, 2003. **124**(1): p. 1-11.

91. Lin, G.Y., He, W.S., and Van Nguyen, T., *Modeling liquid water effects in the gas diffusion and catalyst layers of the cathode of a PEM fuel cell.* Journal of the Electrochemical Society, 2004. **151**(12): p. A1999-A2006.
92. Lin, G. and Van Nguyen, T., *A Two-Dimensional Two-Phase Model of a PEM Fuel Cell.* Journal of The Electrochemical Society, 2006. **153**(2): p. A372-A382.
93. Bird, R.B., Stewart, W.E., and Lightfoot, E.N., *Transport phenomena*. 2nd ed. 2002, New York: Wiley. xii, 895 p.

Author

姓名　張時明

地址　新竹市關東路 260 巷 79 號

學歷

國立交通大學機械工程學系博士班	89/9~
國立交通大學機械工程學系碩士班	88/9~89/6
國立交通大學械械工程學系學士班	85/9~88/6
明新工專機械科	76/9~81/6

經歷

工研院醫材中心副工程師	95/11~
陸軍中尉連輔導長	83/1~85/4
陸軍少尉連輔導長	82/6~83/1
陸軍少尉政戰官	82/1~82/6

Publication list

Journal Paper

1. Chang, S.-M. and Chu, H.-S., *Transient behavior of a PEMFC.* Journal of Power Sources, 2006. **161**(2): p. 1161-1168.
2. Chang, S.-M. and Chu, H.-S., *A Transient Model of PEM Fuel Cells Based on a Spherical Thin Film-Agglomerate Approach.* Journal of Power Sources, 2007, In press.

Conference Paper

1. Chu, H.-S. and Chang, S.-M., *A two-phase, transient model for the cathode of a PEMFC using thin film-agglomerate approach*, in *The 4th International Conference on FUEL CELL SCIENCE, ENGINEERING and TECHNOLOGY*. 2006: Irvine, CA.